

**STATISTICAL METHODS IN SUBSURFACE OBJECT  
DETECTION AND LOCALIZATION FROM GROUND  
PENETRATING RADAR**

A Thesis Presented

by

Xiaoyin Xu

to

The Department of Electrical and Computer Engineering

in partial fulfillment of the requirements

for the degree of

Doctor of Philosophy

in the field of

Electrical Engineering

Northeastern University

Boston, Massachusetts

December 4, 2001

## Acknowledgments

At first, I would like to thank my thesis advisors, Professors Eric L. Miller, Carey M. Rappaport, and Anthony J. Devaney, for their support, guidance, and encouragement. It is only with their insightful advice, invaluable suggestion, and inspiring comments is writing the thesis not only possible but enjoyable. This work was supported financially by an ARO MURI on Demining under Grant DAAG55-97-1-0013. I like to thank EG&G Inc for sharing with me their GPR data. I like to thank Demining Technology Center (DeTeC) at the Ecole Polytechnique Fédérale de Lausanne (EPFL) and the inheritor of the EPFL materials, Free University of Brussels (VUB), for allowing me to use their GPR database. Thanks also go to ERA Technology, owner of the Joint Research Center (JRC) landmine signatures database, for making their GPR data available to my research. The author acknowledges that the copyright in the radar data supplied remains vested at all times in ERA Technology and thank ERA Technology for permission to use the data. I also like to thank BRTRC, Inc. for providing the field data used in Chapter 5. Especially I would like to thank Mr. Fred Coldfeter and Mark Hibbard for providing details about the BRTRC data.

## Note on terminologies and symbols

In this proposal, following terms are used interchangeably or have similar meaning.

GPR data    GPR signals, (GPR) traces, GPR gathers

Target        Object, landmine

Trace         Data vector, time-series

Listed below are the commonly used symbols appeared in this proposal, together with their various meanings and units if available.

| <i>Symbol</i>      | <i>Meaning</i>  | <i>Units</i> |
|--------------------|---|--------------|
| $\mathcal{F}$      | Fourier transform   |              |
| $\mathcal{F}^{-1}$ | inverse Fourier transform   |              |
| $f$                | Frequency   | cycle/sec    |
| <sub>i</sub>       | Subscript “i” denotes variables in “image space”                      |              |
| $j$                | Imaginary unit  | $\sqrt{-1}$  |
| $k_x$              | Wavenumber in the $x$ -direction                                      | 1/m          |
| $k_y$              | Wavenumber in the $y$ -direction                                      | 1/m          |
| $k_z$              | Wavenumber in the $z$ -direction                                      | 1/m          |
| <sub>o</sub>       | Subscript “o” denotes variables in “object space”                     |              |
| <b>P</b>           | Upper case bold symbols, vector or matrix in the Fourier domain       |              |
| <b>p</b>           | Lower case bold symbols, vector or matrix in the space or time domain |              |
| <b>R</b>           | Regularization operator   |              |
| $t$                | Time  | sec          |
| $v$                | Velocity  | m/sec        |
| $x, y, z$          | Rectangular coordinates   | m            |
| $\alpha$           | Attenuation constant  | neper/m      |
| $\lambda$          | Wavelength  | m            |
|                    | Regularization parameter  |              |

| <i>Symbol</i>             | <i>Meaning</i>   | <i>Units</i>         |
|---------------------------|--|----------------------|
| $\epsilon$                | Dielectric constant  | farad/m (F/m)        |
| $\epsilon_0$              | Permittivity of free space                                 | F/m                  |
| $\epsilon_r$              | Relative permittivity                                      |                      |
| $\mu$                     | Magnetic permeability                                      | henry/m (H/m)        |
|                           | Mean value of random variable                              |                      |
| $\mu_0$                   | Magnetic permeability of free space                        | H/m                  |
| $\omega$                  | Angular frequency  | radian/sec           |
| $\sigma$                  | Electric conductivity                                      | mho/m ( $\Omega$ /m) |
|                           | Standard deviation   |                      |
| $\sigma_i$                | The $i$ th singular values of singular value decomposition |                      |
| $\tau$                    | Time delay   | sec                  |
| $\frac{\epsilon}{\sigma}$ |  | F/ $\Omega$          |

## **Abstract**

The use of ground penetrating radar (GPR) arrays for detecting and localizing buried objects has received considerable attention in recent years in areas such as landmine and unexploded ordnance remediation, utility line mapping, and archaeological discovery. A typical GPR array is implemented by moving a pair of transmitter and receiver along a linear track. At every stop of the system, the transmitter emits a short pulse of electromagnetic energy which interacts with the surrounding medium. Based on observations of scattered fields collected by the array the objective of the problem is to determine if an object is present in the field of view of the array and, furthermore, localize its position. In this research, we employ a statistical signal processing method in detection and an optimized imaging method in localization.

Here we view the detection problem in the framework of a blind transient signal detection and employ statistical method to process the GPR returns. The approach allows us to exploit two generic properties of the signal transmission process. First, as the GPR moves close to an object, the presence of an object results in a jump in the mean value of the observed signal relative to the previous observation. Thus, we develop a high-dimensional analysis of variance (HANOVA) test to detect this change. Second, physical principles dictate that as the array moves from one stop to the next, the magnitude of this jump first increases as the array approaches the object and then decreases as the sensors move past the location of the target. This behavior is exploited in the synthesis of a sequential probability ratio test (SPRT) designed to recursively process the output of the HANOVA test as the GPR system moves down the track. The detection method is on-line implementable and has a linear computational complexity.

Once an object is detected, then the next logical step is to localize it. We use an optimized frequency-wavenumber (F-K) migration method to localize subsurface objects from the GPR array data. F-K migration coherently processes waves collected at different positions by a GPR array. It back-propagates recorded waves to the subsurface objects, according to the wave equation. Performance of F-K migration on GPR measurement depends on proper modeling of GPR signals and accurate estimation of wave propagation velocity. Because of measurement noise, random ground surface, and clutter, signal modeling and velocity estimate are not exact, therefore F-K migration may lose its resolution and accuracy. We propose an optimized method to improve performance of F-K migration. The optimized method searches for a better velocity estimate in the framework of Tikhonov regularization. The Tikhonov regularization uses minimum entropy as the constraint of the optimization process. By trying to minimize entropy of F-K migration results, better performance is achieved in terms of resolution and accuracy.

Examples from applying the HANOVA and optimized F-K migration on real data are included to demonstrate their performance.

# Contents

|          |   |          |
|----------|---|----------|
| <b>1</b> | <b>Introduction</b>   | <b>1</b> |
| 1.1      | Subsurface Sensing . . . . .                                  | 1        |
| 1.2      | Problem Statement . . . . .                                   | 3        |
| 1.3      | Proposal Organization . . . . .                               | 6        |
| <b>2</b> | <b>Literature Review</b>                                      | <b>7</b> |
| 2.1      | A Brief Survey of GPR . . . . .                               | 7        |
| 2.2      | Object Detection Using GPR . . . . .                          | 10       |
| 2.2.1    | Analysis of variance (ANOVA) . . . . .                        | 13       |
| 2.2.2    | Sequential probability ratio test (SPRT) . . . . .            | 15       |
| 2.3      | Histogram Modeling Techniques to Enhance GPR Images . . . . . | 17       |
| 2.4      | Seismic Migration and GPR . . . . .                           | 18       |
| 2.4.1    | Data acquisition . . . . .                                    | 18       |
| 2.4.2    | Exploding reflector model . . . . .                           | 18       |



|          |  |           |
|----------|--|-----------|
| 2.4.3    | Seismic migration . . . . .                                  | 20        |
| 2.4.4    | F-K migration of GPR signal . . . . .                        | 24        |
| 2.5      | Tikhonov Regularization in Optimization . . . . .            | 26        |
| <b>3</b> | <b>Forward Model</b>   | <b>29</b> |
| 3.1      | Single GPR Model . . . . .                                   | 29        |
| 3.2      | Array GPR Model . . . . .                                    | 32        |
| <b>4</b> | <b>Statistical Detection of Lanmines</b>                     | <b>33</b> |
| 4.1      | Algorithm . . . . .  | 36        |
| 4.1.1    | Cross-track processing . . . . .                             | 39        |
| 4.1.2    | Down-track processing . . . . .                              | 44        |
| 4.2      | Examples . . . . .   | 48        |
| 4.3      | Window Selection in HANOVA . . . . .                         | 52        |
| 4.4      | Concluding Remarks . . . . .                                 | 53        |
| <b>5</b> | <b>Iterative Histogram Equalization To Enhance GPR Image</b> | <b>59</b> |
| 5.1      | Introduction . . . . .                                       | 60        |
| 5.2      | Iterative Histogram Enhancement . . . . .                    | 61        |
| 5.3      | Examples . . . . .   | 62        |
| 5.3.1    | 2-D examples . . . . .                                       | 62        |
| 5.3.2    | 3-D examples . . . . .                                       | 63        |
| 5.4      | Concluding Remarks . . . . .                                 | 65        |

|          |  |           |
|----------|--|-----------|
| <b>6</b> | <b>Optimized F-K Migration to Locate Landmines</b>                                 | <b>74</b> |
| 6.1      | Algorithm . . . . .  | 75        |
| 6.1.1    | F-K migration . . . . .  | 75        |
| 6.1.2    | Regularization . . . . .   | 76        |
| 6.2      | Examples . . . . .   | 82        |
| 6.2.1    | 2-D examples . . . . .   | 82        |
| 6.2.2    | 3-D examples . . . . .   | 83        |
| 6.3      | Concluding Remarks . . . . .   | 84        |
| <b>7</b> | <b>Future Work</b>   | <b>87</b> |
| 7.1      | Sequential Detection and Localization: Analytical Performance Evaluation . . . . . | 87        |
| 7.2      | Physics and Optimization . . . . .   | 88        |
| 7.3      | F-K migration in inhomogeneous medium . . . . .                                    | 90        |
| 7.4      | Quantification of Resolution . . . . .   | 92        |

# List of Figures

|     |  |    |
|-----|--|----|
| 1.1 | Subsurface sensing using incomplete reflection data, the $z$ axis is often interchangeable with the time axis since most subsurface sensing techniques collect data in the $z$ direction as a temporal signal. . . . .                     | 2  |
| 1.2 | Migration as a mapping operation. . . . .  | 6  |
| 2.1 | GPR and its signal, a) a single GPR, b) a single trace of received GPR signals, c) a GPR array, each circle represents a pair of transmitters and receivers, d) image of GPR signals. . .  | 9  |
| 2.2 | Shows a) setup of F-K migration, waves travel at velocity $v$ , b) exploding reflector model, waves travel at velocity $v/2$ . . . . .   | 19 |
| 2.3 | Diffraction summation, a) points on an imagined hyperbola in the input plane are mapped to, b) a point in the output plane. Wavefront interference, c) a point in the input plane explodes to, d) a hyperbola in the output plane. . . . . | 21 |
| 2.4 | Shows a) setup of F-K migration, waves travel at velocity $v$ , b) exploding reflector model, waves travel at velocity $v/2$ . . . . .   | 26 |

|     |  |    |
|-----|--|----|
| 2.5 | Wave propagation velocity, a) constant velocity in the horizontal direction, b) varying velocity in the horizontal direction. . . . .  | 26 |
| 3.1 | Schematic drawing of a single GPR, transmitter and receiver. . . . .   | 30 |
| 3.2 | Geometries for determining (a) the reflecting point and (b) the refracting point, $\epsilon_1 > \epsilon_0$ . . . .  | 31 |
| 4.1 | Observation from one T/R pair, for a metal mine M20 buried at about position 20. Unit in the horizontal axis is about 7.6 cm and unit in the time axis is 0.02 ns. . . . .   | 34 |
| 4.2 | Signals from four T/R pairs, after background removal, a) pair 1, b) pair 2, c) pair 3, d) pair 4. Unit in the horizontal axis is about 7.6 cm and unit in the time axis is 0.02 ns. . . . .   | 38 |
| 4.3 | Motivating example for use of HANOVA rather than ANOVA. (a) displays sample data collected by a GPR when over an object. The transient nature of the relevant portion of the signal is clear. Unit in time is 0.02 ns. Using this signal, in(b) we display the decreasing detection rates associated with including increasing numbers of “noise” samples in the processing. Probabilities of detection vs. thresholds, solid line, a window from 200 through , ‘-+’ line, a window from 100 to 900, ‘-o’ line, no window. . . . . | 42 |
| 4.4 | Steps of deciding window $\mathbf{w}(m, n)$ and $\mathbf{y}_w(m, n)$ . . . . .   | 43 |
| 4.5 | HANOVA and SPRT processing results for metal mine data shown in Fig. 4.2. Unit in the horizontal axis is about 7.6 cm. . . . .   | 44 |
| 4.6 | Sequential processing. . . . .   | 47 |

|      |  |    |
|------|--|----|
| 4.7  | Results of a single GPR measurement above a steel object around position 50, a) raw observation, b) observation after background removal, c) ANOVA output, d) HANOVA output. In a) and b), unit in the horizontal axis is about 7.6 cm and unit in the time axis is 0.02 ns. . . .                     | 49 |
| 4.8  | More comparison between the ANOVA and HANOVA, a) ANOVA over an M19, anti-tank mine, buried at position 50, b) HANOVA over the M19, c) ANOVA over a TM62, anti-tank mine, buried to the side of the track at position 58, d) HANOVA over the TM62. Unit in the horizontal axis is about 7.6 cm. . . . . | 50 |
| 4.9  | Results of the SPRT, a buried steel object, a) output of ANOVA-SPRT, b) output of HANOVA-SPRT; a buried M19, c) output of ANOVA-SPRT, d) output of HANOVA-SPRT; a buried TM62, e) output of ANOVA-SPRT, f) output of HANOVA-SPRT. Unit in the horizontal axis is about 7.6 cm. . . . .                 | 54 |
| 4.10 | Rate of detection and rate of false-alarms in detecting metallic objects, solid line is the result of HANOVA, dashed line is the result of ANOVA, a) ANOVA vs. HANOVA, b) ANOVA-SPRT vs. HANOVA-SPRT. . . . .  | 55 |
| 4.11 | Rate of detection and rate of false-alarms in detecting plastic mines, solid line is the result of HANOVA, dashed line is the result of ANOVA, a) ANOVA vs. HANOVA, b) ANOVA-SPRT vs. HANOVA-SPRT. . . . .   | 55 |
| 4.12 | GPR array used at Dedham test site of Northeastern University, a) plane view, b) side view.  | 56 |
| 4.13 | GPR data from the Dedham test site, (a) from the left front receiver, (b) from the right front receiver, (c) signal (a) after background removal, (d) signal of (b) after background removal. Unit in time axis is 120 ps. . . . .   | 57 |

|      |  |    |
|------|--|----|
| 4.14 | ROCs of the Dedham test, solid line, HANOVA-SPRT, dash line, ANOVA-SPRT. . . . .   | 57 |
| 4.15 | Choices of window and effect on HANOVA, lower line is $k_1(m, n)$ , upper line is $k_2(m, n)$ , a)<br>window selected by an order 1 MA process, b) HANOVA result from the window to the left,<br>c) window selected by an order 4 MA process, d) HANOVA result from the window to the<br>left, e) window selected by an order 10 MA process, f) HANOVA test result from the window<br>to the left. . . . . | 58 |
| 5.1  | Flowchart of iterative histogram equalization. . . . .   | 63 |
| 5.2  | (a) Original GPR image over an EM12 landmine, (b) image after subtracting the ensemble<br>average, (c) columnwise norm of <b>(a)</b> , (d) columnwise norm of <b>(b)</b> . . . . .   | 64 |
| 5.3  | Left column, images of the IHE with median filtering at iteration 1, 3, and 6. Right column,<br>images of the IHE with median filtering at iteration 1, 3, and 6. . . . .  | 66 |
| 5.4  | (a) Norm of the IHE result without median filtering at iteration 6, (b) norm of the IHE result<br>with median filtering at iteration 6. . . . .  | 67 |
| 5.5  | Histogram of the IHE result with median filter at iteration 1 to 6, from (a) to (f). . . . .   | 68 |
| 5.6  | (a) Original GPR image over an M21 landmine, (b) image after subtracting the ensemble<br>average, (c) image of histogram equalization, (d) image of the IHE result at iteration 6. . . . .   | 69 |
| 5.7  | (a) to (f), histograms of the IHE results at iteration 1 to 6. . . . .   | 70 |
| 5.8  | (a) Original GPR image over a VS16 landmine, (b) image after subtracting the ensemble<br>average, (c) image of histogram equalization, (d) image of the IHE at iteration 6. . . . .  | 71 |

|      |  |    |
|------|--|----|
| 5.9  | (a) Cascaded GPR images over an M15 landmine, (b) cascaded images of the IHE at iteration 1, (c) cascaded images of the IHE at iteration 6. . . . .  | 72 |
| 5.10 | (a) Cascaded GPR images over a VS-22 landmine, (b) cascaded images of the IHE at iteration 1, (c) cascaded images of the IHE at iteration 6. . . . .   | 73 |
| 6.1  | Rough ground surface introduces error in F-K migration, a) a flat ground surface and correct localization, b) a rough ground surface and incorrect localization if velocities are kept constant. Solid line refers to ideal situation, dash line is what will happen in reality. . . . . | 77 |
| 6.2  | a) constant velocity in the horizontal direction, b) varying velocity in the horizontal direction.   | 79 |
| 6.3  | Image $\mathbf{p}$ , a) an image of all zeros with one non-zero element, $\mathbf{R}(\mathbf{p}) = 1$ , b)–e), images of more non-zero elements, $\mathbf{R}(\mathbf{p}) = 2.0, 3.33, 5.0, 5.88$ , respectively. . . . .   | 80 |
| 6.4  | F-K migration, a) GPR signals over a T72 mine, b) result of F-K migration, c) result of optimized F-K migration. . . . .   | 83 |
| 6.5  | F-K migration, a) GPR signals over a PMN mine, b) result of F-K migration, c) result of optimized F-K migration. . . . .   | 83 |
| 6.6  | F-K migration, a) GPR signals over an LI11 mine, b) result of F-K migration, c) result of optimized F-K migration. . . . .   | 84 |
| 6.7  | F-K migration, a) GPR signals over another LI11 mine, b) result of F-K migration, c) result of optimized F-K migration. . . . .  | 84 |
| 6.8  | 3-D example, left column, regular F-K migration image; right column, optimized F-K migration image. . . . .  | 86 |

|     |                       |    |
|-----|-----------------------|----|
| 7.1 | GPR geometry. . . . . | 90 |
|-----|-----------------------|----|



# List of Tables

|     |  |    |
|-----|--|----|
| 6.1 | $\mathbf{R}(\mathbf{p}_o)$ of F-K migration and optimized F-K migration results. . . . . | 85 |
|-----|--|----|

# Chapter 1

## Introduction

ch:introduction

The problem of detecting and localizing buried objects has received considerably amount of research interest in recent years. Of interest in this research is the development of statistical signal processing methods to detect and localize buried landmines based on data collected by a ground penetrating radar (GPR) array.

### 1.1 Subsurface Sensing

surface sensing

Subsurface sensing technique has found application in areas such as landmine and unexploded ordnance remediation, utility line mapping, and archaeological discovery. Subsurface sensing techniques includes

GPR <sup>Peters:1994,Witten:1994</sup> [1, 2], infrared imaging <sup>Uppsal1:2000,Sendur:2000</sup> [3, 4], electromagnetics/magnetics <sup>Drewniak:2000,Ozdemir:2000</sup> [5, 6], laser-induced acoustic imaging <sup>McKnight:2000,DiMarz</sup> [7, 8],

and nuclear quadrupole resonance <sup>Hibbs:2000</sup> [9] and so on. Among these techniques, GPR is widely used because it is sensitive to variations of all three electromagnetic parameters of a medium, i.e., electrical conductivity, electrical permittivity, and magnetic permeability. Therefore GPR is able to detect and locate buried

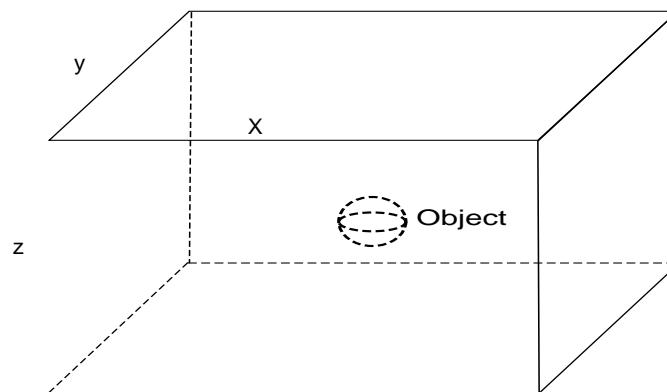


Figure 1.1: Subsurface sensing using incomplete reflection data, the  $z$  axis is often interchangeable with the time axis since most subsurface sensing techniques collect data in the  $z$  direction as a temporal signal.

objects of various kinds. GPR has been used in detecting and locating buried landmines and unexploded ordnance [Chan:1979, 10]. Other applications includes locating tunnels and other buried voids [Daniels:1988, Daniels:1989, 11, 12], trenches and contaminated fluids [Daniels:1994, 13]. All these applications can be categorized as *subsurface sensing using incomplete reflection data*. This is in contrast to subsurface sensing in magnetic resonance imaging (MRI) and electric impedance tomography (EIT) where data can be collected around the subject, which can then be categorized as *subsurface sensing using complete reflection and transmission data*. In subsurface sensing using incomplete reflection data, sensors are constrained to the  $(x, y)$  plane and task is to detect and localize objects in the  $(x, y, z)$  space, Fig. 1.1. For the purpose of illustration, from here on, the *left-hand system* of coordinates as seen in Fig. 1.1 will be used in all the ensuing discussion. This research focuses on the subsurface sensing using incomplete reflection data.

## 1.2 Problem Statement

This research intends to develop statistical method to detect and localize subsurface objects from GPR array measurement. The first goal is to develop signal processing scheme to mark buried objects in the  $(x, y)$  plane, Fig. 1.1. Once an object has been detected, then the next step is to localize it in the vertical plane, i.e., in depth, which is the second goal. At each stop, the GPR transmits electromagnetic wave and receives a reflection. The reflection is usually densely sampled in time for from 10 to 20 ns and is collected into a vector of dimensions in hundreds. This vector is called a trace or time-series in literatures of geophysics and remote sensing <sup>Peters:1994</sup> [1].

The trace consists of measurement noise, specular reflection from ground surface, clutter, and possibly object reflected signals. Measurement noise comes from imperfections of the GPR hardware, approximation in analog to digital conversion, and human error. Specular reflection is the electromagnetic waves which have bounced off of the air-ground interface. Specular reflection can be reduced by some GPR configurations such as forward-looking GPR <sup>Rappaport:2000</sup> [14], but it cannot be totally eliminated. Here clutter is defined as any undesirable components in the GPR data, except noise and specular reflection. In practice, a GPR moves along a linear track to collect a series of traces in order to find subsurface objects.

In our approach to detection, the input is a series of traces obtained sequentially as the GPR moves downtrack. Final output is a sequentially updated test statistic. The test statistic is compared to a preset threshold to determine if an object is present. The method is based on some simple electromagnetic principles and relies on statistical methods to remove noise and ground reflection in order to detect the useful signal. The method is setup in the framework of blind transient signal detection. As seen in the later part of this

proposal, reflection from a subsurface object usually displays a manifest hyperbolic curve in GPR signals. The exact shape of this hyperbola depends on object's type and position and other factors. For example, a plastic mine generally displays a weaker and shorter hyperbola than a metallic mine. A deeply buried object has a short hyperbola in the horizontal direction because its reflection can only be picked up at GPR positions close to it. For this reason, we treat the problem as a blind signal detection. On the other hand, a GPR array can only register object reflected signal in finite duration, both in the horizontal position and time. In other words, object reflected signals are transient in space and time. The reason for signals being transient in space is that GPR only collects reflected wavefield for about 20 ns, reflection from a far away object will simply not arrive in 20 ns. The object reflected signal is transient in time because it only occupies a few nanoseconds in a trace. The motivation is then to detect such a blind transient signal with a method of low computational complexity, high performance, and amenability to on-line implementation. In detail, the method consists of two steps, first, we process a trace in a "static way" and generate a temporary test statistic, second, we process the temporary test statistic sequentially, as the GPR array moves, to yield a final test statistic. Based on the final test statistic, the method is able to achieve a high probability of detection while keeping false-alarm rate low. Specifically, the first step is an generalized high-dimensional analysis of variance (HANOVA). HANOVA is closely related to the standard method of analysis of variance (ANOVA), which is usually used in testing statistical significance. HANOVA is designed to improve the performance of the ANOVA by using truncated signal. Because the object reflected signal is transient in time, a trace is truncated from both ends such that the new trace has a higher signal-to-noise ratio (SNR). Higher SNR increases probability of detection of the detector. While HANOVA is implemented step-by-step as the GPR moves forward, it does not capture the change of data from one step to the next. Therefore, in the second

part, we employ a sequential probability ratio test (SPRT) to provide real-time decision. The SPRT is a cumulative sum and able to reduce the number of false-alarms from the HANOVA. The method has a low computational load and as a sequential method, it is on-line implementable.

Once an object is detected, the next step is to localize the object in the horizontal position and depth. In localization, imaging methods can be used to reconstruct a representation of subsurface reflectivity. The input is a set of traces, i.e., a 2-D image in space-time domain. The output is an image showing subsurface reflectivity in the horizontal direction and depth, i.e., in space-space domain.<sup>1</sup> The input can be a 3-D matrix when GPR collects data on a two-dimensional grid in the horizontal plane. In that case, the output can also be a 3-D matrix, which represents subsurface reflectivity in the  $(x, y, z)$  space. Ideally, the position of the object will become a sharp, bright spot in the output. In the literature, it is usually said that the input resides in “*image space*” and the output resides in “*object space*” <sup>Gazdag:1984</sup> [15], Fig. 1.2. In this paper, double quote will always be used around the “image space” and the “object space” to avoid confusion with terms appearing in later parts.

The method used is an optimized frequency-wavenumber (F-K) migration scheme. F-K migration is a mapping operation from the “image space” to the “object space” based on the wave equation and wave propagation velocity estimation. Assuming the registered wavefield satisfies the wave equation and the velocity estimate is accurate enough, F-K migration is able to reconstruct subsurface reflectivity at any point in space and time. Originally, F-K migration was developed to reconstruct subsurface reflectivity in seismic signal processing, where it back-propagate the wavefield into the earth, up to kilometers <sup>Robinson:1983</sup> [16]. In landmine localization, GPR signals are obtained in a different manner than the seismic signals, still migration methods

---

<sup>1</sup>Strictly speaking, output is an image representing subsurface reflectivity, not a direct measure of reflectivity. This difference will become clear in later chapters.

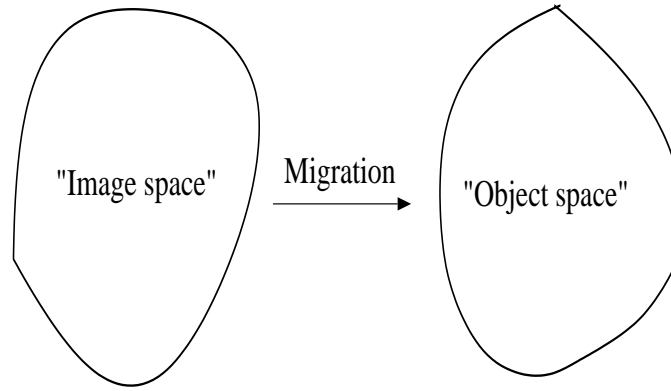


Figure 1.2: Migration as a mapping operation.

have been successfully applied on GPR signals. More details will be given in Chapter 2. Nevertheless, F-K migration has the disadvantages of low resolution and large sidelobes in the presence of measurement noise, random ground surface, and clutter in GPR data. To circumvent this problem, an optimization method is proposed to increase resolution and reduce sidelobes in F-K migration result. The optimization is implemented in the framework of Tikhonov regularization. The regularization minimizes entropy of F-K migration output and better results are obtained in terms of enhancing mainlobe and suppressing sidelobes.

### 1.3 Proposal Organization

The proposal is organized as follows. Chapter 2 reviews current GPR signal processing methods in detection and localization. Chapter 4 presents the detection method, a combination of HANOVA and SPRT. Chapter 6 describes the localization method and its optimization. Proposed future work is given in Chapter 7.

## Chapter 2

# Literature Review

terature review

In this chapter, I will briefly discuss GPR, analysis of variance, sequential probability ratio test, seismic migration and frequency-wavenumber migration, and Tikhonov regularization method in solving an optimization problem.

### 2.1 A Brief Survey of GPR

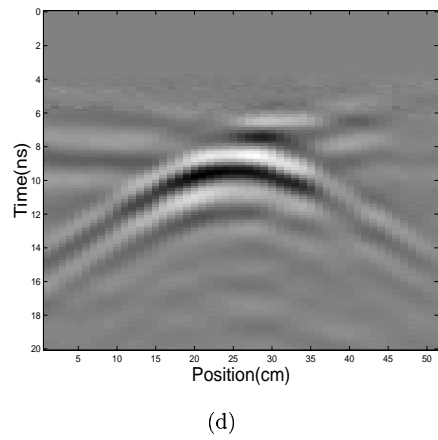
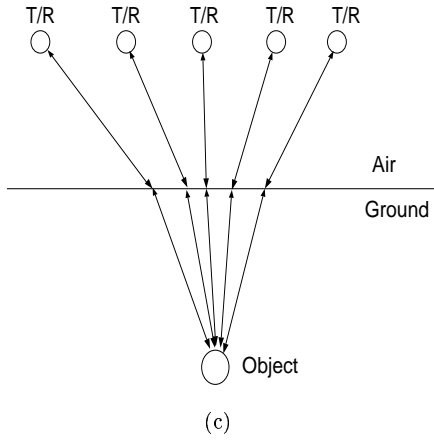
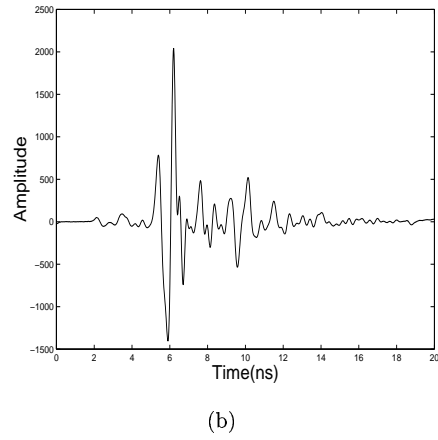
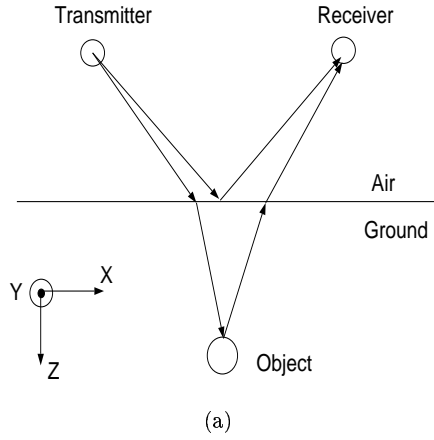
sec:survey GPR

GPR can be defined as a radar whose goal is to detect and identify structures underground <sup>Peters:1994</sup>[1]. It has been in use for about 20 years in contrast to the more than 50 year history of conventional radar <sup>Peters:1994</sup>[1]. A simple diagram of a GPR is given in Fig. 2.1(a). It consists of a transmitting antenna (transmitter) and a receiving antenna (receiver). The transmitter radiates a pulse into the ground and the receiver collects the echo for a certain time period, usually 10 to 20 ns. The transmitted pulse may be any transient signal, sine wave, steps, and Gaussian wave are all possible waveforms. Pulse widths are usually in the order of a few nanoseconds <sup>Peters:1994</sup>[1].



Compared with conventional radar, GPR has a much broader bandwidth, from a few megahertz to a few gigahertz. GPR operates at high frequency so that it can provide images of high resolution of subsurface reflectivity. At such high frequencies, electromagnetic waves are extremely vulnerable to interference. This interference can be reduced by averaging a number of GPR returns obtained as a function of time without moving the GPR [1].<sup>Peters:1994</sup> The most critical part of a GPR is the transmitting and receiving antenna. The antenna are usually in the form of dipoles, which are heavily loaded to reduce as much as possible the antenna ringing. Usually the transmitter and receiver are separated, i.e., the GPR is a bistatic radar. For typical GPR, the receiver takes the forms of a sampling system. The sampling system constructs the received signal from discrete samples of successive periods of the reflected waveform. “The sampling system makes it possible to use an amplifier with time- (or range-) dependent gain controlled by a computer prior to the sampler in order to minimize sampling noise” [1].<sup>Peters:1994</sup> Fig. 2.1(b) shows a typical received GPR signal.

Field operation of a GPR system is very simple. Commonly, a vehicle mounted GPR system (VMGPR) surveys an interested area step by step along a linear track. A VMGPR may consists of a single GPR or an array of GPR. At each step, the VMGPR operates in the following sequence: 1) the transmitter radiates a pulse into the ground and turns off, 2) the receiver turns on to collect reflected signal, 3) the receiver turns off after a short time, usually 10 to 20 ns. The data that is recorded by one receiver at one step is called a trace (or a time-series). Denote the direction of VMGPR movement as  $x$ , then the VMGPR will collect reflection in the  $(x, t)$  plane. If the VMGPR is a GPR array, a three-dimensional image of the subsurface will be generated in the  $(x, y, t)$  space. Depending on the task to perform, the step size of the VMGPR can vary from a few meters to a fractions of meters. Fig. 2.1 (c) and (d) shows a GPR array and its received signals. At positions close to the object, the array registers stronger reflections at small time-delays. At farther away



and GPR signal

Figure 2.1: GPR and its signal, a) a single GPR, b) a single trace of received GPR signals, c) a GPR array, each circle represents a pair of transmitters and receivers, d) image of GPR signals.

positions, the reflections are weaker and time-delays are large. Thus typical GPR signals show a manifest hyperbolic curve around the position of an object. Fig. 2.1 (d) confirms that the object (landmine) reflected signals are transient in two directions, the signals are clearly visible between 15 to 35 cm in the horizontal position and 6 to 14 ns in the time axis.

GPR is different from the conventional radar in that 1) GPR operates in near-field scenario, 2) most GPR antenna are close to the air/ground interface and ground reflection cannot be ignored, 3) the medium

GPR operates in is highly lossy. At a frequency of  $f$ , the attenuation factor is

$$\alpha = \frac{1}{2}\sigma(f)\sqrt{\frac{\mu}{\epsilon}} \quad (2.1) \quad \boxed{\text{eq:attenu}}$$

where  $\mu$  is the permeability,  $\epsilon$  is the permittivity, and  $\sigma$  is the conductivity of the medium. Note that the conductivity is frequency-dependent. Depending on the shape of antenna and the way it works, spreading function needs also to be considered to model the GPR signal accurately. Mathematically, if the transmitted signal is  $p(t)$ , then the signal reflected from an underground object can be approximated as  $\alpha p(t - \tau)$ , an attenuated and delayed version of  $p(t)$ .

Because soil is usually inhomogeneous and air/ground interface is rough, there are multipath reflection and refraction in GPR signal. When one includes frequency dependent conductivity at the soil, it becomes prohibitive to process the GPR signal based solely on physics principles. On the other hand, we can overcome the difficulty in modeling by exploiting the data diversity provided by a GPR array and use some basic physics principles and statistical method to look for some specific features in the GPR signals <sup>Miller:1995</sup> [17].

## 2.2 Object Detection Using GPR

ection using GPR

In the real world, GPR data are contaminated by measurement noise, specular reflection, and clutter. Though all are undesirable, noise, specular reflection, and clutter affect GPR signal processing in different ways. Noise is generally a stationary process and can be very well modeled as a stochastic process, such as an additive white Gaussian noise (AWGN). Correspondingly, existing noise reduction schemes can be used based on the assumption of the stochastic process, from moving average filter <sup>Ku:2000b</sup> [18] to Wiener filter.

Specular reflection is the reflection from the ground surface. It is usually the strongest component in GPR data. Specular reflection depends on the roughness of the ground and other characteristics of the soil, such as moisture. At best, specular reflection can be modeled as a stationary stochastic process, though it is not always true. Specular reflection makes detecting shallowly buried objects very difficult because object reflected signals are close to the specular reflection in time. On the other hand, objects deeply buried can be easily separated by time-gating, i.e., throw away specular reflection by truncating reflected signal in the first few nanoseconds and remained reflection shall contain only object reflected signal. There the problem is to detect signals of low signal to noise ratio because of large attenuation associated with deeply buried objects. Specular reflection usually reduces a detector's probability of detection. Clutter is defined as any undesirable components, except noise and specular reflection, in GPR data. Clutter, in contrast, increases the number of false-alarms of a detector. Clutter takes different forms and can appear in many ways in GPR data. When a clutter appear close to an object, it affects resolution of the detector. A clutter separated from any objects may show up as a false-alarm. In combination with noise and specular reflection, clutter generally affects the receiver operating characteristics (ROC) of the detector. The major challenge in GPR signal processing is to enhance object reflected signals and reduce clutter and specular reflection.

Current mathematical methods for the problem of object detection fall into one of three categories. First, pattern matching methods <sup>Gader:1999,Gader:2000</sup> [19, 20] employ techniques such as fuzzy set theory and neural networks. Such methods can be fast but require extensive training to function well. Moreover, performance analysis is limited to Monte-Carlo simulations. Second, image-then-detect techniques <sup>Bradley:1999</sup> [21] employ a beamforming or backpropagation approach to build an image of the subsurface which is then post-processed to detect objects. Such methods generally require the data from a full GPR scan to form an image and are thus

not well suited to on-line computations in which information is processed sequentially as the array proceeds down track. More subtly, the attenuation associated with the propagation of the GPR signal typically results in useful signal only over receivers located closest to object. Thus, methods based on beamforming which require array-based observations are not really appropriate for this problem. As with the pattern matching approaches, performance analysis tools are not readily available. Finally, there has been some very interesting work done in the area of statistical processing methods <sup>Dogaru:1998</sup> [22] where one can use models to examine quantities such as detection rates, probability of false alarm, etc.; however the techniques in <sup>Dogaru:1998</sup> [22] for instance are based on highly complex electromagnetic models for the GPR sensor and are thus computationally intensive. Signal processing in the framework of hypothesis testing has advantages of robustness, fast computation, on-line implementation, and being amenable to performance analysis. In <sup>Ku:1999, Xu:2000</sup> [23, 24], it is shown that binary hypothesis testing can be applied to detect mine by comparing received signal from neighboring radars. We model the detection problem in a typical hypotheses testing framework <sup>Helstrom:1995</sup> [25],

$$H_0 : \quad \textit{there is no object},$$

$$H_1 : \quad \textit{there is an object}.$$

The null hypothesis  $H_0$  means that there is no buried object in the field of view of the GPR array, so the total received signal is comprised of specular reflection, clutter, and measurement noise. Reflection from the air-ground interface is the dominant component of this part of the signal. The alternative hypothesis  $H_1$  indicates that there is buried object so that the received signal consists of nominal background, measurement

noise, and an object reflect signal. In the simplest mathematic form, we can write the received signals  $p$  as

$$\begin{aligned} H_0 : \quad p &= g \\ H_1 : \quad p &= s + g \end{aligned} \tag{2.2}$$

where  $s$  is the object reflected signal and  $g$  represents the sum of nominal background and measurement noise.

**sec:ANOVA**

### 2.2.1 Analysis of variance (ANOVA)

ANOVA is a body of methods to analyze data with a view to test hypotheses about the effects of one or more factors <sup>Ghosh:1970</sup>[26]. To review the basics of ANOVA, we follow the notation established above for the GPR

problem and for simplicity assume we have one received signal from a single T/R pair. Let  $\mathbf{p}$ , a vector of size  $K \times 1$ , be the received signal and assume that  $\mathbf{p} \sim N(\mathbf{s}, \sigma_g^2 \mathbf{I})$  and we wish to test  $H_0 : \mathbf{s} = \mathbf{0}$  (i.e.,

no object) vs.  $H_1 : \mathbf{s} \neq \mathbf{0}$  (i.e., an object present) where  $\mathbf{s}$  denotes the object reflected signal. Standard

ANOVA is essentially an “energy detection” scheme <sup>Fan:1996</sup>[27] where we estimate  $\mathbf{s}$  by  $\mathbf{p}$ , generate the test statistic

$u = \|\mathbf{p}\|^2$ , and compare  $u$  to a threshold,  $\gamma$ . If  $P$  exceeds the threshold,  $H_1$  is chosen, else  $H_0$  is selected.

The probability of detection of the standard ANOVA is

$$Q_d(H_1|H_1) = Q\left(\frac{\gamma - \frac{\|\mathbf{s}\|^2}{\sigma_g^2 \sqrt{2K}}}{\sqrt{1 + \frac{2\|\mathbf{s}\|^2}{\sigma_g^2 K}}}\right) \tag{2.3}$$

**eq:power**

where  $\gamma$  is the test threshold decided by setting an acceptable probability of false-alarm under  $H_0$  and  $Q$  is the complementary cumulative distribution function and is strictly decreasing <sup>Fan:1994</sup> [28]

$$Q = \int_{\gamma}^{\infty} P_1(u) du \quad (2.4)$$

where  $P_1$  is the probability density function of  $u$  under hypothesis  $H_1$ .

While easy to understand and implement, ANOVA has its limitation. Estimating  $\mathbf{s}$  by  $\mathbf{p}$  assumes that  $\mathbf{s}$  is evenly or almost evenly distributed over its full dimension. When  $\mathbf{s}$  is of high-dimensions and its nonzero samples concentrate only on a sub-dimension, we can divide  $\mathbf{p}$  into two types of fractions. One is the “*signal-rich fraction*” and the other is called the “*noisy fraction*”. If there is prior information about the location of the signal-rich fraction, better result can be achieved by carrying out ANOVA on the signal-rich fraction only. In this way, a high-dimensional problem becomes a sub-dimensional one. For historical reason, ANOVA applied on the signal-rich fraction is called *high-dimensional analysis of variance (HANOVA)* <sup>Fan:1996</sup> [27]. HANOVA has a better performance than the corresponding ANOVA in terms of probability of detection and probability of false-alarm. In reality, the length of this signal-rich fraction is not known *a priori* and there is no clear starting and ending point of the signal-rich fraction. To take advantage of HANOVA, we need a method to find about the signal-rich fraction adaptively. Recently, Fan <sup>Fan:1996</sup> [27] and Fan and Lin <sup>Fan:1998</sup> [29] proposed a scheme to adaptively truncate the original high-dimensional observation to a sub-dimension. When there is *a priori* information indicating that the first  $k_1$  dimensions of an observation contains most of signal, an

estimate of  $k_1$  is decided by

$$k_1 = \arg \max_{k_1} \frac{\sum_{k=1}^{k_1} [\mathbf{p}]_k^2}{\sigma_g^2 \sqrt{k_1}} - \sqrt{k_1} \quad (2.5) \quad \boxed{\text{eq:decide}}$$

where  $[\mathbf{p}]_k$  means the  $k$ th element of  $\mathbf{p}$ . Then the HANOVA is simply a test on the first  $k_1$  dimensions of the observation vector  $\mathbf{p}$ . In GPR application, we look for the fraction contains mostly of object reflected signals and it does not start from the beginning, so we generalize the HANOVA to search for both the start and end point of the signal-rich fraction.

### 2.2.2 Sequential probability ratio test (SPRT)

**sec:SPRT**

While HANOVA detects statistical significance at one stop of the array, it does not capture the structure of object reflected signal seen as the array moves down-track. To improve performance, we use SPRT in the second of our detection scheme. SPRT is a family of hypothesis testing methods that takes new observation into calculation as it is gathered. SPRT is a natural choice in GPR signal detection because GPR signals are usually obtained step by step. Denote the test statistic at the  $i$ th step as  $u(n)$ , then SPRT takes the form of a cumulative sum (cusum)

$$U(n) = U(n-1) + u(n). \quad (2.6)$$

Here  $U(n)$  is the final test statistic and it is compared to a preset threshold at each step to make a decision of the test result. Statistically,  $U(n)$  is a random walk process constrained to change between two thresholds,



upper threshold  $\eta_a$  and lower threshold  $\eta_b$ . Standard SPRT makes one of three decisions at each step,

$$U(n) \geq \eta_a \Rightarrow \text{declare } H_1 \text{ and stop,}$$

$$\eta_b \geq U(n) \leq \eta_a \Rightarrow \text{take another observation,}$$

$$U(n) \leq \eta_b \Rightarrow \text{declare } H_0 \text{ and stop.}$$

The false-alarm probability  $Q_0$  equals the probability under  $H_0$  that the random variable  $U(n)$  crosses the threshold  $\eta_a$  before passing below the lower threshold  $\eta_b$ . And the probability of detection  $Q_d$  is the probability that  $U(n)$ , under  $H_1$ , passes below  $b$  before exceeding  $\eta_a$ . Performance of the SPRT is decided by the selection of  $(\eta_a, \eta_b)$  and it is a difficult problem to determine  $(\eta_a, \eta_b)$  to minimize the average cost of the SPRT. Wald <sup>Helstrom:1995</sup> [25] has shown that, in approximation, the thresholds  $(\eta_a, \eta_b)$  required for attaining the reliability  $(Q_0, Q_d)$  are

$$\eta_a \approx \ln \left[ \frac{Q_d}{Q_0} \right] \tag{2.7}$$

$$\eta_b \approx \ln \left[ \frac{1 - Q_d}{1 - Q_0} \right]. \tag{2.8}$$

Since in GPR application, we are only interested in detecting objects, SPRT can be set to test against one threshold  $\eta$  such that

$$U(n) < \eta \Rightarrow \text{take another observation,}$$

$$U(n) \geq \eta \Rightarrow \text{there is an object, stop.}$$

In contrast to fixed sample size tests, SPRT can reduce the number of samples required to make a decision.

## 2.3 Histogram Modeling Techniques to Enhance GPR Images

sec:histogram

In GPR signal (image) processing, the biggest challenge is to effectively remove the specular reflection from the ground, i.e, the background. The background can be removed in two directions,  $x$  and  $t$  respectively. To remove the background in the  $x$  direction, two often used methods are subtraction of the ensemble average of a GPR image or subtraction of a running average (moving average filter) of the image. Both methods have the advantage of simple calculation and the moving average filter can be implemented sequentially. But both methods have deteriorated performance when the ground surface is relatively rough. In that situation, both methods cannot remove as much background as possible and there are remaining background sections in the image and can be mistakenly identified as a valid target. To remove the background in the  $t$  direction, the method used is time-gating. In time-gating, when there is prior information about the depth of the buried landmines, one can calculate the time required for the landmine reflected signal reach the GPR receiver and discard all the signals arriving before that time. Two problems arise in using the time-gating techniques, first, there is usually no prior information of the depth of the buried landmines; second, when the landmines are buried close to the ground surface, even knowing the depth may not be enough to guarantee a good time-gating because of the ground roughness. On the other hand, if the GPR images can be enhanced in some way at first, then both kinds of background removal can be more effectively.

One kind of image enhancement is histogram modeling techniques (e.g. histogram equalization). Histogram equalization modifies the dynamic range and contrast of an image by altering the image such that its

intensity histogram has a desired shape. Histogram equalization employs a monotonic, non-linear mapping which re-assigns the intensity values of pixels in the input image such that the output image contains a uniform distribution of intensities (i.e. a flat histogram).

## 2.4 Seismic Migration and GPR

sec:migration

### 2.4.1 Data acquisition

data acquisition

Migration is geophysical inversion method that (re)constructs an image of subsurface reflectivity from measurement made at the earth's surface [Robinson:1983, 16]. There are different types of migration methods. For each specific method, modification is necessary depending on the manner of data acquired. All the data are collected by sensors consisting of transmitter and receiver. For the purpose of illustration, we assume sensors reside on the horizontal axis  $x$  and let  $x_s$  be the coordinate of the transmitter and  $x_r$  be the coordinate of the receiver. We then the half-offset coordinate of the transmitter and receiver as  $h = (x_s - x_r)/2$ . When the transmitter and receiver are co-located, the half-offset  $h = 0$  and the transmitter and receiver are said to be in zero-offset setup. Zero-offset setup corresponds to monostatic radar system in GPR. In zero-offset setup, waves travel the same path from the transmitter to the object and from the object to the receiver.

### 2.4.2 Exploding reflector model

reflector model

In practice, transmitters and receivers of the GPR array take turns to transmit and receive electromagnetic waves. For mathematical treatment, we can assume that all transmitters are activated at the same time, but each receiver only records signals originating from the same transmitter-receiver pair. We can further

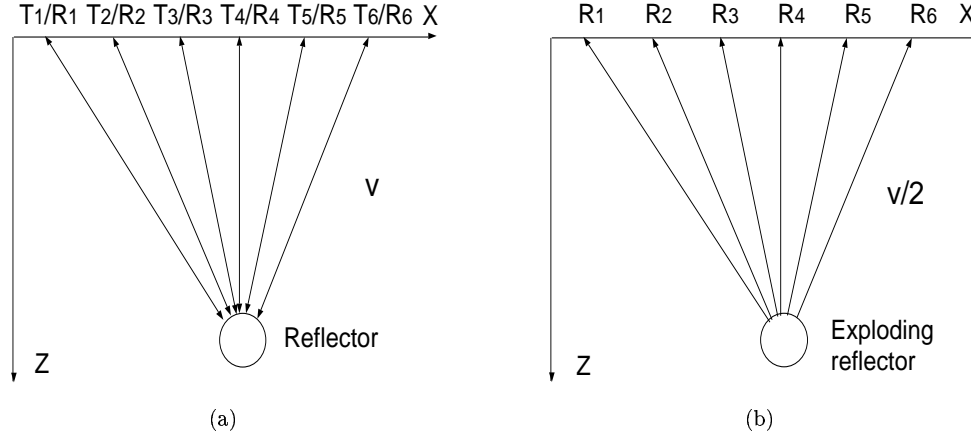


Figure 2.2: Shows a) setup of F-K migration, waves travel at velocity  $v$ , b) exploding reflector model, waves travel at velocity  $v/2$ .

fig:FK model

assume that there is no transmitter at the surface, instead the object becomes a source. At time zero, the object transmits a spherical wave in all directions and after the transmission, the object disappears. What remains is a wavefield propagating in the soil. This assumption is called “exploding reflector model” <sup>Gazdag:1984</sup> [15] and has been applied successfully in seismic signal processing. This assumption is not exactly true for GPR, but as we will show later on, surprisingly good results can still be obtained by applying the assumption to our problem. For distinction, we call the transmitter–object–reflector model as the “full model”, Fig. 2.2(a).

In the exploding reflector model, there is only up-going waves and waves travel at the half velocity as it does in the full-model. This conversion is necessary to make the exploding reflector model consistent with the full-model in describing the reflected wavefield, Fig. 2.2(b). The up-going spherical waves reach the corresponding receiver after a certain time-delay. Different pairs of transmitters and receivers register the reflected wave at different time-delays. The reflected waves form an approximate hyperbolic curve in the GPR signal as seen in Fig. 2.1(d). When done correctly, seismic migration collapses the hyperbola and puts

the position of the landmine at the tip of hyperbola.

### 2.4.3 Seismic migration

Seismic migration

Migration is usually used to map underground reflectivity in the depth of hundreds of meters to kilometers. It is well known that in lossy medium (soil), attenuation of a propagating wave is proportional to its frequencies, (2.1). At such depth, electromagnetic waves attenuates too much in the soil to be useful. Instead, acoustic waves are used because their frequencies are low. Though electromagnetic waves and acoustic waves are different in the level of attenuation, they obey the same physical principles such as Snell's law. As we will see later on, this factor makes it possible to generalize migration methods to GPR application.

There are many migration methods and they all attempt to collapse the hyperbola seen in Fig. 2.1(d) to a point, which represents the true position of the object. Classical methods include diffraction summation migration and wavefront interference migration. In diffraction summation migration, for each point in the object plane, a diffraction hyperbola is constructed and points on the hyperbolic curve are summed together. This process is repeated for every point in the object plane to generate one migration image, Fig. 2.3(a) and (b). While diffraction summation can be considered as a method collapsing hyperbola to a point, wavefront interference migration works in the opposite way. It takes a seismic trace from the data plane and distribute it over a semi-circle in the object plane, Fig. 2.3(c) and (d). Repeating the above process for every seismic trace and adding the results together will generate a migration image. Mathematically, diffraction summation is a “many to one” mapping and wavefront interference is a “one to many” mapping. Both methods had some success in the late 1960s and early 1970s, but they are not based on strict wave model <sup>Gazdag:1984</sup> [15].

On the other hand, there are types of migration methods based on the wave equation, such as frequency-

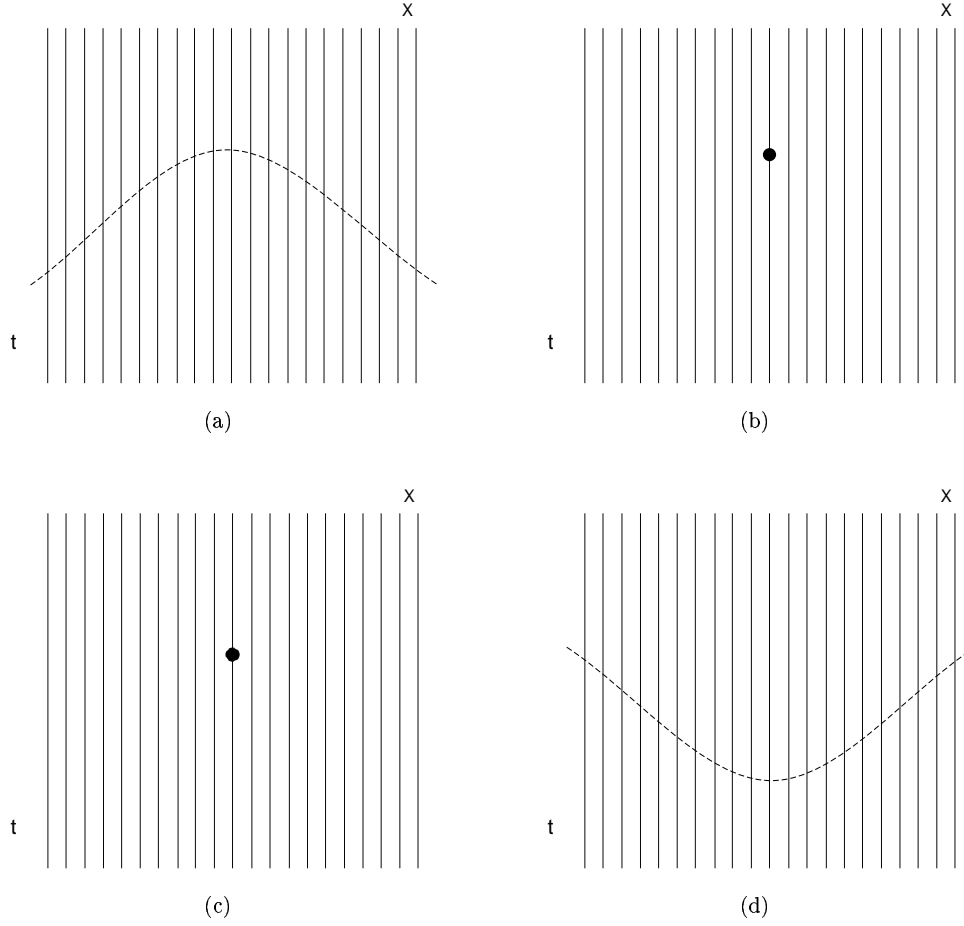


Figure 2.3: Diffraction summation, a) points on an imagined hyperbola in the input plane are mapped to, b) a point in the output plane. Wavefront interference, c) a point in the input plane explodes to, d) a hyperbola in the output plane.

seismic migration

wavenumber (F-K) migration, space-time migration, and Kirchhoff migration. The idea is to use the wave equation to back-propagate the wavefield. Assuming there is an exploding reflector and it activates at time zero, and denote wavefield measured at  $z = 0$ , i.e., at the ground surface, as  $p_i(x, z = 0, t)$ , subscript “i” means the “image space”. F-K migration solves the wave equation by differentiation in Fourier domain.

Because  $v$  is assumed constant, we can take the Fourier transform of  $p_i(x, z, t)$  with respect to  $x$  and  $t$ ,

$$P_i(k_x, z=0, \omega) = \int_{-\infty}^{\infty} \int_{-\infty}^{\infty} p_i(x, z=0, t) \exp[-j(k_x x + \omega t)] dx dt \quad (2.9) \quad \boxed{\text{eq:FFT}}$$

where  $k_x$  is the horizontal wavenumber and  $\omega$  is the frequency. Fourier transform turns differentiation into multiplication,

$$\frac{\partial^2 p_i}{\partial x^2} \xrightarrow{\mathcal{F}} (-jk_x)^2 P_i \quad (2.10)$$

and

$$\frac{\partial^2 p_i}{\partial t^2} \xrightarrow{\mathcal{F}} (-j\omega)^2 P_i \quad (2.11)$$

then we can write (6.1) as

$$\frac{1}{v^2} (-j\omega)^2 P_i = (-jk_x)^2 P_i + P_i'' \quad (2.12)$$

where  $P_i''$  represents the second order partial derivative of  $P_i$  with respect to  $z$ . Rearranging the above equation gives

$$P_i'' + \left[ \frac{\omega^2}{v^2} - k_x^2 \right] P_i = 0. \quad (2.13)$$

Now we can define the vertical wavenumber  $k_z(\omega, v)$  as <sup>Robinson:1983</sup> [16].

$$k_z(\omega, v) = \left[ \frac{\omega^2}{v^2} - k_x^2 \right]^{\frac{1}{2}}. \quad (2.14) \quad \text{eq:extrap}$$

The vertical wavenumber  $k_z$  represents the dispersion relations of the one-direction wave equation <sup>Gazdag:1984</sup> [15]. By finding  $k_z(\omega, v)$  we transform the problem from the space-time domain to the space-space domain and is able to find the wavefield  $p_o(x, z, t = 0)$ , subscript “o” denotes the “object space”. In summary, F-K migration has three steps,

1. Take Fourier transform of  $p_i(x, z = 0, t)$  with respect to  $x, t$ .
2. Find the vertical wavenumber  $k_z(\omega, v)$  as in (2.14).
3. Inverse Fourier transform to obtain  $p_i(x, z, t = 0)$  as

$$p_o(x, z, t = 0) = \frac{1}{(2\pi)^2} \int_{-\infty}^{\infty} \int_{-\infty}^{\infty} P_o(k_x, \omega) \exp[j(k_x x + k_z(\omega, v)z)] dk_x d\omega. \quad (2.15)$$

The assumption of above procedure is that velocity is constant in the vertical and horizontal direction and also there is no ground interface. As we shall see later on, this assumption is not true in GPR application.

Since F-K migration is computed in discrete form on computer, we can write the  $p_i(x, z = 0, t)$  as a matrix  $\mathbf{p}_i$  of size  $M \times N$ ,  $x = x_1, \dots, x_N, t = t_1, \dots, t_M$ , then the above steps of F-K migration can be summarized as

1.  $\mathbf{P}_i(k_x, \omega) = \text{FFT}\{\mathbf{p}_i(x, t)\}$ .



2. Convert the integral over  $\omega$  to an integral over  $k_z(\omega, v)$  by letting

$$k_z(\omega, v) = \left[ \frac{\omega^2}{v^2} - k_x^2 \right]^{\frac{1}{2}}.$$

3.  $\mathbf{P}_o(k_x, k_z) = \mathbf{P}_i(k_x, k_z(\omega, v))$ .

4.  $\mathbf{p}_o(x, z) = \text{IFFT}\{\mathbf{P}_o(k_x, k_z)\}$ .

One key advantage of F-K migration is that using a Fourier transform differential operations transform into algebraic operations and step 1 and 3 can be quickly computed by fast Fourier transform.

Regular F-K migration has the disadvantage of losing resolution due to measurement noise, random ground surface, and clutter in GPR signals and inaccurate estimation of velocity.

#### 2.4.4 F-K migration of GPR signal

Most GPRs are technically bistatic, i.e., its transmitters and receivers are separated. However, when the transmitter and receiver are closely positioned to each other, mathematically, we can treat the GPR as a monostatic radar system and that will be the model we use in this paper. Some other assumptions about the wave-equation migrations are <sup>Jakubowicz:1983</sup>[30]

1. Sensors are located at the surface of ground.
2. The signal being processed is free of noise and clutter.
3. Soil is homogeneous, therefore wave has a constant propagation velocity.

Of the above assumptions, the first two are never true in GPR application. GPRs are usually at some height above the ground, therefore ray path is bending at the ground surface. Noise and clutter in GPR signals usually distort the hyperbolic curve assumed in F-K migration and can make the migration result blurred and focusing at wrong places. Wave propagation velocity is not always constant. In seismic signal process, when soil is horizontally stratified, a smooth root-mean-square (rms) velocity <sup>Gibson:1983,Gazdag:1978</sup> ~~[[31,32]~~ is usually used. The use of rms velocity is less helpful in GPR application on landmine localization because landmines are usually buried in shallow depth and the surrounding soil is often not horizontally stratified but quite inhomogeneous. Another assumption of F-K migration is that ground surface is flat. While such assumption may be true in oil well exploration and subsurface pipe mapping, it is not so in landmine localization where ground surface is usually rough. Rough ground surface will introduce random time-delays to the GPR signals and makes the hyperbolic curve usually seen in GPR signals distorted.

In GPR application, the wavefield model is more complicated. Fig. 2.4 shows the corresponding F-K migration model used in GPR application. Here waves travel two different paths, one in the air and one in the soil. The ground reflection makes the wave-equation no longer valid. Nonetheless, using F-K migration directly in this scenario has achieved very good results <sup>Yu:1996,Holzrichter:2000</sup> ~~[[33,34]~~. Obviously, improvement is possible if above mismatches can be mediated in some way. That is why we turn to optimization theory to find a modification of F-K migration.

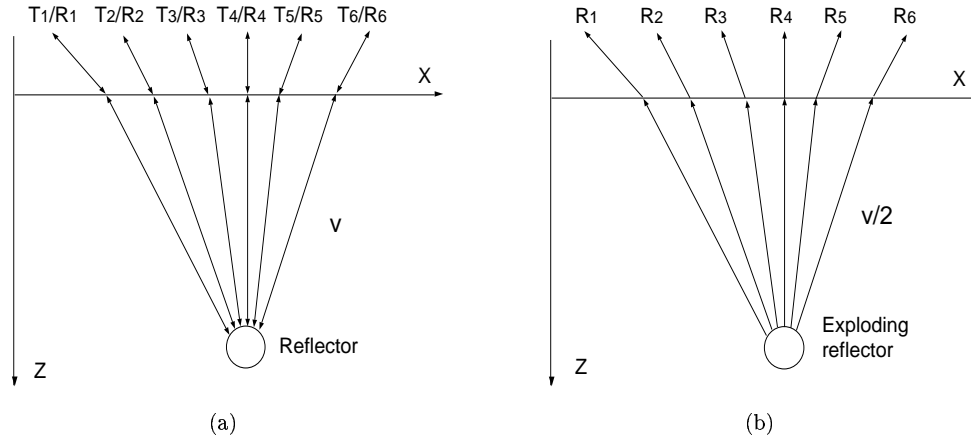


Figure 2.4: Shows a) setup of F-K migration, waves travel at velocity  $v$ , b) exploding reflector model, waves travel at velocity  $v/2$ .

## 2.5 Tikhonov Regularization in Optimization

Because of aforementioned mismatches, it appears that using one constant velocity across the horizontal direction is sub-optimal in F-K migration. One way of optimizing F-K migration is to use different velocities at different GPR positions, Fig. 2.5. Making velocities depend on GPR positions, it is expected to take into

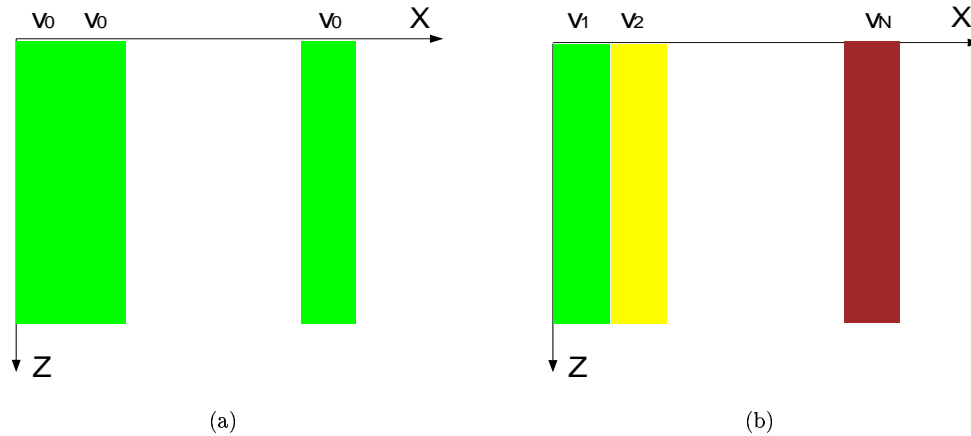


Figure 2.5: Wave propagation velocity, a) constant velocity in the horizontal direction, b) varying velocity in the horizontal direction.

consideration of rough ground surface and clutter to some extent. As a result, the F-K migration output shall consist of a sharp mainlobe and suppressed sidelobes. As will be discussed in Chapter 6, an F-K migration output with enhanced mainlobe and suppressed sidelobes has a smaller entropy. Therefore, in searching of a better velocity estimation, the process is constrained to minimize entropy of the F-K migration output. Method of Tikhonov regularization is well suited to solve this kind of optimization problem. Denoting the new velocity vector of length  $N$  as  $\mathbf{v}$ , Tikhonov regularization then looks for a solution to the following cost function

$$\min_{\mathbf{v}} \|\mathbf{v} - \mathbf{v}_0\|_2^2 + \lambda^2 \mathbf{R}(\mathbf{p}_0). \quad (2.16)$$

eq:object

where  $\lambda$  is a *regularization parameter* and  $\mathbf{R}$  is a *regularization operator*, usually chosen to be the identity matrix, a discrete approximation of the first or second order derivative operator, or entropy or inverse of entropy of  $\mathbf{p}_0$ . The first term is a measurement of change of velocity such that the change shall be small. It is referred to as a measurement of fidelity to the GPR signals. The second term penalizes some measure of F-K migration output such that the final result shall have the characteristics we would like to have. The relative importance between these two terms is controlled by the regularization parameter  $\lambda$ . As  $\lambda \rightarrow 0$ , we demand that  $\mathbf{v}$  stay close to  $\mathbf{v}_0$ . On the other hand, as  $\lambda \rightarrow \infty$ ,  $\mathbf{v}_0$  plays a limited role in influencing  $\mathbf{v}$  and  $\mathbf{v}$  is solely determined by minimizing  $\lambda^2 \mathbf{R}(\mathbf{p}_0)$ .

In Tikhonov regularization, proper selection of the regularization parameter is a non-trivial problem [35,36]. A regularization parameter too small will cause under-regularization, i.e., the optimization problem degenerates into a regular least-square problem. On the other hand, a regularization parameter too large

Belge:1998,Har

makes the problem over-regularized, where output displays little fidelity to the data.

## Chapter 3

# Forward Model

h:forward model

In this chapter, we introduce a forward scattering model. First, a simple GPR model based on ray theory is presented. Then an array GPR model is developed.

### 3.1 Single GPR Model

imple GPR model

To detect and localize mines, a ground penetrating radar array is implemented. Fig. 3.1 shows a typical single GPR system with the signals it generates [37]. In this paper we assume a simplified model where the signal seen by the receiver is composed of at most two components. The first signal is the reflected signal from the ground and is always present in the data. The second component (if it exists) is the reflected contribution from an object in the field of view of the array.

The received signal,  $\phi(t)$ , is taken to be the sum of delayed and attenuated versions of two “template” signals indicating the nominal behavior of the ground bounce signal and the nominal behavior of a signal

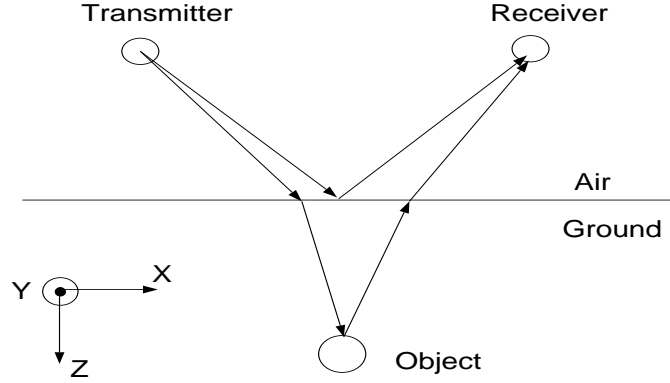


Figure 3.1: Schematic drawing of a single GPR, transmitter and receiver.

fig:singl

arising from scattering from a mine. Mathematically we have

$$\phi(t) = a\psi_g(t - \tau_g) + b\psi_m(t - \tau_m) \quad (3.1)$$

eq:delaye

where  $\psi_g$  and  $\psi_m$  are the nominal ground bounce and mine reflected signal(mine signal),  $a$  and  $b$  are attenuation factors,  $\tau_g$  is the delay of ground reflection, and  $\tau_m$  is the delay of the mine signal. Note that if no mine is present,  $\phi$  is just equal to the first term of Eq. 3.1.

To find the delays and the attenuation factors we assume that the propagation of signal from the transmitter to the receiver can be described using a ray-optics-type model shown in Fig. 3.1. That is, the ground bounce is composed of signal reflected from the interface at the specular point midway between the transmitter and receiver while the four-part path of the mine component of the signal can be determined via the judicious use of Snell's law.

To begin, the  $\tau_g$  and  $\tau_m$  are determined by the travel time of two-way paths and can be calculated as

$$\text{Delay} = \frac{\text{2-way path length}}{\text{velocity of the wave}}. \quad (3.2)$$

To find  $\tau_g$  and  $\tau_m$ , we need to locate reflecting point and refracting point shown in Fig. 3.2. Let media 1

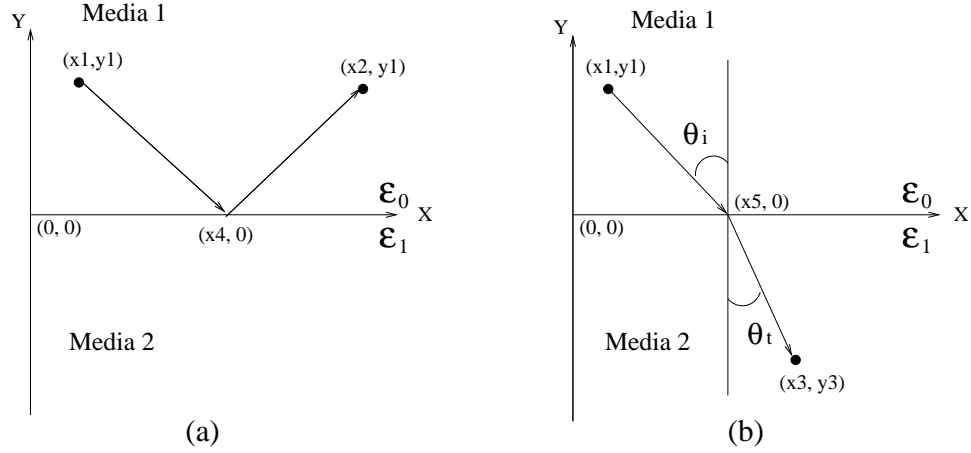


Figure 3.2: Geometries for determining (a) the reflecting point and (b) the refracting point,  $\epsilon_1 > \epsilon_0$ .

fig:snell

be air and media 2 be soil, with electric permittivity  $\epsilon_0$  and  $\epsilon_1$ , respectively, Fig. 3.2.(a), the reflecting point on the boundary between two points  $(x_1, y_1)$  and  $(x_2, y_1)$  in media 1 is simply the mid-point  $(x_4, 0)$ , where

$$x_4 = \frac{x_1 + x_2}{2}.$$

For the refracting point, according to Snell's law, for a source located at  $(x_1, y_1)$  in media 1 and target at  $(x_3, y_3)$  in media 2, the refracted ray from source to target must intersect boundary at a point  $(x_5, 0)$ , Fig. 3.2.(b), such that <sup>Rappaport:1996</sup>[38]

$$\frac{Re\{\epsilon_1\}}{\epsilon_0} = \frac{\frac{(x_1 - x_5)^2}{(x_1 - x_5)^2 + y_1^2}}{\frac{(x_3 - x_5)^2}{(x_3 - x_5)^2 + y_3^2}}. \quad (3.3)$$

Solution of this quartic equation has four roots. By Fermat's principle, which states that of all possible paths joining two given points on a wave path, the wave path has actual least travel time, we can discard three physically impossible roots and retain the true refracting point. Once the reflecting point and the refracting



point are established, the delay  $\tau_g$  and  $\tau_m$  can be found as,

$$\tau_g = 2 \frac{\sqrt{(x_1 - x_4)^2 + y_1^2}}{c} \quad (3.4)$$

$$\tau_m = 2 \frac{\sqrt{(x_1 - x_5)^2 + y_1^2}}{c} + 2 \frac{\sqrt{(x_3 - x_5)^2 + y_3^2}}{c/Re\sqrt{\epsilon_1}} \quad (3.5)$$

eq:speed

where  $c$  is the speed of light in air and  $\frac{c}{\sqrt{Re\{\epsilon_1\}}}$  is the traveling speed of wave in soil.

In addition to the time delays, the received signal  $\phi(t)$  has an amplitude reduction caused by propagation through the soil as well as geometric spreading as it traverses both the air and the earth. In soil, the wave attenuates exponentially with the distance it travels,  $e^{-\alpha_s d}$ . The quantity  $\alpha_s$  is the attenuation constant of the soil which is related to the conductivity and permittivity of the medium [Balanis:1989] while  $d$  is the distance the wave travels in the earth. We assume geometric spreading results in an inverse path length amplitude reduction. Referring to the setup of Fig. 3.2, then we have the overall amplitude reduction factors given by

$$a = \frac{1}{2\sqrt{(x_1 - x_4)^2 + y_1^2}} \quad \text{and} \quad b = \left( \frac{e^{-\alpha_s \sqrt{(x_3 - x_5)^2 + y_3^2}}}{\sqrt{(x_1 - x_5)^2 + y_1^2} + \sqrt{(x_3 - x_5)^2 + y_3^2}} \right)^2.$$

## 3.2 Array GPR Model

array GPR model

In practice, GPR usually moves along a linear track.

## Chapter 4

# Statistical Detection of Lanmines

ch:detection

Here we consider detection methods with an eye toward approaches that could be used in real-world scenarios. Our interests are in techniques possessing three important characteristics. First, to reflect the manner in which GPR data are acquired and the nature of the GPR mission, the algorithms should be causal in that they need only the data at the current and previous sensor position to determine whether an object is present in the field of view of the sensor. Second, they should be of low complexity. Preferably the number of calculations would grow linearly with the size of the data set. Finally, the processing schemes should be robust to uncertainties in the GPR environment and hence the particular detailed structure of the received signals.

Here we consider a statistical, transient detection approach. By “transient” we mean that the signals of interest are manifest in the GPR data for a small number of sensor positions and for relatively few samples in any received waveform. For example, in Fig. 4.1 we plot raw observations obtained by one T/R pair

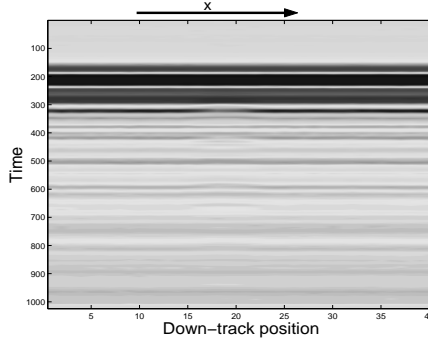


Figure 4.1: Observation from one T/R pair, for a metal mine M20 buried at about position 20. Unit in the horizontal axis is about 7.6 cm and unit in the time axis is 0.02 ns.

fig:image

from an EG&G GPR system [40], over an M20 metal mine. Each column of this image is a time-series of observations for a given stop of the array. It is seen that the received GPR signal is transient in two ways. First, for each time-series (i.e. for each column of the image) containing an object signal, the signal appears only in a brief window, roughly from samples 300 to 700. The reason is that the object signal always comes after the signal arising from the bounce off of the air-ground interface and attenuates quickly in lossy media. Second, the object signal shows up only at a few down-track positions of the GPR array, specifically locations 15 through 25. In both cases, the appearance of object signal changes the mean value of the data. Our method for object detection then is based on detecting change in this mean first in the cross-track direction and then in the down-track direction.

More specifically our approach consists of two parts. First, at each down-track position of the array, we process the data among all T/R pairs to generate one test statistic. We use high-dimensional analysis of variance (HANOVA) to test whether the data consists of reflected signal from a buried object. The HANOVA is a generalized version of standard analysis of variance (ANOVA), which is a method for testing hypothesis about means of random vectors [27, 29]. Second, a sequential probability ratio test (SPRT) is

applied to process the statistic of the HANOVA as the array moves down-track. The SPRT is a recursive statistical hypothesis testing technique that provides early indication of the onset of changes in a time series. The output of the SPRT is compared with a threshold. If it exceeds the threshold, a detection is declared, otherwise, the GPR array moves one more step down-track and new data are collected and processed in the above manner <sup>Helstrom:1995</sup> [25].

As explained in greater detail below, our approach does in fact satisfy the three requirements we discussed previously. It is causal and has computational complexity that grows linearly with the size of the data. Moreover, we show through real-data examples that it is robust, requiring little in the way of training and able to successfully address the object detection problem for a number of GPR systems operating in a wide range of environments. We do stress here that the algorithm in this paper is intended *only* to find anomalies beneath the GPR array and *not* to solve the far more challenging classification problem. Thus, from a practical perspective our approach will serve well as an efficient “pre-screener” in a larger automatic target detection algorithm suite. Finally, our method is motivated by landmine detection using GPR, however it can also be used in other detection application, such as laser-induced acoustic subsurface objects detection <sup>Shi:1999</sup> [41].

Section 4.1 discusses the problem formulation and our method. Section 4.2 gives some examples of using the method in different situations. Field data from different radar configurations and test sites are used to show how the algorithm works. Conclusion and direction of future work are given in Section 4.4.

## 4.1 Algorithm

To begin, we consider a single GPR T/R pairs as shown in Fig. 2.1(a). After each transmission, the receiver collects an echo for a certain amount of time. Depending on the presence of an object, there are either three or four components in the echo. One is measurement noise, assumed to be white and Gaussian. Another is specular reflection from the ground-air interface. The third component is clutter, which is defined as any undesirable signal except the noise and specular reflection. The fourth component is object signal, reflection from a buried object.

For the GPR array shown in Fig. 2.1(c), assume we have  $M$  GPR T/R pairs surveying an area in  $N$  steps, the task is to use present and previous array measurement to detect buried mines as the array moves down-track. At each down-track position, we model the array detection problem in a typical hypotheses testing framework <sup>[Helstrom:1995](#)</sup> [25],

$$H_0 : \quad \text{there is no object,}$$

$$H_1 : \quad \text{there is an object.}$$

The null hypothesis  $H_0$  means that there is no buried object in the field of view of the GPR array, so the total received signal is comprised of specular reflection, clutter, and measurement noise. The alternative hypothesis  $H_1$  indicates that there is buried object so that the received signal consists of noise, specular reflection, clutter, and an object signal.

In this paper we assume that most of specular reflection and noise have been removed via a preprocessing stage. The most used methods are casual methods, such as subtraction of a moving average from the

observation [24]<sup>Ku:2000</sup>, and non-causal methods, such as subtraction of an ensemble average from the observation [23, 42]<sup>Ku:1999, El-She</sup>. In this paper, a moving average (MA) filter is used.

In practice, the receiver collects time-samples of the reflection and stores it as a vector. For convenience, we use vector notation in our discussion, i.e.,  $\mathbf{y}(m, n)$  is a column vector representing observation of the  $m$ th T/R pair at the  $n$ th down-track position. The length of  $\mathbf{y}(m, n)$  is  $K$ , the number of samples in time. Fig. 4.2 shows the received signal after the background removal by a MA filter.<sup>1</sup> We then have the hypothesis test

$$\begin{aligned} H_0 : \quad & \mathbf{y}(m, n) = \mathbf{g}(m, n) \\ H_1 : \quad & \mathbf{y}(m, n) = \mathbf{s}(m, n) + \mathbf{g}(m, n) \end{aligned} \tag{4.1} \quad \boxed{\text{eq:1}}$$

where  $m = 1, \dots, M$ ,  $n = 1, \dots, N$  are positions of GPR,  $\mathbf{y}(m, n)$  is the vector observation of the  $m$ th T/R pair at the  $n$ th stop,  $\mathbf{s}(m, n)$  is the assumed signal due to presence of buried object,  $\mathbf{g}(m, n)$  is assumed to be a white Gaussian noise with a zero mean, and covariance matrix  $\sigma_g^2 \mathbf{I}$ , where  $\mathbf{I}$  is the identity matrix of size  $K$  and independent of  $(m, n)$ .

The statistical assumptions about  $\mathbf{g}(m, n)$  are not strictly accurate in describing the noise in a GPR signal. For example the background removal process will not be perfect leaving a component of correlated “clutter” in the data which may or may not possess Gaussian statistic. Despite the mismatch, the use of the additive white Gaussian noise model is useful for a number of reasons. This model allows us to develop an algorithm for object detection which is firmly rooted in Gaussian-based statistical decision theory and

---

<sup>1</sup>For the purpose of illustration, in this section we use field data from a buried metal mine to illustrate clearly the concept under consideration. Examples which demonstrate better the utility of our approach on more challenging problems, including buried plastic mines, are given in Section 4.2.

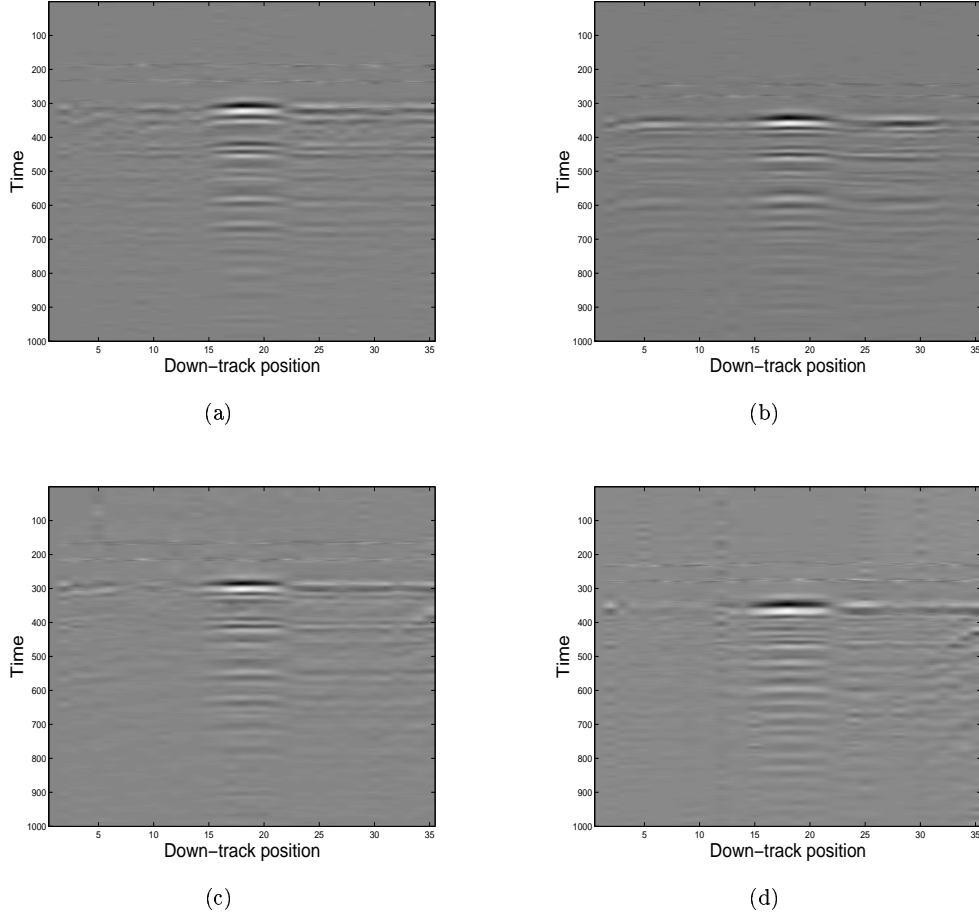


Figure 4.2: Signals from four T/R pairs, after background removal, a) pair 1, b) pair 2, c) pair 3, d) pair 4. Unit in the horizontal axis is about 7.6 cm and unit in the time axis is 0.02 ns.

background removal

which can be generalized in the future for more complex noise processes. Moreover, the complexity of such algorithms is quite low making them well suited for real-world implementation. Finally, test results in Section 4.2 from real field data demonstrate that the method is quite effective in detecting objects. Thus, the Gaussian noise model is shown to work in practice. While it may be interesting to explore other, more accurate models for the sensor noise to determine for example what can be gained in terms of performance and what would be lost in terms of computational complexity, such an effort is beyond the scope of the work

in this paper.

Based on the previous discussion, after background removal the hypotheses test in (4.1) may be written as

$$\begin{aligned} H_0 : \quad & \mathbf{y}(m, n) \sim N(\mathbf{0}, \sigma_g^2 \mathbf{I}) \\ H_1 : \quad & \mathbf{y}(m, n) \sim N(\mathbf{s}(m, n), \sigma_g^2 \mathbf{I}), \quad m = 1, \dots, M, \quad n = 1, \dots, N \end{aligned} \tag{4.2} \quad \boxed{\text{eq:2}}$$

where the notation  $\mathbf{y} \sim N(\bar{\mathbf{x}}, \mathbf{R}_g)$  indicates that  $\mathbf{y}$  is distributed as a Gaussian random vector with mean  $\bar{\mathbf{x}}$  and covariance matrix  $\mathbf{R}_g$ .

As stated in section 1.2, we take a two-step approach to the processing of  $\mathbf{y}(m, n)$ . First for each  $n$  we use the HANOVA procedure to generate a single test statistic,  $Y(n)$ , from the data from all T/R pairs. Second, a recursive, sequential detection scheme is employed to process  $Y(n)$  as we proceed down track in order to determine where objects are present.

#### 4.1.1 Cross-track processing

track processing

We begin by discussing the use of HANOVA to process data in the cross-track direction. HANOVA is a generalized version of analysis of variance (ANOVA). ANOVA is a body of methods to analyze the data with a view to test hypotheses about the effects of one or more factors <sup>Ghosh:1970</sup>[26]. To review the basics of ANOVA, we follow the notation established above for the GPR problem and for simplicity assume we have one data vector from a single T/R pair of size  $K \times 1$ ,  $\mathbf{y} \sim N(\mathbf{s}, \sigma_g^2 \mathbf{I})$  and we wish to test  $H_0 : \mathbf{s} = \mathbf{0}$  (i.e., no object) vs.  $H_1 : \mathbf{s} \neq \mathbf{0}$  (i.e., an object present)<sup>2</sup>. Standard ANOVA is essentially an “energy detection” scheme <sup>Fan:1996</sup>[27] where we estimate  $\mathbf{s}$  by  $\mathbf{y}$ , generate the test statistic  $Y = \|\mathbf{y}\|^2$ , and compare  $Y$  to a threshold,  $\gamma$ . If  $Y$  exceeds

---

<sup>2</sup>For notational simplicity, we drop the explicit dependence of all quantities on  $m$  and  $n$  in this discussion



the threshold,  $H_1$  is chosen, else  $H_0$  is selected. The probability of detection of the standard ANOVA is

$$P_d(H_1|H_1) = Q\left(\frac{\gamma - \frac{\|\mathbf{s}\|^2}{\sigma_g^2 \sqrt{2K}}}{\sqrt{1 + \frac{2\|\mathbf{s}\|^2}{\sigma_g^2 K}}}\right) \quad (4.3) \quad \boxed{\text{eq:power}}$$

where  $\gamma$  is the test threshold decided by setting an acceptable probability of false-alarm under  $H_0$  and  $Q$  is

the complementary cumulative distribution function and is strictly decreasing <sup>Port:1994</sup> [28].

Recently, Fan <sup>Fan:1996</sup> [27] and Fan and Lin <sup>Fan:1998</sup> [29], have noted that the performance of ANOVA suffers for problems when the signal of interest is limited to a window of the observation vector. The reason is that a full dimensional test loses its power due to accumulation of stochastic noise. To see why, suppose  $\mathbf{s}$  is different from  $\mathbf{0}$  only for say the first  $k_0$  samples of the full observation vector. Then on average as  $K > k_0$  goes large,  $\sum_{k=1}^K [\mathbf{s}]_k^2 / \sigma_g^2 \sqrt{2K}$  decreases due to the accumulation of zero mean noise samples and the term within the parenthesis of (4.3) increases, thus reducing  $P_d$ . Therefore, for higher probability of detection, we would like to confine the test on a window mostly containing the signal of the observation vector. The window we choose is a box window  $\mathbf{w}$ , defined as

$$[\mathbf{w}]_k = \begin{cases} 1, & k = k_1, \dots, k_2 \\ 0, & \text{otherwise} \end{cases} \quad (4.4) \quad \boxed{\text{eq:3}}$$

where  $1 \leq k_1 < k_2 \leq K$ . The  $k_1$  and  $k_2$  are chosen in a preset manner, as discussed later in this section.

Multiplying each element in  $\mathbf{y}$  by the corresponding element of  $\mathbf{w}$  gives the windowed  $\mathbf{y}_w$

$$[\mathbf{y}_w]_k = [\mathbf{y}]_k \times [\mathbf{w}]_k, \quad k = 1, \dots, K. \quad (4.5)$$

To demonstrate the utility of HANOVA, we test the time-series shown in Fig. 4.3(a). We choose to test the vector at its full dimension  $k_1$  in (4.4) is 1 and  $k_2 = 1000$ , and two windowed sub-dimensions (each containing fewer and fewer noise components)  $k_1 = 100$  and  $k_2 = 900$ , and  $k_1 = 200$  and  $k_2 = 800$ . From Fig. 4.3(b), it is seen that by setting the window properly, higher probability of detection is gained at different levels of detection thresholds,  $\gamma$  in (4.3). It demonstrates that when signal is not “full-dimensional”, looking for a window of signal-rich sub-dimensions to test will increase the probability of detection.

When the observation is a sequence of high-dimensional vectors whose components are mostly noise, as is the case for our GPR problem, it is desirable to adaptively choose the window to maximize the probability of detection. This kind of method of reducing a full dimensional test to a windowed version is called HANOVA <sup>Fan:1998</sup>[29]. Fan’s original work was limited to problems in which the first  $k_0$  dimensions are believed to be signal-rich and used in HANOVA, with  $k_0$  found from the data. Here we consider a generalization of Fan’s work to take into account the fact that for the GPR problem the transient signal is significant over a window not generally starting with the first dimension but in the middle of the observation vector. Moreover, this window will vary with  $(m, n)$ .

To choose this window we note that (4.3) indicates that the probability of detection achieves its maximum

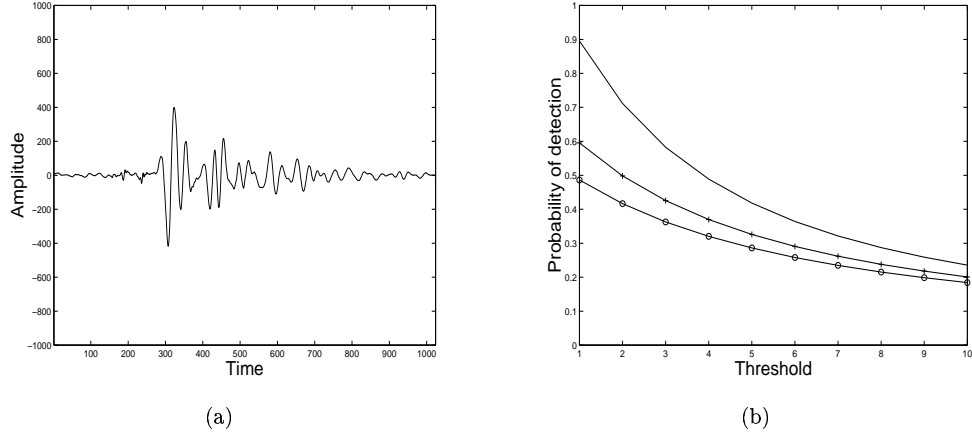


Figure 4.3: Motivating example for use of HANOVA rather than ANOVA. (a) displays sample data collected by a GPR when over an object. The transient nature of the relevant portion of the signal is clear. Unit in time is 0.02 ns. Using this signal, in(b) we display the decreasing detection rates associated with including increasing numbers of “noise” samples in the processing. Probabilities of detection vs. thresholds, solid line, a window from 200 through , ‘+’ line, a window from 100 to 900, ‘o’ line, no window.

fig:why hanova

value when the term inside the parenthesis is minimized. Equally, one wants to maximize the quantity

$$\arg \max_{k_1, k_2} \frac{\sum_{k=k_1}^{k_2} [\mathbf{s}(m, n)]_k^2}{\sigma_g^2 \sqrt{k_2 - k_1 + 1}} - \sqrt{k_2 - k_1 + 1} \quad (4.6)$$

eq:maximi

where  $k_1 < k_2$  and  $k_1, k_2 \in 1, \dots, K$ . The difficulty for us is that in general, the precise structure of  $\mathbf{s}$  is not known. Hence, we use the data to form an estimate of  $\mathbf{s}$  as follows. Assume we are at the  $n$ th stop, then we estimate  $\mathbf{s}$  by the mean value of the previous  $l$  vectors

$$\hat{\mathbf{y}}(m, n) = \begin{cases} \frac{\sum_{j=1}^n \mathbf{y}(m, j)}{j}, & n = 1, \dots, l \\ \frac{\sum_{j=n-l}^n \mathbf{y}(m, j)}{l}, & n > l \end{cases} \quad (4.7)$$

eq>window

where  $m = 1, \dots, M$  and the corresponding window  $\mathbf{w}(m, n)$  is decided based on  $\hat{\mathbf{y}}(m, n)$  as  $k_1, k_2$  are

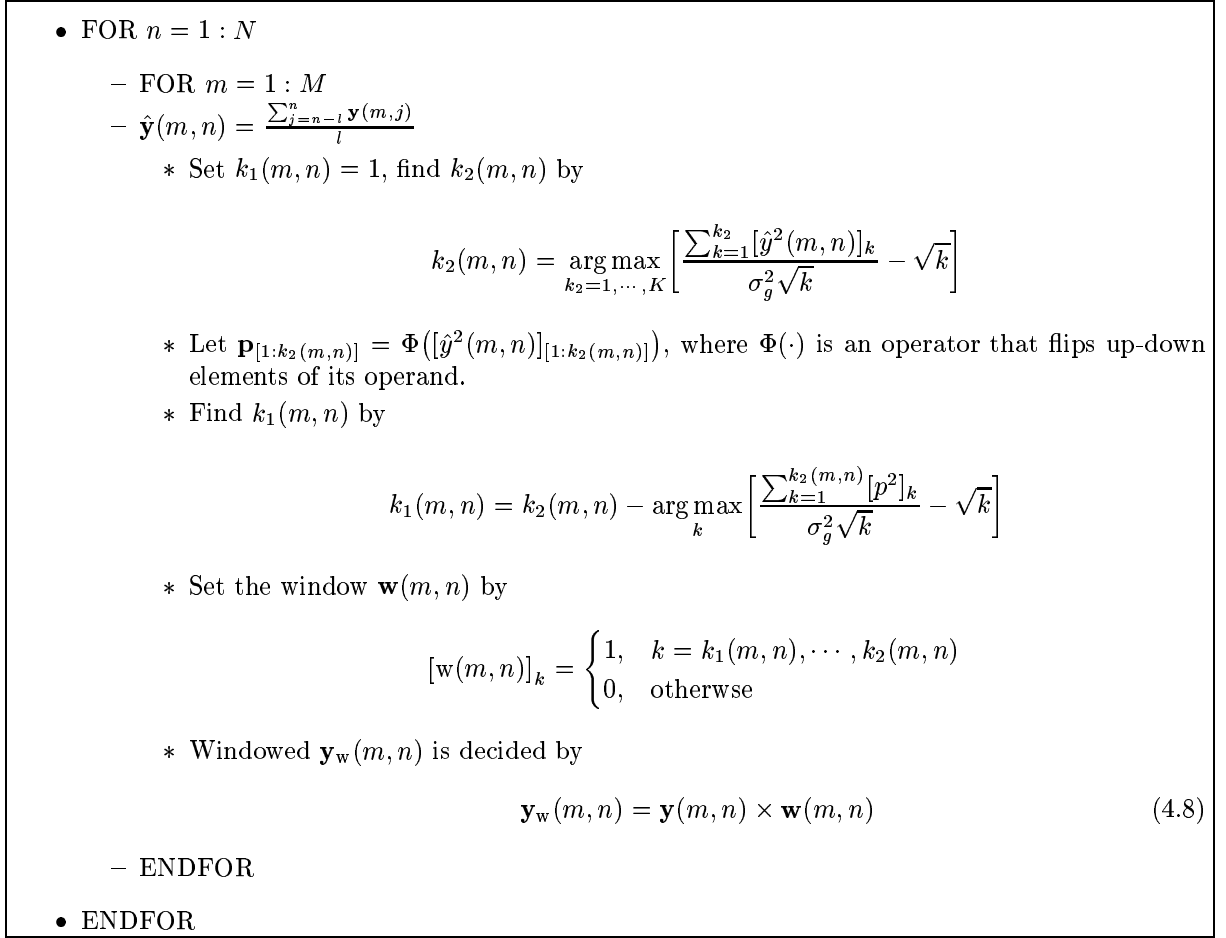


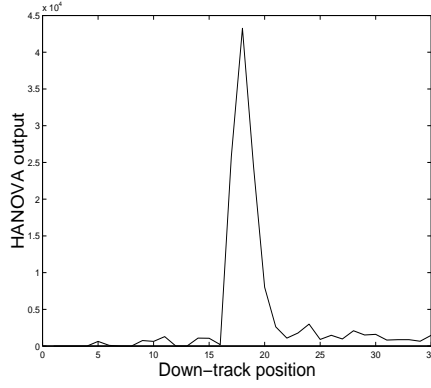
Figure 4.4: Steps of deciding window  $\mathbf{w}(m, n)$  and  $\mathbf{y}_w(m, n)$ .

fig:Search

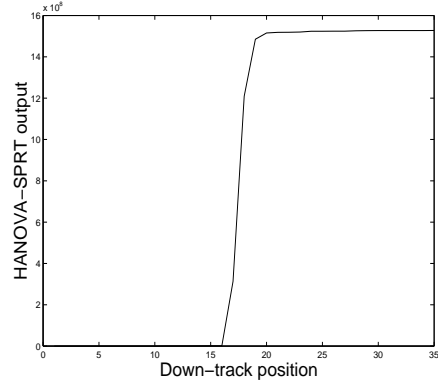
defined by (4.6). More will be said about choosing a proper  $l$  in section 4.3.

Rather than looking for the optimal window by searching over all  $k_1$ - $k_2$  pairs, we pursue a suboptimal, but more efficient two-stage approach. First, we fix  $k_1$  as 1, incrementally increase  $k_2$ , and stop when (4.6) is maximized. Thus we determine the end point of the window  $k_2$ . Starting from  $k_2$ , working backward toward the first point, we similarly determine the starting point of the window,  $k_1$ . Both searching steps can be computed in linear complexity, it takes  $o(K)$  steps to find the  $k_2$  and  $o(k_2)$  steps to find the  $k_1$ <sup>3</sup>. In summary the steps for looking for windows at the  $n$ th stop of the GPR array are given in Fig. 4.4.

<sup>3</sup>The notation  $o(K)$  means that the computational complexity grows slower than or equally fast as  $K$  increases.



(a) HANOVA result  $Y(n)$  over a metal mine.



(b) Output  $U(n)$  of SPRT following HANOVA .

Figure 4.5: HANOVA and SPRT processing results for metal mine data shown in Fig. 4.2. Unit in the horizontal axis is about 7.6 cm.

fig:hanova

Having determined the window at the position  $(m, n)$ , the next stage of processing is to generate a single detection statistic at stop  $n$ . Here we generalize HANOVA to multiple vector observations, via

$$Y(n) = \frac{1}{\sigma_g^2} \sum_{m=1}^M \|\mathbf{y}_w(m, n)\|^2. \quad (4.9)$$

Note  $\mathbf{y}_w(m, n)$  can be of different length because of different window applied. Fig. 4.5(a) shows the result of applying HANOVA to the data in Figure 4.2. Where the HANOVA output is high, so too is the likelihood of an object being present. Thus in Fig. 4.5(a), the object is clearly detectable. More examples involving different types of objects will be given in Section 4.2.

#### 4.1.2 Down-track processing

track processing

While HANOVA detects statistical significance at one stop of the array, it does not capture the object signal structure seen as the array moves down-track. To improve detection performance, we employ a sequential

detection scheme to process  $Y(n)$  recursively as  $n$  increases in order to identify the transient signal arising from the mine <sup>Helstrom:1995, Siegmund:1985</sup> [25, 43]. Specification of this sequential probability ratio test (SPRT) begins by noting that under our models  $Y(n)$  takes on a  $\chi^2$  distribution under both  $H_0$  and  $H_1$ . Standard statistical analysis <sup>Fan:1996</sup> [27] yields

$$\begin{aligned} H_0 : \quad Y(n) &\sim \chi^2_{\sum_{m=1}^M \Delta k(m,n)}(0) \\ H_1 : \quad Y(n) &\sim \chi^2_{\sum_{m=1}^M \Delta k(m,n)}(\delta^2(n)) \end{aligned} \tag{4.10} \quad \text{eq:hanova}$$

for  $n = 1, \dots, N$  where the notation  $x \sim \chi_p^2(\delta^2)$  indicates that the random variable  $x$  is distributed according to a  $\chi^2$  law of order  $p$  and non-centrality parameter  $\delta^2$  <sup>Port:1994</sup> [28] and  $\Delta k(m, n) = k_2(m, n) - k_1(m, n)$  is the length of the  $(n, m)$ th window. For the GPR problem it is easy to show that

$$\delta^2(n) = \frac{1}{\sigma_g^2} \sum_{m=1}^M \|\mathbf{s}(m, n) \times \mathbf{w}(m, n)\|^2. \tag{4.11} \quad \text{eq:delta}$$

For our problem, the length of each window,  $\Delta k(m, n)$ , is large (on the order of hundreds) and the central limit theorem permits us to approximate the  $\chi^2$  distribution using a Gaussian distribution <sup>Port:1994</sup> [28]. We then have

$$\begin{aligned} H_0 : \quad Y(n) &\sim N(\mu_0, \sigma_0^2) \equiv N\left(\sum_{m=1}^M \Delta k(m, n), 2 \sum_{m=1}^M \Delta k(m, n)\right) \\ H_1 : \quad Y(n) &\sim N(\mu_1(n), \sigma_1^2(n)) \equiv N\left(\sum_{m=1}^M \Delta k(m, n) + \delta^2(n), 2 \sum_{m=1}^M \Delta k(m, n) + 4\delta^2(n)\right). \end{aligned} \tag{4.12} \quad \text{eq:normal}$$

At stop  $n$ , the log likelihood ratio for the hypotheses testing problem in (4.12) is

$$u(n) = \ln \frac{p_n(Y(n))}{p_0(Y(n))}, \quad n = 1, \dots, N \quad (4.13) \quad \boxed{\text{eq:likeli}}$$

where  $p_n(Y(n))$  is the PDF of  $Y(n)$  evaluated at the  $n$ th stop under  $H_1$  and  $p_0(Y(n))$  is the PDF of  $Y(n)$  evaluated under  $H_0$ . Under  $H_0$ ,  $\mu_0$  and  $\sigma_0^2$  are estimated using data from an object-free area. Therefore, for this algorithm, the GPR array must start by collecting data in a calibration region to initialize these variables. Under  $H_1$ , one difficulty with generating  $u(n)$  is that  $\mu_1(n)$  and  $\sigma_1^2(n)$  are typically not known *a priori* since the underlying  $\mathbf{s}(m, n)$  are not assumed known. It turns out that we only need to estimate  $\mu_1(n)$ , and  $\sigma_1^2(n)$  can be found from the following relation

$$\begin{aligned} \sigma_1^2(n) &= 2 \sum_{m=1}^M \Delta k(m, n) + 4\delta^2(n) \\ &= 2 \sum_{m=1}^M \Delta k(m, n) + 4 \left[ \mu_1(n) - \sum_{m=1}^M \Delta k(m, n) \right] \\ &= 4\mu_1(n) - 2 \sum_{m=1}^M \Delta k(m, n). \end{aligned} \quad (4.14) \quad \boxed{\text{eq:estima}}$$

At the  $n$ th stop, we estimate the mean of  $Y(n)$  by its maximum likelihood estimator  $\mu_1(n) = Y(n)$ .

The *sequential probability ratio test* statistic  $U(n)$  is a cumulative sum, changing with the acquisition of each new  $u(n)$

$$U(n) = \max(0, U(n-1) + u(n)). \quad (4.15) \quad \boxed{\text{eq:4}}$$

- $U(1) = 0$
- FOR  $n = 2, \dots, N$ 
  - $\mu_1(n) = Y(n)$
  - Form  $\sigma_1^2(n)$  according to (4.14)
  - Form  $u(n)$  according to (4.13)
  - $U(n) = \max(0, U(n-1) + u(n))$
  - IF  $U(n) > \alpha$ , declare object, ENDIF
- ENDFOR

Figure 4.6: Sequential processing.

fig:sequen

Because subsurface object detection is a binary hypothesis testing problem, e.g., we are only interested in knowing whether there is a buried object, the SPRT statistic is bounded from lower bound, zero. When  $U(n-1) + u(n)$  is negative,  $U(n)$  is reset to zero. For a preset threshold  $\alpha$ , the SPRT will make one of two decisions at each  $n$

$$U(n) \geq \alpha \Rightarrow \text{choose } H_1$$

$$U(n) < \alpha \Rightarrow \text{take another observation.}$$

The sequential detection is then essentially a repeated SPRT <sup>Basseville:1993</sup> [44] and summarized in Fig. 4.6.

Fig. 4.5(b) shows the sequential test statistic when the SPRT is applied to the data in Fig. 4.5(a). Because the SPRT in (4.15) has the form of a modified “integrator,” a typical time series for the SPRT statistic takes a step-like form. The larger and sharper the step, the more likely it is that a target is present. At the position where there is an object, the sequential test statistic has a clear upward change again indicating the existence of an object at about position 16.



## 4.2 Examples

In this section we use field data as examples to illustrate the performance of our method. The field data are collected by both single GPR and GPR arrays at different test sites. For each data set, we compare the results from using standard ANOVA, HANOVA, ANOVA followed by SPRT, and HANOVA followed by SPRT. Comparison indicates that generally HANOVA performs better than ANOVA, and with SPRT, both ANOVA and HANOVA make fewer false-alarms. In other words, HANOVA with SPRT gives the best receiver-operating characteristics, as we shall see later in this section.

At first, we apply our method on data collected by single GPR at different test sites. Some data are taken under relatively favorable condition, while most are from more hostile test sites which involve rough ground surface and other clutter. Fig. 4.7 compares results of ANOVA and HANOVA on a buried steel object at position 50. For comparison, the outputs of ANOVA and HANOVA are normalized to one. It is observable that while both methods detect the object easily, the HANOVA is better in suppressing noise output where there is no object, e.g., at position 1 through 40 and 60 through 100, Fig. 4.7(c) and (d). Fig. 4.8(a) and (b) show the results from detecting a plastic mine, M19, at position 50. Again, the HANOVA performs better in suppressing noise. At positions 20 through 40, the HANOVA creates a much lower noise level than the ANOVA does. Similarly, the HANOVA produces a cleaner output at the end of the run.

Fig. 4.8(c) and (d) show the results of ANOVA and HANOVA in detecting an anti-tank mine, TM62, from a very “noisy” data set. The mine is buried at position 60. Outputs of both HANOVA and ANOVA consist of the correct detection and some false alarms. The HANOVA maintains a better performance than the ANOVA in the sense that, for a given detection threshold, the HANOVA would generally have a smaller

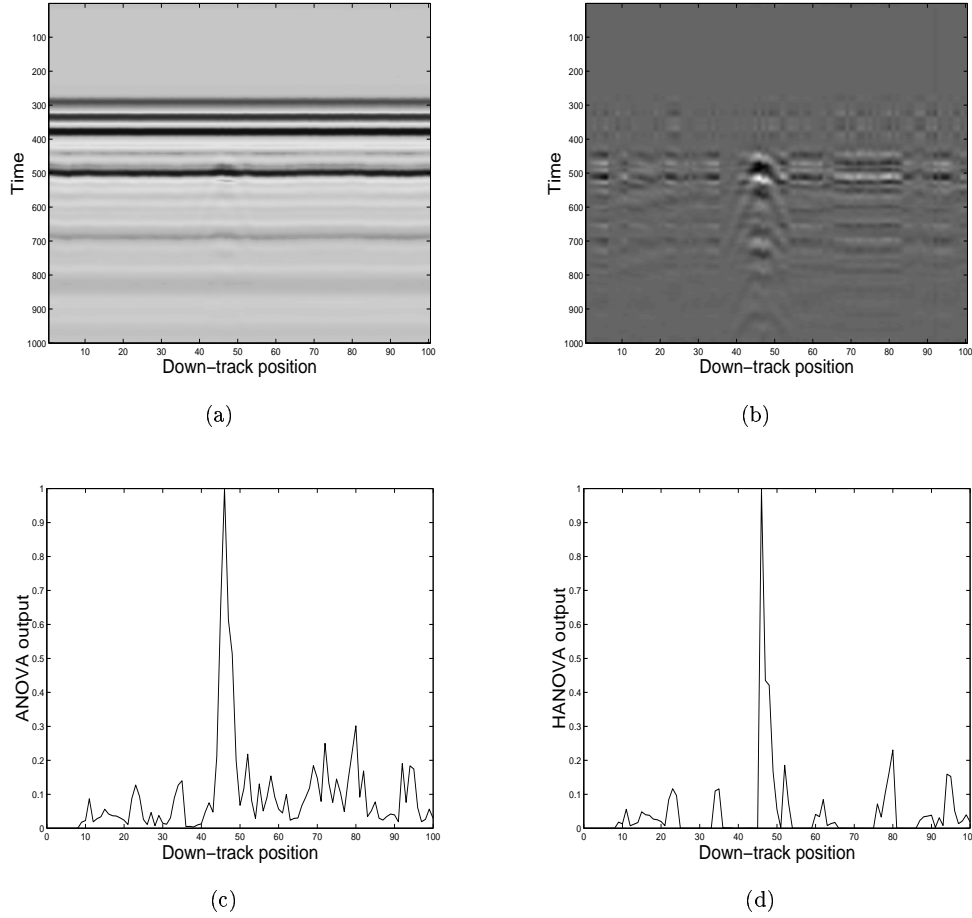


Figure 4.7: Results of a single GPR measurement above a steel object around position 50, a) raw observation, b) observation after background removal, c) ANOVA output, d) HANOVA output. In a) and b), unit in the horizontal axis is about 7.6 cm and unit in the time axis is 0.02 ns.

fig:steel

number of false-alarms. For the HANOVA, no false alarms will be declared for a threshold greater than 0.5, while for the ANOVA, the threshold must be set above 0.8 to avoid making a wrong decision. Between threshold 0.5 and 0.8, the ANOVA will make two false-alarms while the HANOVA has zero false-alarm.

Next, by comparing the outputs of the SPRT in the above three examples, we see that sequential processing generally smoothes the output and generates fewer false-alarms than by using ANOVA (or HANOVA) only, Fig. 4.9. In all three examples, SPRT following HANOVA performs better than SPRT following ANOVA, in the sense that the output is more leveled off at object-free area and the jump at the position of

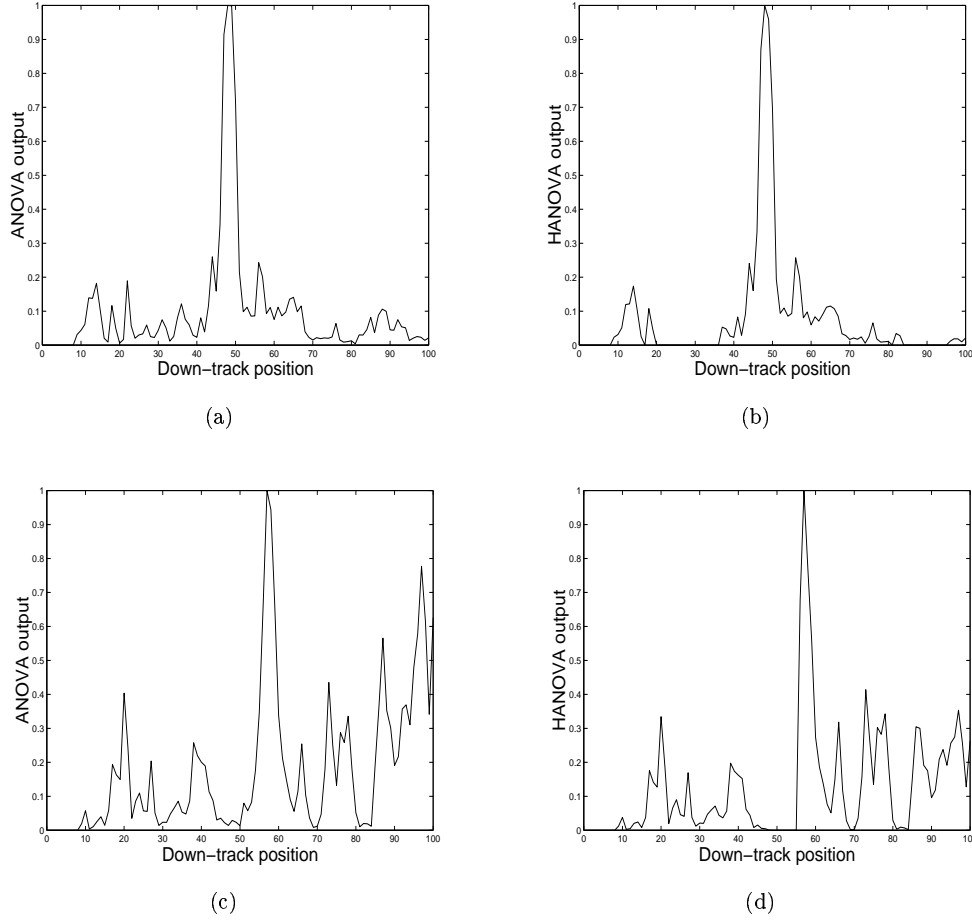


Figure 4.8: More comparison between the ANOVA and HANOVA, a) ANOVA over an M19, anti-tank mine, buried at position 50, b) HANOVA over the M19, c) ANOVA over a TM62, anti-tank mine, buried to the side of the track at position 58, d) HANOVA over the TM62. Unit in the horizontal axis is about 7.6 cm.

the buried object is sharper.

To study the receiver operating characteristic (ROC) of the method, we test our method on multiple runs of different type of targets. Fig. 4.10(a) shows the ROC curves of ANOVA and HANOVA to detect 60 metallic objects. The objects include metallic mines such as TM15, TM46, and PMN. Fig. 4.10(b) shows the ROC of ANOVA-SPRT and HANOVA-SPRT. Compared with Fig. 4.10(a), SPRT improves the performance of both ANOVA and HANOVA. In generating these curves a correct identification of any of the objects was

taken to be a “detection” whether or not the object itself was a mine. Indeed, as noted in the Introduction, the algorithm in this paper is intended *only* to detect the presence of objects below the array and not to solve the classification problem. Still, given the “real-world” conditions under which the data were taken, the low false alarm rates here point to the robustness of our approach.

Next, we compare the performance of ANOVA, HANOVA, ANOVA-SPRT, and HANOVA-SPRT in detecting 70 plastic mines. The mines are M19, VS-1.6, T72, and C4A1. Fig. 4.11 shows the ROC curves of the above four methods. It is seen that both the ANOVA-SPRT and HANOVA-SPRT perform better than the ANOVA and HANOVA, respectively.

As another example, we test our method on a different array radar system at another test site. The setup of the GPR array is shown in Fig. 4.12. There is one transmitter in this system. In front of the transmitter, four receivers are positioned in a  $2 \times 2$  pattern. Above the transmitter and the receivers there is a hyperbolic reflection plate, it is set so that the transmitter is at the focal point of the reflection plate. The array moves on a linear track to collect data. At each step, the transmitter sends a spherical wave to the reflection plate and after reflection, the sphere wave becomes plane wave. The four receivers then collect reflection of this plane wave from the ground. The system has the advantage of generating plane wave and points it forward to reduce ground reflection. Fig. 4.13 displays collected data from the two front receivers at the Dedham test site of Northeastern University and the corresponding signal after background removal. In an area of  $58 \text{ m}^2$ , there are 12 buried landmines of different types, such as M19, PMN, VS-2.2, and so on. Using our method we are able to detect all 12 mines with a few false-alarms, Fig. 4.14. The results are similar to those obtained by a single GPR. For a detection rate above 90%, the HANOVA has a significantly smaller number of false-alarm.

### 4.3 Window Selection in HANOVA

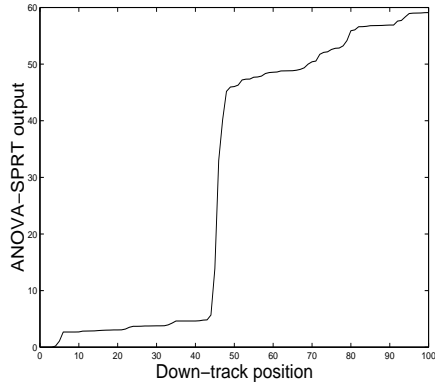
Ideally, we want to find a window that is sensitive to the presence of a signal and provides little response in the test statistic when there is noise only. But these two requirements are often in conflict with each other. From (4.7), we can change the order  $l$  of the MA process to control the window we use. The smaller is  $l$ , the more sensitive the window is to the presence of signal and strong noise. On the other hand, the larger is  $l$ , the more robust will the statistic be to noise, which translates into a smaller probability of false-alarm. But a large  $l$  reduces sensitivity of the HANOVA to signal. Fig. 4.15 shows the effect of  $l$  on window selection and the corresponding HANOVA results. Three different  $l$  are used, i.e.,  $l = 1, 4, 9$ . In the data, there are three mine objects, two metal mines at the position 110 and 170. A weak mine object is at position 25. For comparison, we normalize the HANOVA outputs in each case by its maximum value, which corresponds to the strong metal mine buried at position 110. Fig. 4.15(a) and (b) show the window chosen by a MA of order 1 and the resulting HANOVA output. The two strong objects can be detected at a threshold of 0.7, the weak object can only be found at a threshold of 0.2. Fig. 4.15(c) shows the window chosen by a MA of order 4. The window oscillates much less than the window in Fig. 4.15(a). From the HANOVA result, Fig. 4.15(d), we can find all the three objects at a threshold of 0.3. Increasing the order of MA process can make the results worse, Fig. 4.15(e) and (f). A large window reduces the sensitivity of the HANOVA to signal and actually makes detection more difficult. Now the weak object at position 25 cannot be detected at a threshold greater than 0.3. As a guideline, we find that MA processes of order between 3 and 10 yield good windows both in sensitivity to signal and robustness to noise. This selection is affected by the step-size of the array. An array moving at small step-size will allow an MA process of large  $l$  in selecting windows,

and vice versa.

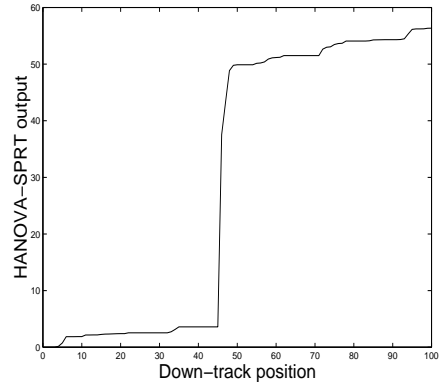
## 4.4 Concluding Remarks

cluding remarks

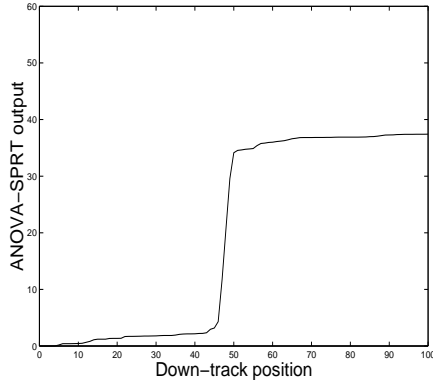
In this chapter, we have proposed a sequential, high-dimensional ANOVA to process GPR returns. The method is tested on real data and has a relaxed requirement on the physical model used in the processing routine. The method is on-line implementable and has a linear computational load. The method works in two stages: first it looks for statistically significant difference from array observations, second, it applies a sequential detection as new data are obtained. HANOVA is powerful in the sense of maximizing probability of detecting statistically significant difference among sub-dimensions of a full vector of observations. Sequential detection recursively processes the result of the HANOVA and enables real-time processing as new data are collected. We have demonstrated the performance of this technique on samples of field data.



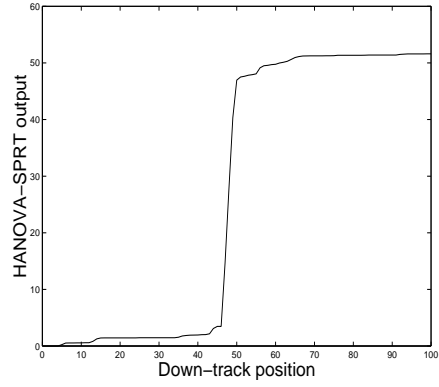
(a)



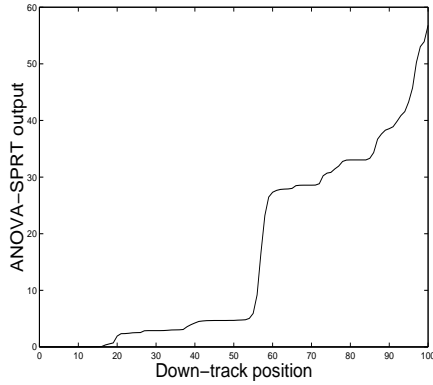
(b)



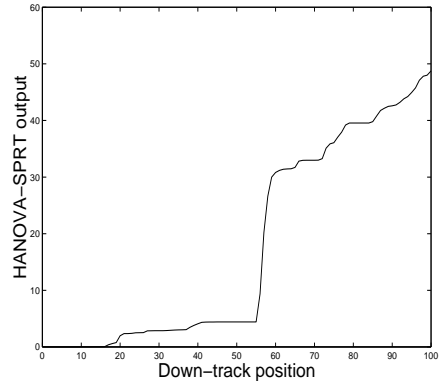
(c)



(d)



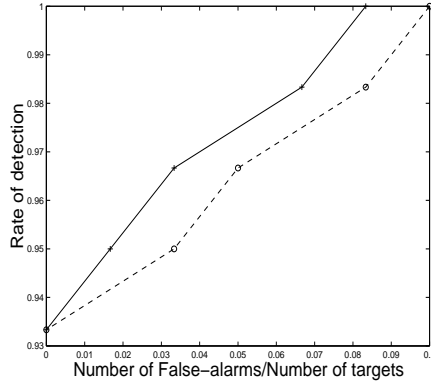
(e)



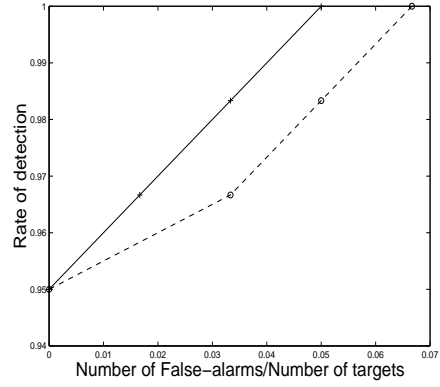
(f)

Figure 4.9: Results of the SPRT, a buried steel object, a) output of ANOVA-SPRT, b) output of HANOVA-SPRT; a buried M19, c) output of ANOVA-SPRT, d) output of HANOVA-SPRT; a buried TM62, e) output of ANOVA-SPRT, f) output of HANOVA-SPRT. Unit in the horizontal axis is about 7.6 cm.

Fig:Socorro SPRT

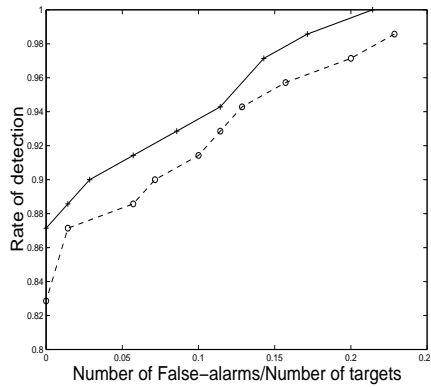


(a)

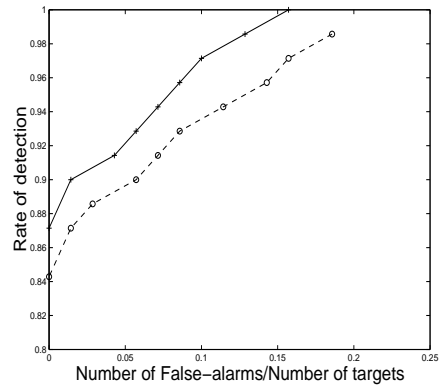


(b)

Figure 4.10: Rate of detection and rate of false-alarms in detecting metallic objects, solid line is the result of HANOVA, dashed line is the result of ANOVA, a) ANOVA vs. HANOVA, b) ANOVA-SPRT vs. HANOVA-SPRT.



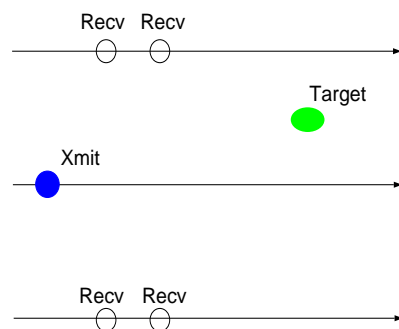
(a)



(b)

Figure 4.11: Rate of detection and rate of false-alarms in detecting plastic mines, solid line is the result of HANOVA, dashed line is the result of ANOVA, a) ANOVA vs. HANOVA, b) ANOVA-SPRT vs. HANOVA-SPRT.





(a)

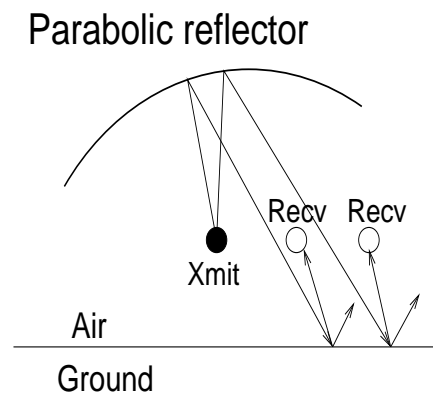


Figure 4.12: GPR array used at Dedham test site of Northeastern University, a) plane view, b) side view.

fig:gpr Dedham

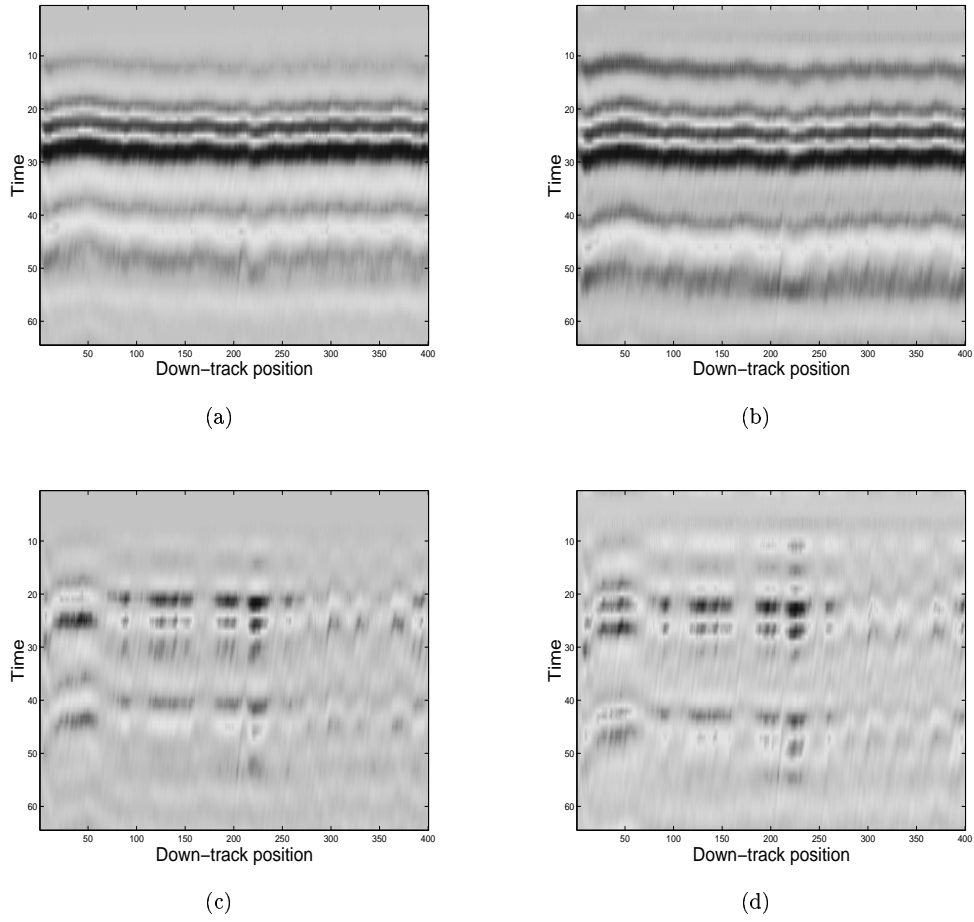


Figure 4.13: GPR data from the Dedham test site, (a) from the left front receiver, (b) from the right front receiver, (c) signal (a) after background removal, (d) signal of (b) after background removal. Unit in time axis is 120 ps.

edham test data

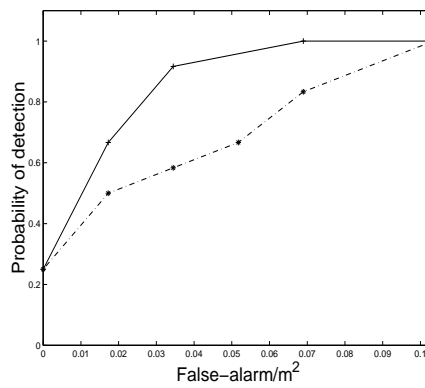
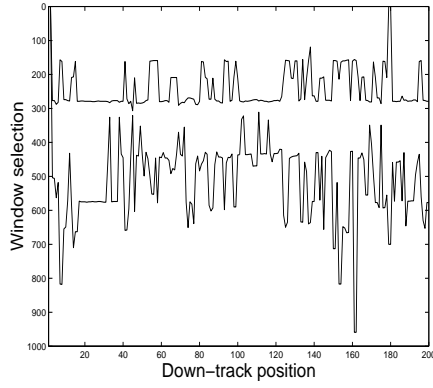
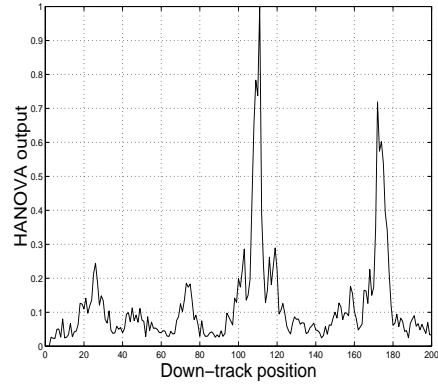


Figure 4.14: ROCs of the Dedham test, solid line, HANOVA-SPRT, dash line, ANOVA-SPRT.

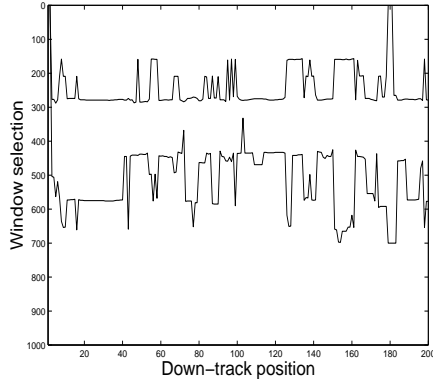
fig:roc D



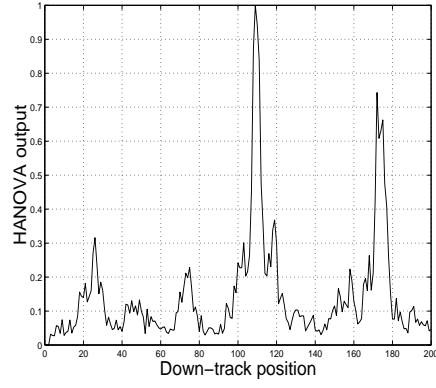
(a)



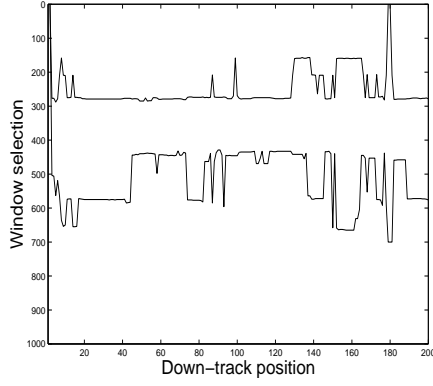
(b)



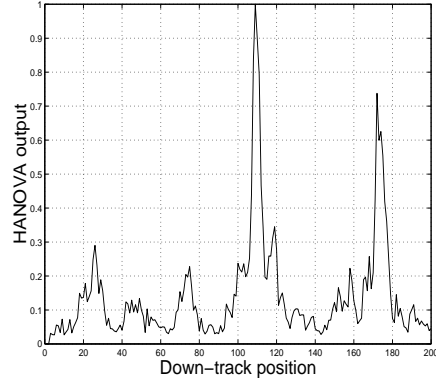
(c)



(d)



(e)



(f)

Figure 4.15: Choices of window and effect on HANOVA, lower line is  $k_1(m, n)$ , upper line is  $k_2(m, n)$ , a) window selected by an order 1 MA process, b) HANOVA result from the window to the left, c) window selected by an order 4 MA process, d) HANOVA result from the window to the left, e) window selected by an order 10 MA process, f) HANOVA test result from the window to the left.

different windows

## Chapter 5

# Iterative Histogram Equalization To Enhance GPR Image

am equalization

In this chapter we investigate using histogram equalization to enhance GPR images. As mentioned in the previous chapters, GPR inevitably registers the specular reflection from the ground which interferes GPR signal processing very much. Compared with the specular reflection, landmine reflect signals are of small amplitude and hard to observe. Histogram equalization is very useful in enhancing weak signals <sup>Jain:1989</sup> [45]. Using iterative histogram equalization and background removal method, we can obtain better GPR images to improve landmine detection. The background removal method used are median filter and subtraction of the ensemble mean. The image enhancement method presented in this chapter is very effective in improving GPR images when the landmines are buried close to the surface. In this case, time-gating as a method of separating the specular reflection from the landmine reflected signals is not difficult to carry out because

of the proximity of the two signals. The iterative histogram equalization (IHE) does not require searching the boundary between the specular reflection and the landmine reflected signals. Instead, by enhancing the landmine reflected signals, background removal becomes easier and more effective. At the end, landmine reflected signals is more observable and detectable.

## 5.1 Introduction

m introduction

The histogram of a signal represents the relative frequency of occurrence of the various amplitude levels in the signal. Obviously the signal can be of one-dimensional or multi-dimensional. In GPR image enhancement, histogram-modeling techniques modify a GPR image so that its histogram has a desired shape. For example, in most cases, we would like to enhance the low-contrast part of the image which contains the landmine reflect signals. As we will see, a GPR image of enhanced low-contrast part has a histogram stretched out. Histogram-modeling techniques fall into three categories, histogram equalization, histogram modification, and histogram specification, respectively. We use the histogram equalization to obtain better GPR images.

At this point, some observation about landmine detection are helpful to understand the challenges of the problem. To the contrary of intuition, it is usually the shallowly buried landmines that is difficult to detect because they are close to the surface and their signals are mixed with the specular reflection from the ground. For the deep buried landmines, time-gating is often sufficient to separate the landmine reflected signal from the ground bounce, i.e., by throwing away signals arrived in the first few nanoseconds one will have only the landmine reflected signal left and detection is not very difficult. Returning to the detection of shallowly buried landmines, we will see that simple background subtraction does not always produce satisfactory

results. On the other hand, using histogram equalization, we can enhance the landmine reflected signal and then background subtraction will be more constructive. What's more, better result can be obtained by iteratively applying the histogram equalization and background removal. In the next section, we introduce an iterative histogram equalization method to enhance GPR images. The field data used in this chapter are collected by BRTRC, Inc. at Fort AP Hill test site in Virginia, USA.

## 5.2 Iterative Histogram Enhancement

sec:method

In landmine detection using GPR, the desired signal is the reflected wave from buried landmines. To enhance the landmine reflected signals, we use histogram equalization to increase the contrast of the GPR image. After the histogram equalization, background removal is carried out by subtracting the ensemble average of the equalized image and a median filter is applied to remove any speckle point in the image. The whole process is iterated to give better result before it diverges. The flowchart of iterative histogram equalization is shown in Fig. 5.1. The median filter is taken over a window of  $3 \times 3$ . For a received GPR image  $\mathbf{y}(m, n)$  of size  $M \times N$ , the mean subtraction is carried out as

$$\mathbf{z}(:, n) = \mathbf{y}(:, n) - \bar{\mathbf{y}}, \quad n = 1, \dots, N \quad (5.1) \quad \text{eq:5.1}$$

where  $\bar{\mathbf{y}} = \frac{1}{N} \sum_{n=1}^N \mathbf{y}(:, n)$  is the ensemble average of  $\mathbf{y}$  along the column direction. The median filter is defined as

$$\mathbf{z}(m, n) = \text{median}\{\mathbf{y}(m - k, n - l), (k, l) \in W\} \quad (5.2) \quad \text{eq:5.2}$$

where  $W$  is a pre-chosen filter window, usually of size  $3 \times 3$ ,  $5 \times 5$ , or  $7 \times 7$ . The median filter is able to remove a single very unrepresentative pixel in the filter window. The algorithm for median filtering requires arranging the pixel values in the filter window in ascending or descending order and picking the middle value. If the number of pixels in the filter is an even-number  $2k$ , the median value is calculated as the average of the arranged pixels at position  $k$  and  $k + 1$ . Because the average of two numbers is usually different from either of the two numbers, median filter is almost always taken over a filter window consisting of an odd-number of pixels such that the median is an actual pixel value in the filter window. For this reason the median filter is better at preserving sharp discontinuities. Because in increasing image contrast, the histogram stretch does not discriminate the desired details from the landmine reflected signals and other small undesirable disturbance, interference will appear as the iteration goes on. The interference appears in the form of speckle noise and can be very well removed by the median filter. In the next two sections, we use examples to compare the performance of IHE with and without median filtering.

## 5.3 Examples

### 5.3.1 2-D examples

sec:2-D examples

In this section we use some examples from field data to show the performance of the IHE. Fig. 5.2 (a) displays a GPR image from a buried EM12 landmine at depth of 2.54 cm (1 inch). Output of subtracting the ensemble average is shown in Fig. 5.2 (b). Fig. 5.2 (c) and (d) plot the columnwise  $L_2$  norm of Fig. 5.2 (a) and (b). It is seen that there is not too much improvement. Results of histogram equalization are shown in Fig. 5.3 where the images generated with and without median filtering are compared. It is seen that in

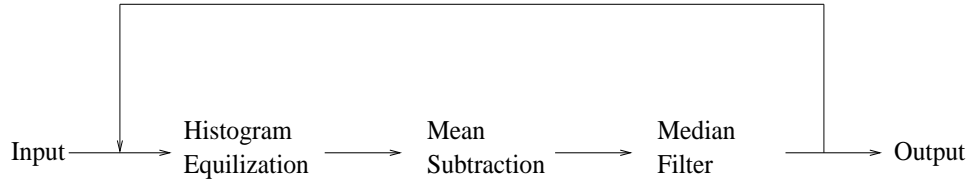


Figure 5.1: Flowchart of iterative histogram equalization.

fig:flowcl

both cases the landmine is readily observable after 6 iterations but the images generated without median filtering have speckle noise. The stripes to the left and right side of the landmine signal are due to the background removal method, which is a subtraction of the ensemble average. Fig. 5.5 plots the histogram of the results of the IHE at iteration  $1, 2, \dots, 6$ . From the figure, we see that the largest component of the histogram increases as the iteration goes on, this corresponds to a more homogeneous background since the largest component corresponds to the background. This change is desirable because it means an increased contrast of the image.

Fig. 5.6 shows results of applying the IHE over a buried M21 landmine. The change in histogram is displayed in Fig. 5.7. From both figures, it is seen that as iteration increases, the IHE produces better images. Another example is shown in Fig. 5.8. In the figure, a VS16 landmine is buried at 2.54 cm. The landmine is easily observable in Fig. 5.8 (d). The bright spot at the upper left corner can be eliminated because in most cases we know the height of the GPR and signals arrived much earlier than the ground bounce can be safely ignored.

### 5.3.2 3-D examples

The IHE can be expanded to three dimensions in a straight-forward manner. Again we use data collected at Fort AP Hill test site to demonstrate the performance of the IHE. The data was collected by a single



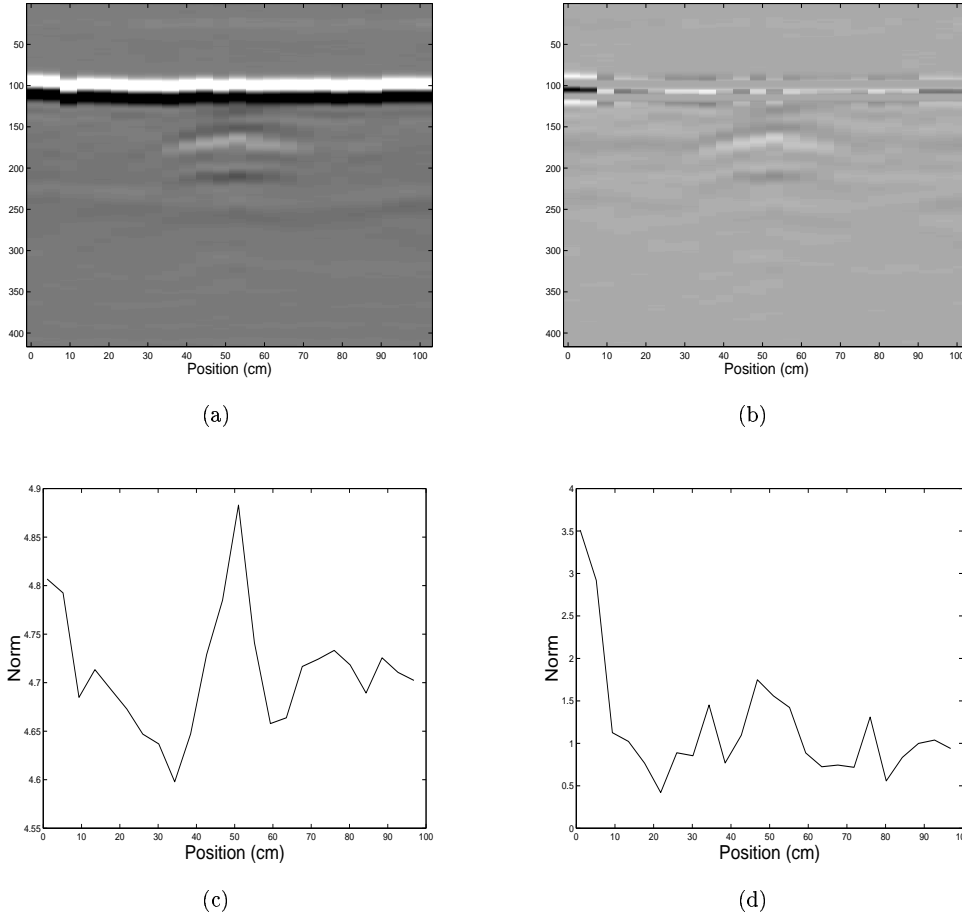


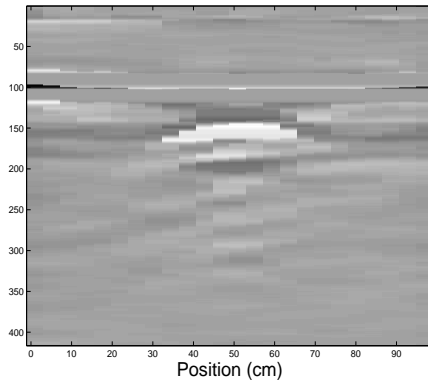
Figure 5.2: (a) Original GPR image over an EM12 landmine, (b) image after subtracting the ensemble average, (c) columnwise norm of (a), (d) columnwise norm of (b).

fig:1a

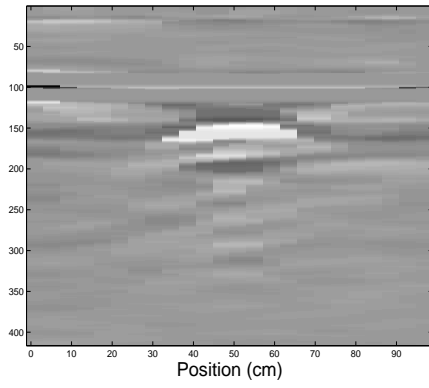
GPR running down a linear track, starting from different cross-track position. The whole data set is of size  $416 \times 21 \times 8$  or  $416 \times 24 \times 8$ , which means that at each stop the GPR takes 416 samples in time and makes 21 or 24 stops along the track, covering roughly one meter to 1.2 meters. In both cases, the GPR starts again in one of eight different cross-track positions. Two examples are given in Fig. 5.9 and 5.10, over an M15 and a VS-22 landmine. While in both cases there are speckle noises in some frames, it is seen that by combining the eight images we can easily detect the landmines.

## 5.4 Concluding Remarks

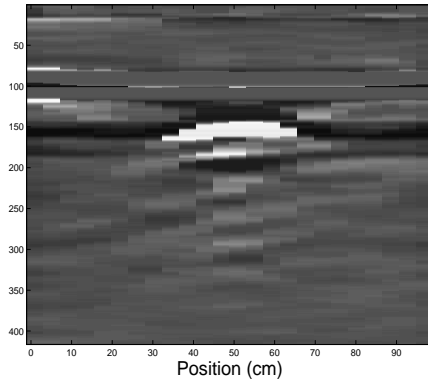
In this chapter, we present an image enhancement method based on histogram equalization. The IHE increases the contrast of a landmine reflected signal by altering the histogram of the original GPR image. Followed by background subtraction and median filtering, the IHE is able to eliminate most of the ground bounce and keep landmine reflected signals intact. The speckle noise incurred in the iteration is removed by the median filter. The iterative method presented in this chapter aims to enhance GPR images when the landmine reflected signals are weak in amplitude and do not display a manifest hyperbolic curve usually seen in the GPR images. The method is based on image processing technique and statistical signal processing. In the next chapter, we propose an optimized migration method based on the wave equation.



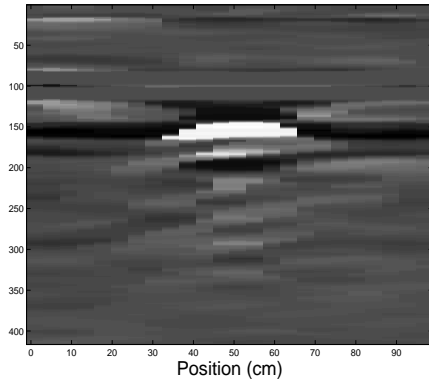
(a)



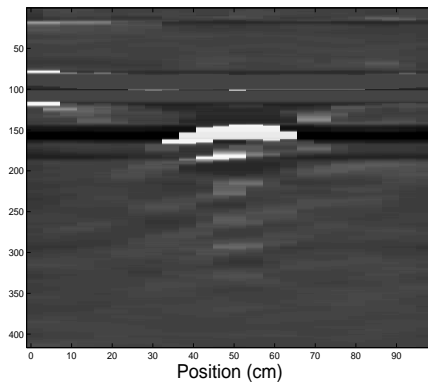
(b)



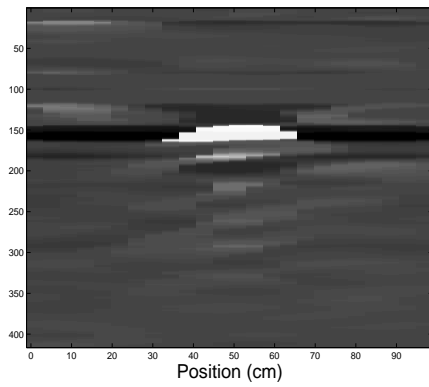
(c)



(d)



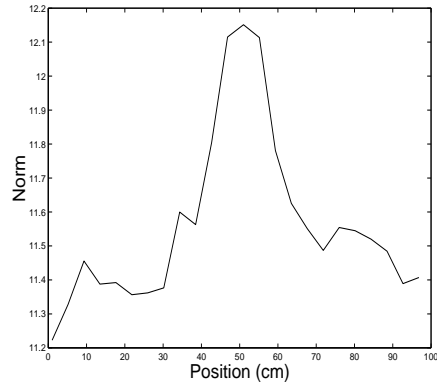
(e)



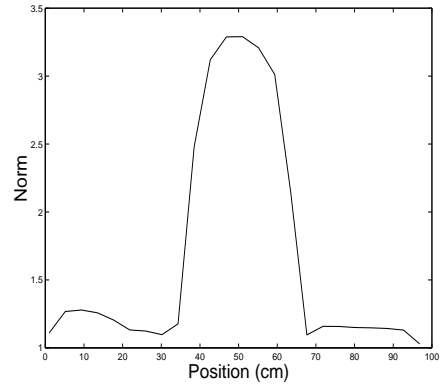
(f)

Figure 5.3: Left column, images of the IHE with median filtering at iteration 1, 3, and 6. Right column, images of the IHE with median filtering at iteration 1, 3, and 6.

fig:1



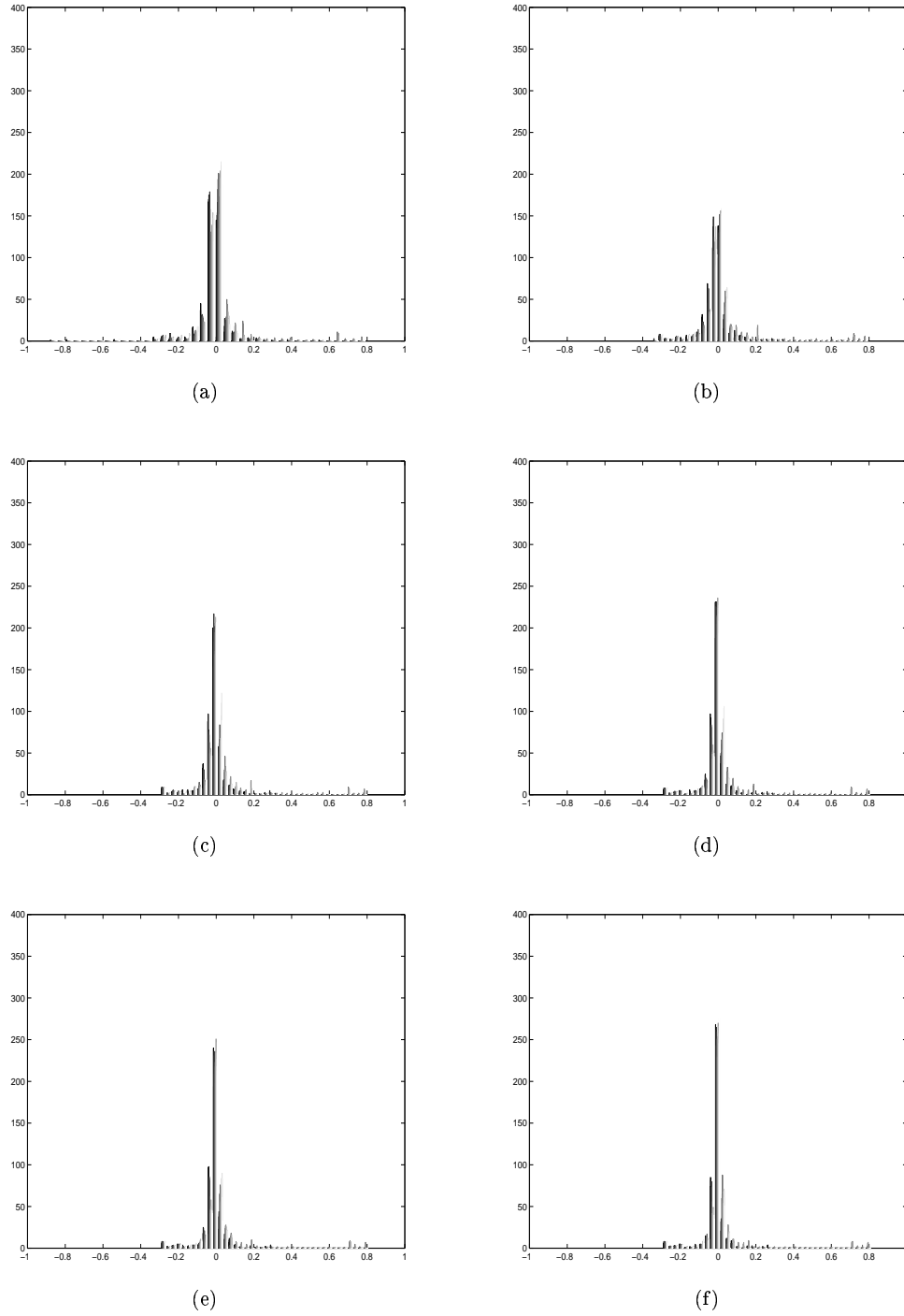
(a)



(b)

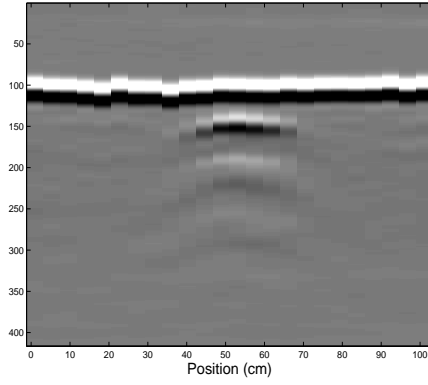
Figure 5.4: (a) Norm of the IHE result without median filtering at iteration 6, (b) norm of the IHE result with median filtering at iteration 6.

fig:1c

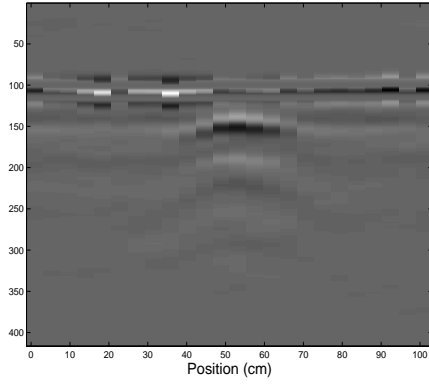


**fig:1b**

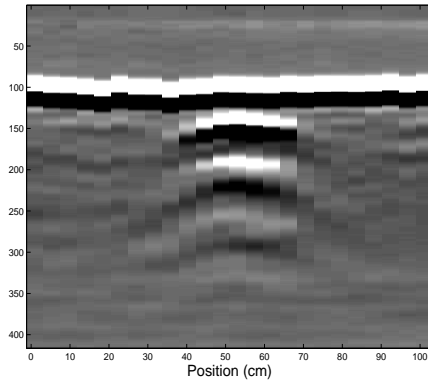
Figure 5.5: Histogram of the IHE result with median filter at iteration 1 to 6, from (a) to (f).



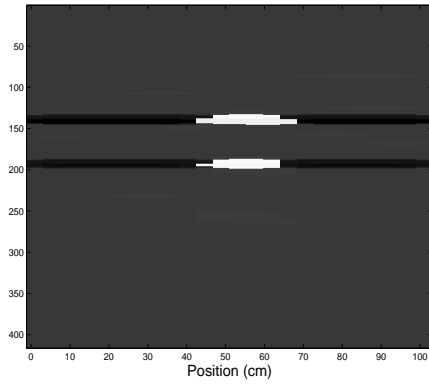
(a)



(b)



(c)



(d)

Figure 5.6: (a) Original GPR image over an M21 landmine, (b) image after subtracting the ensemble average, (c) image of histogram equalization, (d) image of the IHE result at iteration 6.

fig:2

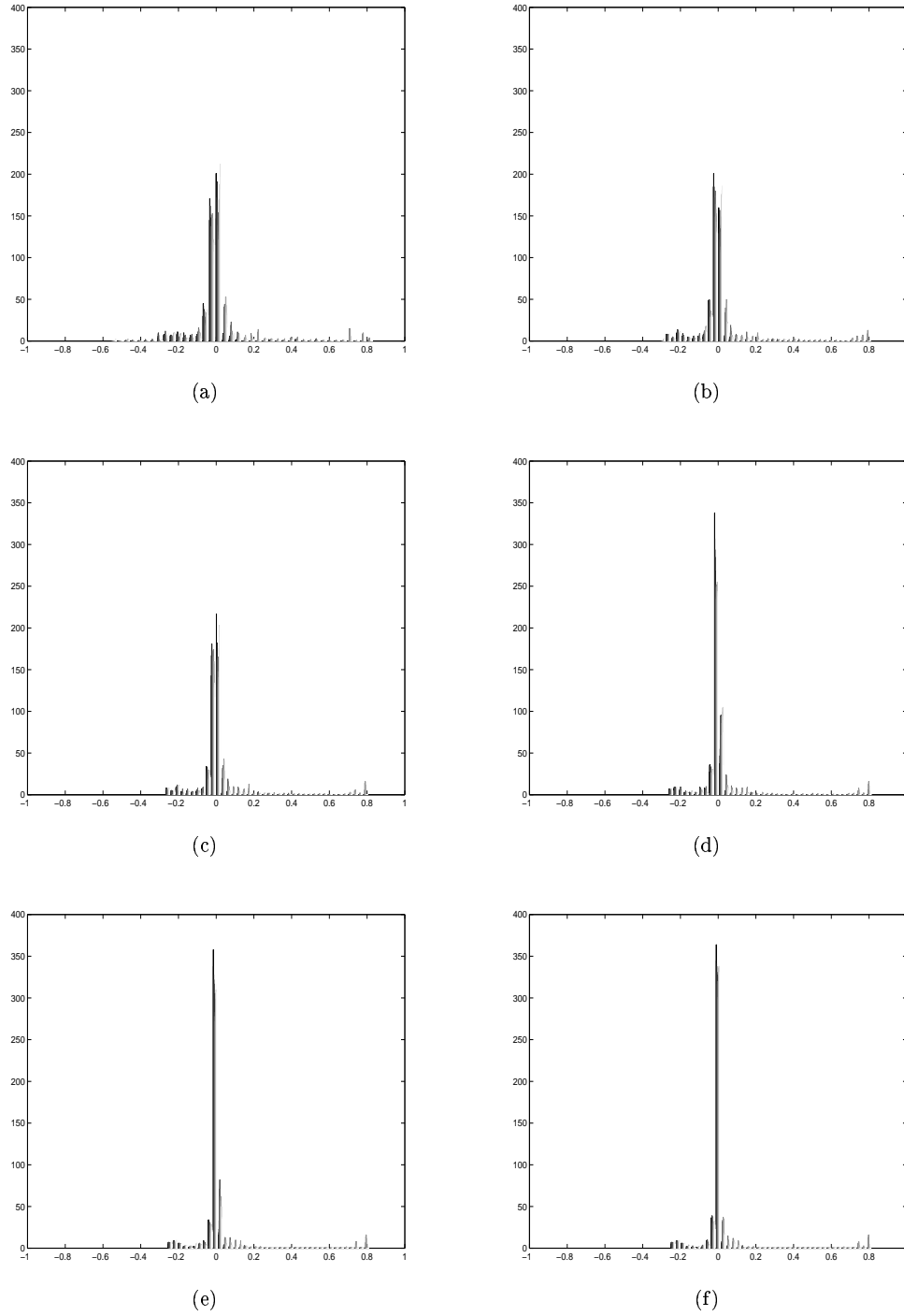
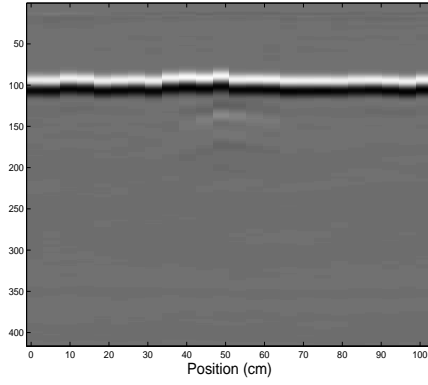
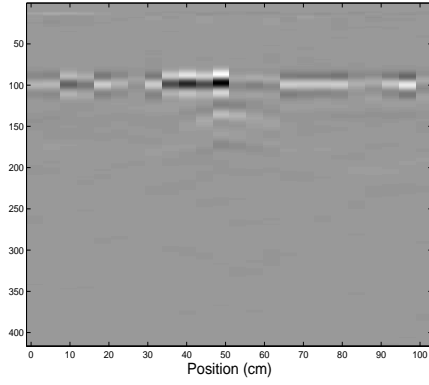


fig:2b

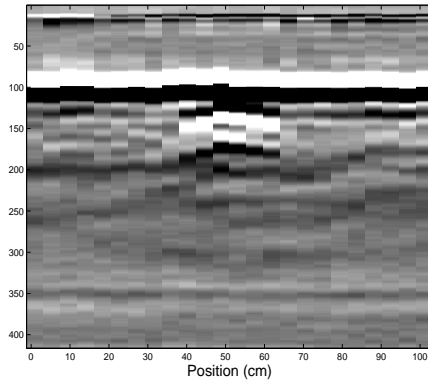
Figure 5.7: (a) to (f), histograms of the IHE results at iteration 1 to 6.



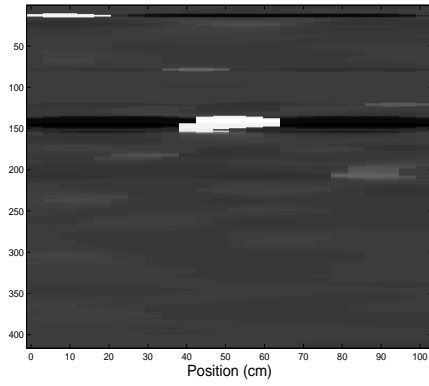
(a)



(b)



(c)

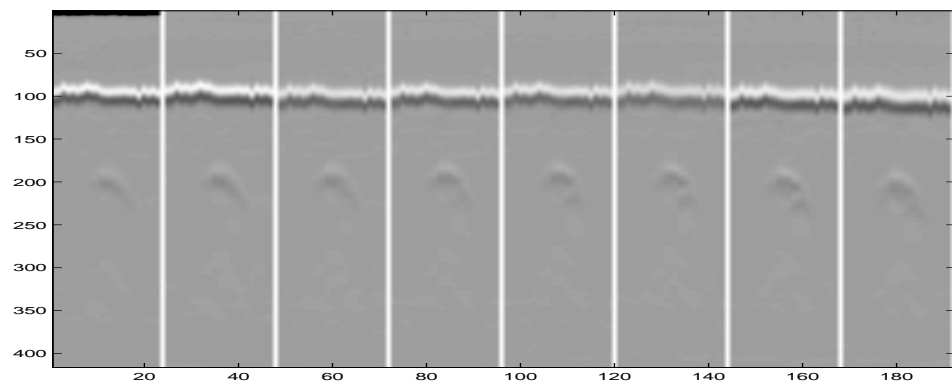


(d)

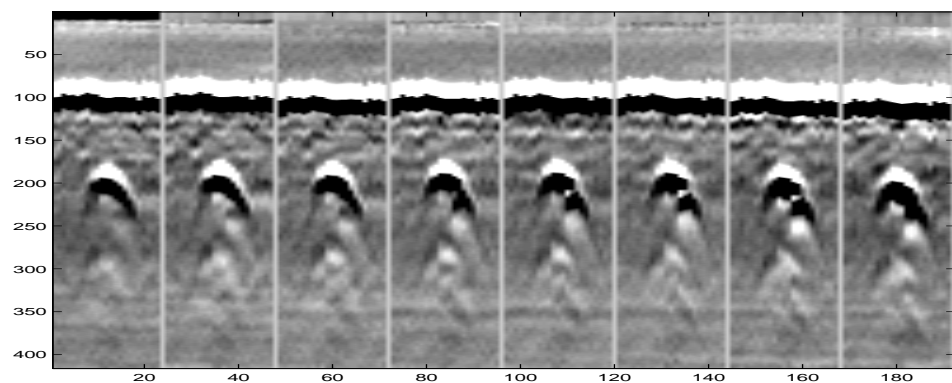
Figure 5.8: (a) Original GPR image over a VS16 landmine, (b) image after subtracting the ensemble average, (c) image of histogram equalization, (d) image of the IHE at iteration 6.

fig:3

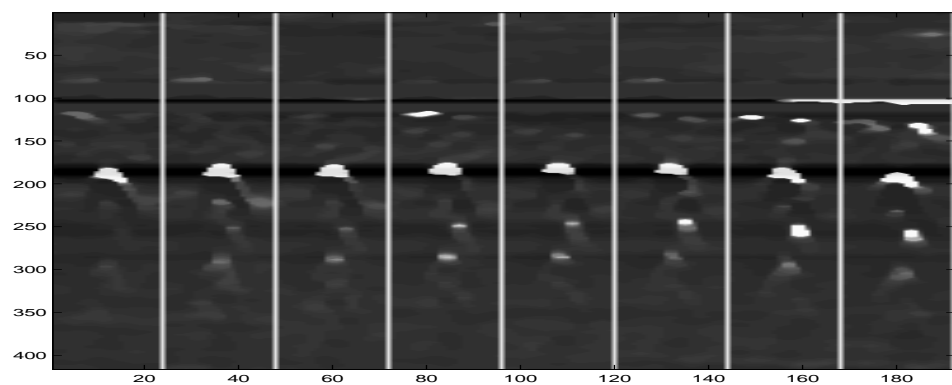




(a)



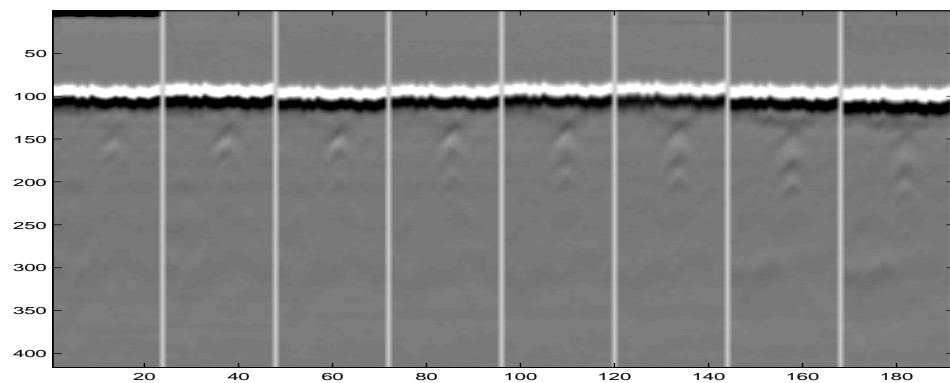
(b)



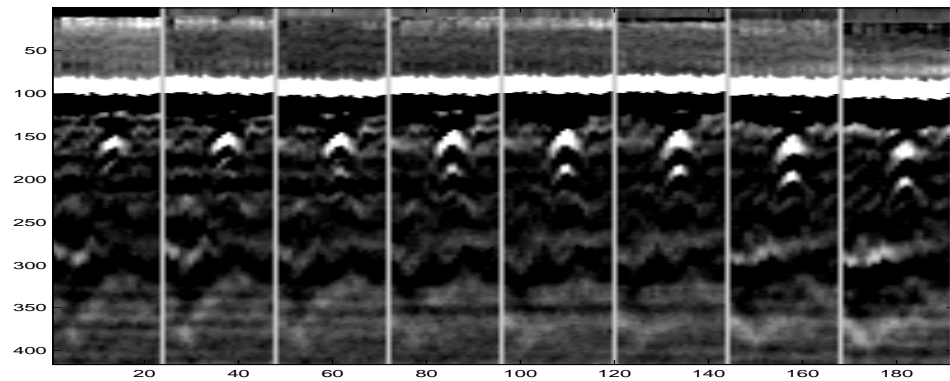
(c)

Figure 5.9: (a) Cascaded GPR images over an M15 landmine, (b) cascaded images of the IHE at iteration 1, (c) cascaded images of the IHE at iteration 6.

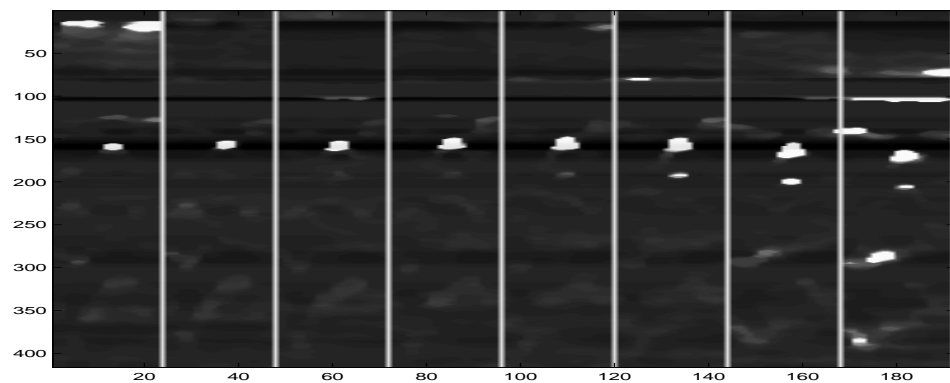
fig:4



(a)



(b)



(c)

Figure 5.10: (a) Cascaded GPR images over a VS-22 landmine, (b) cascaded images of the IHE at iteration 1, (c) cascaded images of the IHE at iteration 6.

fig:5

## Chapter 6

# Optimized F-K Migration to Locate Landmines

ch:localization

To localize a buried landmine, F-K migration can be used to reconstruct underground reflectivity of the medium. For the purpose of discussion, we describe the F-K migration in two dimensions. F-K migration can be generalized to three dimensions in a straight-forward manner. Denote the 2-D wavefield registered by a GPR array by  $p_i(x, z = 0, t)$  where  $x$  is the horizontal direction,  $z$  is the vertical direction pointing from the surface downward to the soil, and  $t$  is time, then the task of F-K migration is reconstructing subsurface reflectivity  $p_o(x, z, t = 0)$  from the received wavefield at the surface <sup>Robinson:1983</sup>[16].

F-K migration has been proven to be a very effective geophysical inversion method in seismic data processing. But there are additional considerations when using F-K migration on GPR data to localize landmines. First, the ground surface is not flat. Rough ground surface introduces random time-delays and

if not treated properly, this random time-delay affects performance of the F-K migration. Second, there are noise and clutter in GPR signal and F-K migration may generate sidelobes. In landmine localization, regular F-K migration uses constant wave propagation velocity for all the T/R pairs and performs well when GPR signal is clean. In the presence of rough ground surface, noise, and clutter, its performance deteriorates. Using different velocities at different GPR positions is able to improve F-K migration output. The varying velocities are determined by Tikhonov regularization.

## 6.1 Algorithm

ation algorithm

### 6.1.1 F-K migration

Here, we assume that most of measurement noise and ground reflection have been eliminated by some preprocessing methods, such as moving average filtering <sup>Kp:2000c</sup>[46]. The most important assumption of F-K migration is the exploding reflector hypothesis. At time zero, the exploding reflector activates and emits a spherical wave in all directions and the exploding reflector disappears. The array of GPR registers this spherical wave at different horizontal positions. These waves are received at each surface point  $(x, z = 0)$  as a function of  $t$ , so we can represent them as  $p_i(x, z = 0, t)$ , which satisfying the scalar wave equation

$$\frac{1}{v^2} \frac{\partial^2 p_i}{\partial t^2} = \frac{\partial^2 p_i}{\partial x^2} + \frac{\partial^2 p_i}{\partial z^2} \quad (6.1) \quad \text{eq:wave e}$$

where  $v$  is the velocity of wave propagation and considered constant in the horizontal and vertical direction, Fig. 2.2(b). And the extrapolation equation is

$$k_z(\omega, v) = \left[ \frac{\omega^2}{v^2} - k_x^2 \right]^{\frac{1}{2}}. \quad (6.2) \quad \boxed{\text{eq:extrap}}$$

The vertical wavenumber  $k_z$  represents the dispersion relations of the one-direction wave equation <sup>Gazdag:1984</sup> [15]. For convenience, we list steps of discrete F-K migration here. For an image of size  $M \times N$ , F-K migration is carried out as follows

1.  $\mathbf{P}_i(k_x, \omega) = \text{FFT}\{\mathbf{p}_i(x, t)\}.$
2. Convert the integral over  $\omega$  to an integral over  $k_z(\omega, v)$  by letting

$$k_z(\omega, v) = \left[ \frac{\omega^2}{v^2} - k_x^2 \right]^{\frac{1}{2}}.$$

3.  $\mathbf{P}_o(k_x, k_z) = \mathbf{P}_i(k_x, k_z(\omega, v)).$
4.  $\mathbf{p}_o(x, z) = \text{IFFT}\{\mathbf{P}_o(k_x, k_z)\}.$

In the above procedure, a constant velocity is used in both the vertical and horizontal directions.

### 6.1.2 Regularization

**:regularization**

The mismatches mentioned in Chapter 2 deteriorates performance of F-K migration. Despite the above mismatches, F-K migration has been shown to work very well in GPR application <sup>Yu:1996,Holzrichter:2000</sup> [33, 34]. On the other

hand, because of these factors F-K migration may lose its resolution and sidelobes may show up in F-K



surface is the line denoted by  $ABDE$ , Fig. 6.1(b). The first GPR is still at  $C_1$  and but the second GPR is at  $C_3$ . Estimating time-delays as in the first case, we then draw two circles of different radii because it takes longer for the GPR at  $C_3$  to receive reflection from  $G$ . Circle  $\odot C_1$  and  $\odot C_3$  intersects at the correct object position  $G$ . But that is under the assumption that we know how the ground surface changes. In reality, without knowing the shape of ground surface, it will be assumed that the second GPR is still at position  $C_2$ . Moving the center of  $\odot C_3$  to  $C_2$ , the new circle  $\odot C_2$  intersects with  $\odot C_1$  at  $F$ , which is deeper than the correct object position. Therefore it confirms that when ground surface is rough, applying F-K migration or other migration methods by assuming a flat ground surface will introduce error in the output. One way to correct the above error is to assign a small radius to  $\odot C_2$ , which means a small velocity shall be used to back-propagate waves received by the GPR at  $C_2$ . Essentially a desirable method can use varying velocities to correct for the error introduced by the rough ground surface. The horizontal velocity dependence makes Eq. 6.1 and hence Eq. 6.2 no longer applicable because now  $v$  is function of  $x$ . Nonetheless, from the perspective of imaging processing, it is feasible to fine-tune Eq. 6.2 such that  $k_z = k_z(\omega, k_x, v(x))$ . As shown in section 6.2, improved results are obtained by allowing horizontal velocity dependence.

Our approach is better described in discrete form. Specifically, we denote the initial estimate of velocity by  $v_0$  and using vector notation, we write  $v_0$  as a vector of length  $N$ ,  $\mathbf{v}_0 = [v_0, \dots, v_0]$ , Fig. 6.2(a). For a measured wavefield  $\mathbf{p}$  of size  $M \times N$ , from Eq. 6.2 we have a matrix  $\mathbf{k}_z$  of the same size such that

$$\mathbf{k}_z(m, n) = \left[ \frac{\omega^2(m)}{v_0^2(n)} - k_x^2(n) \right]^{\frac{1}{2}}, \quad m = 1, \dots, M, \quad n = 1, \dots, N. \quad (6.3)$$

Here we call  $\mathbf{k}_z$  the extrapolation matrix. In order to obtain better result, we allow velocities be different at

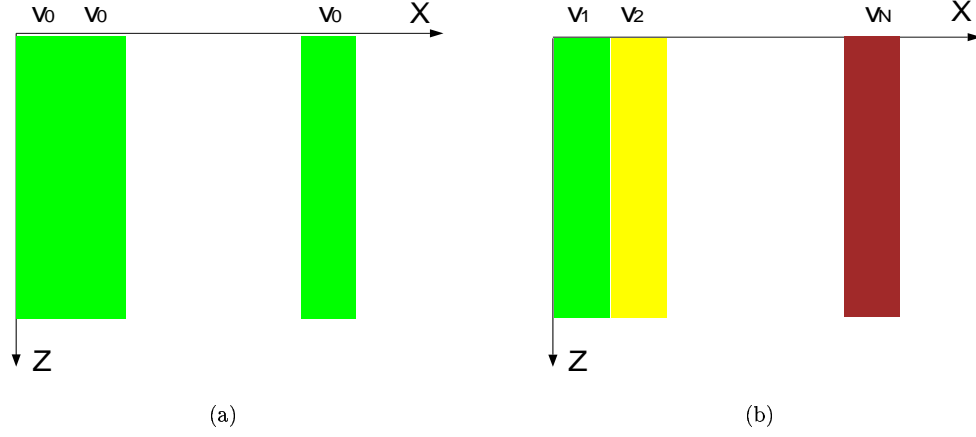


fig:velocity

Figure 6.2: a) constant velocity in the horizontal direction, b) varying velocity in the horizontal direction.

each GPR position, Fig. 6.2(b). Denoting the new velocity vector as  $\mathbf{v}$ , the extrapolation matrix becomes

$$\mathbf{k}_z(m, n) = \left[ \frac{\omega^2(m)}{v^2(n)} - k_x^2(n) \right]^{\frac{1}{2}}, \quad m = 1, \dots, M, \quad n = 1, \dots, N. \quad (6.4)$$

In optimization, we then look for a solution to the following constrained optimization problem

$$\hat{\mathbf{v}} = \arg \min_{\mathbf{v}} \|\mathbf{v} - \mathbf{v}_0\|_2^2 + \lambda^2 \mathbf{R}(\mathbf{p}_0). \quad (6.5)$$

eq:object

Equation (6.5) is known as Tikhonov regularization <sup>Beige:2000</sup> [47] in signal processing. The regularization operator

$\mathbf{R}$  is chosen to be the inverse of varimax of  $\mathbf{p}_0$

$$\mathbf{R}(\mathbf{p}_0) \equiv \left[ \frac{\sum_{m=1}^M \sum_{n=1}^N \mathbf{p}_0^4(m, n)}{[\sum_{m=1}^M \sum_{n=1}^N \mathbf{p}_0^2(m, n)]^2} \right]^{-1}. \quad (6.6)$$

The  $\mathbf{R}(\mathbf{p}_0)$  is considered an approximation to entropy <sup>Wu:1998</sup> [48]. The advantages of using inverse of varimax



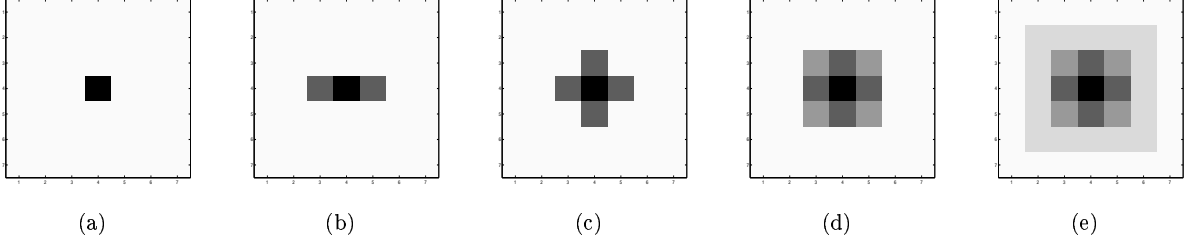


Figure 6.3: Image  $\mathbf{p}$ , a) an image of all zeros with one non-zero element,  $\mathbf{R}(\mathbf{p}) = 1$ , b)–e), images of more non-zero elements,  $\mathbf{R}(\mathbf{p}) = 2.0, 3.33, 5.0, 5.88$ , respectively.

fig:varimax norm

norm over entropy are in computation, 1) computing varimax norm avoids logarithm of zero, which may happen in computing entropy, 2) for an image of size  $M \times N$ , the computational load of varimax norm is a linear function of  $MN$  and the computational load of the entropy with  $L$  discrete probability levels is a linear function of  $MNL$ , much more expensive if  $L$  is large. The first term in the objective function (6.5) is a velocity fidelity constraint. It keeps distance between  $\mathbf{v}$  and  $\mathbf{v}_0$  small because  $\mathbf{v}_0$  is often a good starting point. The second term plays the role of a regularizer and is used to minimize entropy of  $\mathbf{p}_0$ . As  $\lambda \rightarrow 0$ , we demand that  $\mathbf{v}$  stay close to  $\mathbf{v}_0$ . On the other hand, as  $\lambda \rightarrow \infty$ ,  $\mathbf{v}_0$  plays a limited role in influencing  $\mathbf{v}$  and  $\mathbf{v}$  is solely determined by minimizing  $\lambda^2 \mathbf{R}(\mathbf{p}_0)$ .

Minimizing  $\mathbf{R}(\mathbf{p}_0)$  is to obtain simplicity or certainty in  $\mathbf{p}_0$ . Fig. 6.3 describes the behavior of  $\mathbf{R}$ . An image of all zeros and one non-zero element has the highest degree of certainty and it has a small  $\mathbf{R}(\mathbf{p})$  value of 1, Fig. 6.3(a). Adding more non-zero elements to the image reduces its certainty and the image appears blurred. Fig. 6.3(b)–(e) shows that for images with increasing number of nonzeros, the corresponding  $\mathbf{R}(\mathbf{p})$  increases monotonically. In the case of F-K migration, minimizing  $\mathbf{R}(\mathbf{p}_0)$  effectively eliminates some sidelobes in the resulting images and sharpens mainlobes, which correspond to the correct positions of buried landmines, as shown in section 6.2.

Two dimensional F-K migration can be easily expanded to 3-D situation. In 3-D, wavefield  $p_i(x, y, z, t)$  obeys the 3-D scalar wave equation

$$\frac{1}{v^2} \frac{\partial^2 p_i}{\partial t^2} = \frac{\partial^2 p_i}{\partial x^2} + \frac{\partial^2 p_i}{\partial y^2} + \frac{\partial^2 p_i}{\partial z^2}. \quad (6.7)$$

And (6.2) becomes

$$k_z(\omega, v) = \left[ \frac{\omega^2}{v^2} - k_x^2 - k_y^2 \right]^{\frac{1}{2}} \quad (6.8)$$

The corresponding optimized 3-D F-K migration is a direct generalization of the optimized 2-D F-K migration. The 3-D F-K migration can be implemented using one-pass method or two-pass method which consists of implementing two 2-D F-K migration successively, one in the  $x$ -direction and the other in the orthogonal direction, i.e, the  $y$ -direction <sup>Gibson:1983, Jakubowicz:1983</sup> [30, 31]. The one-pass method is also called *full* 3-D migration <sup>Gibson:1983</sup> [31], meaning that migration is accomplished in a single pass at the full volume of 3-D data. In this paper, we chose to use the one-pass method. In the optimization part of the 3-D F-K migration, the varimax norm is taken over the full 3-D F-K migration images. Let  $\mathbf{p}_0$  be a 3-D matrix of size  $M \times N \times L$ , then

$$\mathbf{R}(\mathbf{p}_0) \equiv \left[ \frac{\sum_{m=1}^M \sum_{n=1}^N \sum_{l=1}^L \mathbf{p}_0^A(m, n, l)}{[\sum_{m=1}^M \sum_{n=1}^N \sum_{l=1}^L \mathbf{p}_0^2(m, n, l)]^2} \right]^{-1}. \quad (6.9)$$

## 6.2 Examples

In this section, we apply regular F-K migration and the optimized F-K migration to some data obtained at DeTeC <sup>DeTeC:1997</sup> [49]. At first, we demonstrate the effectiveness of our method in enhancing 2-D F-K migration image. In the next subsection, we compare results of regular F-K migration and the optimized method in 3-D cases.

### 6.2.1 2-D examples

Fig. 6.4 shows the GPR signals over a small anti-personnel mine T72 of low metallic contents. In Fig. 6.4(a) the hyperbolic curve of the mine is clear but there is interference beneath the hyperbolic curve. In regular F-K migration, the mine position is correctly marked but sidelobes beneath the mine are severe. Our method produces a better image in which the mainlobe is enhanced, and sidelobes are considerably suppressed. Fig. 6.5 compares result of regular F-K migration and our method over a large anti-personnel mine, PMN. This mine has a “large” metallic content and a strong GPR reflection. Our method has a higher resolution than the regular F-K migration does. Fig. 6.6 and Fig. 6.7 compare regular F-K migration and the optimized method over two LI11 landmines. In Fig. 6.6, our method focuses at the right position of the landmine while regular F-K migration generates a very noisy picture and puts mine location at a wrong place. For the second LI11 landmine, the optimized method has a more obvious mainlobe and magnitude of sidelobes are reduced. Table 6.1 lists values of  $\mathbf{R}(\mathbf{p}_0)$  of the regular and the optimized F-K migration of the above examples. As expected, results of the optimized F-K migration have smaller values of  $\mathbf{R}(\mathbf{p}_0)$  (smaller entropy) than the regular method. Note that among the examples, results of small  $\mathbf{R}(\mathbf{p}_0)$  are visually more appealing than

those of large values.

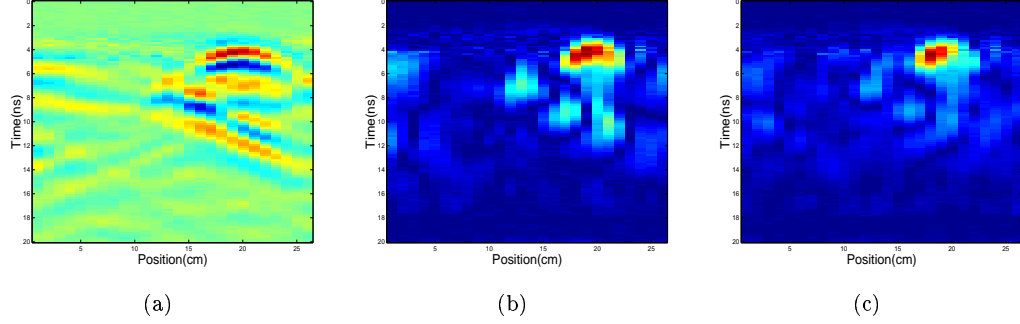


Figure 6.4: F-K migration, a) GPR signals over a T72 mine, b) result of F-K migration, c) result of optimized F-K migration.

K migration T72

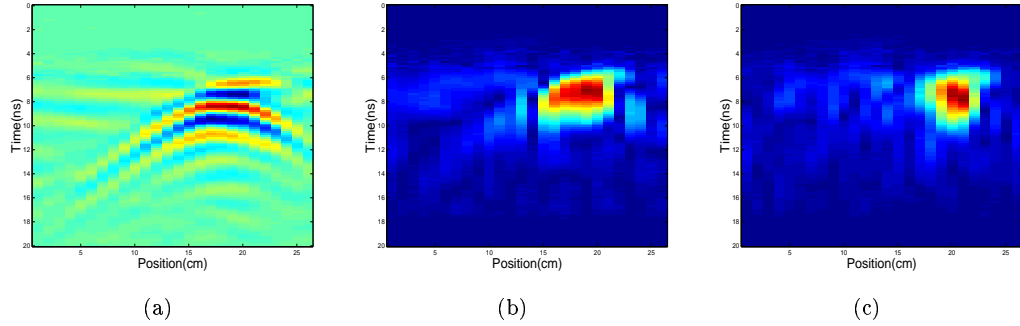


Figure 6.5: F-K migration, a) GPR signals over a PMN mine, b) result of F-K migration, c) result of optimized F-K migration.

K migration PMN

### 6.2.2 3-D examples

Here we use GPR signals obtained from a 2-D grid on the  $x - y$  plane to show that our method has superior performance than the regular F-K migration in three dimensions. The left column of Fig. 6.8 shows the GPR signals from a  $26 \times 4$  grid over a PMN landmine. Grid unit is 2cm. Using the  $26 \times 4$  traces as input, regular 3-D F-K migration results are shown in the middle column. Results from our method are shown in the right

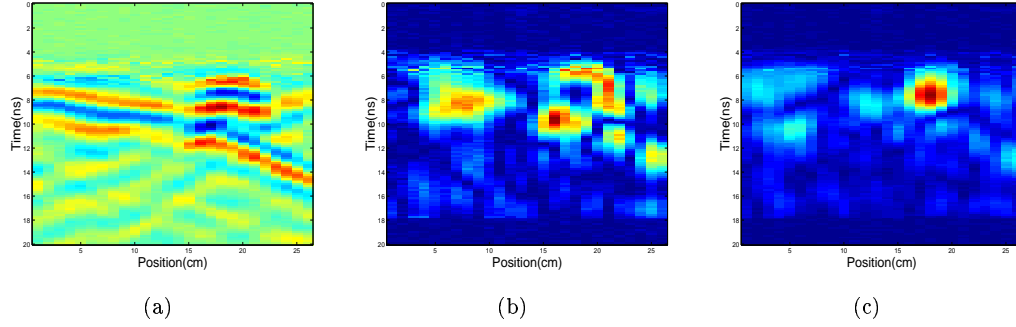


Figure 6.6: F-K migration, a) GPR signals over an LI11 mine, b) result of F-K migration, c) result of optimized F-K migration.

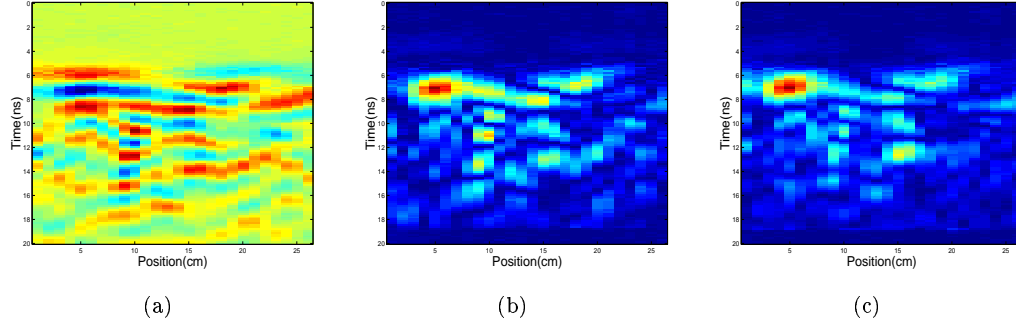


Figure 6.7: F-K migration, a) GPR signals over another LI11 mine, b) result of F-K migration, c) result of optimized F-K migration.

column, which compares favorably to the regular F-K migration. While there are variations in regular F-K migration results, results of the optimized F-K migration are very consistent and correctly mark the mine position.

### 6.3 Concluding Remarks

F-K migration can be used to process GPR array data to localize buried landmines. We point out some limitations of using F-K migration on GPR array data and propose an optimization method in the form of

Table 6.1:  $\mathbf{R}(\mathbf{p}_o)$  of F-K migration and optimized F-K migration results.

| $\mathbf{R}(\mathbf{p}_o)$ | T72 | PMN | LI11 (1) | LI11 (2) |
|----------------------------|-----|-----|----------|----------|
| F-K migration              | 233 | 333 | 588      | 556      |
| Optimized F-K migration    | 204 | 256 | 357      | 476      |

varimax norm

Tikhonov regularization to improve performance of F-K migration. As it is well known, performance of F-K migration is directed determined by the wave propagation velocity. In regular F-K migration, velocity is considered constant in the horizontal direction. The optimized F-K migration, aiming at minimizing entropy of F-K migration image, allows wave propagation velocities be different at different GPR positions. The effect of varying velocities is to offset interferences introduced by rough ground surface, clutter, and possible soil inhomogeneity. Minimizing entropy allows the optimized F-K migration to generate sharp and clean image. A well chosen regularization parameter suppresses sidelobes in the F-K migration image and keeps mainlobe at the correct position. Further modification and fast implementation of the optimization method are discussed in Chapter 7.

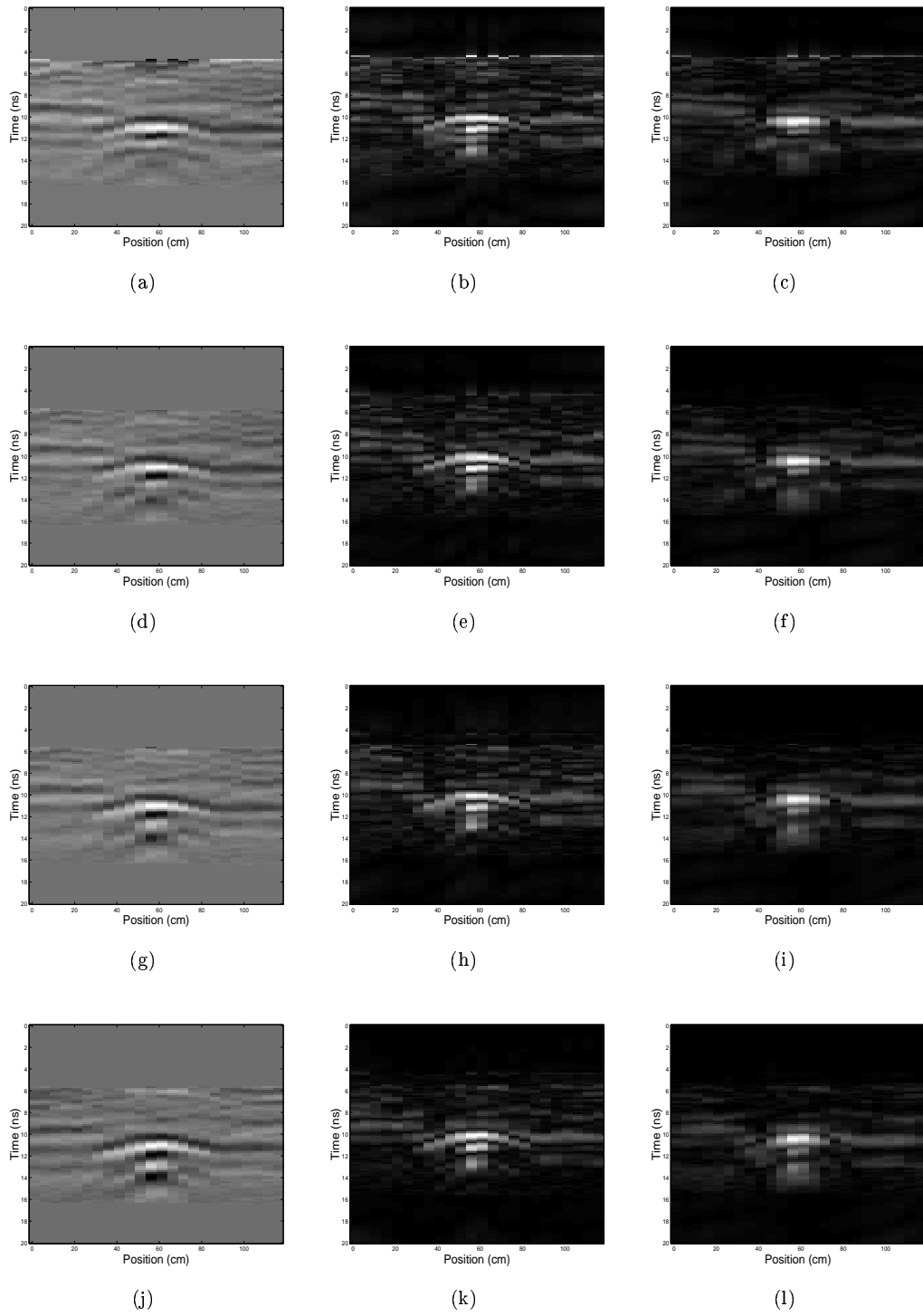


Figure 6.8: 3-D example, left column, regular F-K migration image; right column, optimized F-K migration image.

# Chapter 7

## Future Work

ch:future work

In previous chapters, we have demonstrated the performance of HANOVA followed by SPRT in object detection and optimized F-K migration in object localization. Proposed work will be on a few fronts as explained next.

### 7.1 Sequential Detection and Localization: Analytical Performance

#### Evaluation

and Localization

Here we will work on schemes to integrate the sequential detection with localization. As the GPR moves down-track, F-K migration can take wavefield obtained as input and back-propagate the wavefield. As new trace obtained, F-K migration can combine the new trace with previous data in a “roll-over” manner. Therefore, F-K migration can be incorporated with SPRT to detect and localize at the same time. Optimization can be computed by a second computer or in a parallel computing scheme. On the other hand, we will use



Monte-Carlo method to evaluate the performance of SPRT in terms of average run length and ROC's.

## 7.2 Physics and Optimization

and optimization

From the viewpoint of pure image processing, introducing horizontal velocity dependence is a method to obtain better result. From the perspective of geophysics, the effect and meaning of horizontal velocity dependence is not very clear at this point. In this part of the future work, we will examine the implication of the horizontal velocity dependence on F-K migration. For the convenience of discussion, we summarize regular F-K migration here

$$P_i(k_x, \omega) = \int \int p_i(x, z=0, t) e^{-i(k_x x + \omega t)} dx dt \quad (7.1) \quad \text{eq:ch7 1}$$

$$k_z(\omega) = \left[ \frac{\omega^2}{v^2} - k_x^2 \right]^{\frac{1}{2}} \quad (7.2) \quad \text{eq:ch7 2}$$

$$p_o(x, z, t=0) = \int \int P(k_x, \omega) e^{i[k_z(\omega)z + k_x x]} d\omega dk_x. \quad (7.3) \quad \text{eq:ch7 3}$$

Substituting (7.2) into (7.3), we obtain

$$p_o(x, z, t=0) = \int \int P_i(k_x, \omega) e^{i\left[\left(\frac{\omega^2}{v^2} - k_x^2\right)^{1/2} z + k_x x\right]} d\omega dk_x. \quad (7.4) \quad \text{eq:ch7 F-}$$

In F-K migration, we treat the exploding reflector as a source and back-propagates from receivers to the exploding reflector. On the other hand, we can also treat the receivers as an “array of sources” at positions  $(x_m, 0)$  where  $m = 1, \dots, M$  and the exploding reflector as a “receiver” at position  $(x, z)$ . In this way, waves propagate forward from the “array of transmitters” to the “receiver”. This process can be thought of as

a radiation problem and easily described by using Green's function [Leuschen:2001, 50]. Using vector notation shown in

Fig. 7.1, we have

$$p_o(\mathbf{r}') = \sum_{x=x_1}^{x_M} \int P^*(x, \omega) [-\omega^2 \mu_0 G(\mathbf{r}', \mathbf{r}_x; \omega)] d\omega \quad (7.5) \quad \text{eq:Green'}$$

where  $G(\mathbf{r}', \mathbf{r}_x)$  is the propagation Green's function of the zero-offset GPR collections,  $P(x, \omega)$  is the received signal by the  $x$ th receiver in frequency domain,  $\omega$  is the temporal frequency, and the superscript  $*$  stands for complex conjugate. It is known that the Green's function is a function only of the difference vector  $\mathbf{R} = \mathbf{r}' - \mathbf{r}_x$  and it satisfies the equation

$$[\nabla^2 + k^2]G(\mathbf{r}' - \mathbf{r}_x) = -4\pi\delta(\mathbf{r}' - \mathbf{r}_x) \quad (7.6)$$

where  $\delta(\cdot)$  is the Dirac delta function and  $\mathbf{r}' - \mathbf{r}_x = (x - x_m)\hat{\mathbf{x}} + z\hat{\mathbf{z}}$ . The Green's function solution to the migration problem represents this solution in terms of a superposition of outgoing spherical waves with each spherical wave being centered at the “source point”  $\mathbf{r}_x$  and weighted by the source strength  $P(x, \omega)$  at that point. For comparison, we Fourier transform  $P(x, \omega)$  with respect to  $x$  and rewrite (7.5) as

$$\begin{aligned} p_o(\mathbf{r}') &= \sum_{x=x_1}^{x_M} \int \left[ \int P^*(k_x, \omega) e^{-ik_x x} dk_x \right] [-\omega^2 \mu_0 G(\mathbf{r}' - \mathbf{r}_x; \omega)] d\omega \\ &= \sum_{x=x_1}^{x_M} \int \int P^*(k_x, \omega) e^{-ik_x x} [-\omega^2 \mu_0 G(\mathbf{r}' - \mathbf{r}_x; \omega)] d\omega dk_x \\ &= \int \int P^*(k_x, \omega) \sum_{x=x_1}^{x_M} e^{-ik_x x} [-\omega^2 \mu_0 G(\mathbf{r}' - \mathbf{r}_x; \omega)] d\omega dk_x \end{aligned} \quad (7.7) \quad \text{eq:Green'}$$

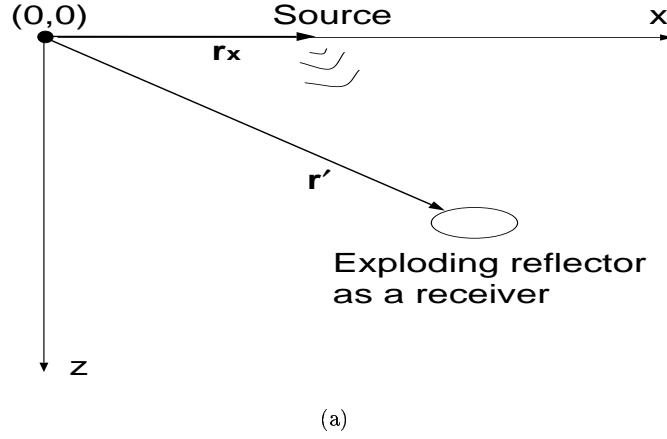


Figure 7.1: GPR geometry.

Green's function

Comparing (7.4) and (7.7), we can see that the two migration equations are essentially the same. They both apply a filter to the received signals to back-propagate them to the exploding reflector. The Green's function solution is based on the fact that the Helmholtz equation is linear and can be represented as a superposition of elementary solutions to the equation when excited by delta functions. The F-K migration based on the wave-equation reverses the roles of sources and receiver in Fig. 7.1 and back-propagates waves to the receiver. Because of the reciprocity of the Green's function, it is not hard to see that the two expressions are identical in physics.

### 7.3 F-K migration in inhomogeneous medium

us FK migration

While F-K migration and other migration methods inversely propagate wavefield from the surface to sub-surface, they do not explicitly take into account of attenuation in the soil. In this part of future work, we propose a modification of F-K migration such that attenuation is considered. The 2D scalar wave equation

in inhomogeneous medium is <sup>[Chew:1990](#)</sup>  
<sup>[\[51\]](#)</sup>

$$\frac{\partial^2 p_i}{\partial x^2} + \frac{\partial^2 p_i}{\partial z^2} = \frac{1}{v^2} \frac{\partial^2 p_i}{\partial t^2} + \tau \frac{\partial p_i}{\partial t} \quad (7.8) \quad \text{eq:inhomo}$$

where

$$\tau = \frac{\mu}{\sigma} \quad (\text{H}\cdot\text{U}/\text{m}^2) \quad (7.9)$$

where  $\mu$  and  $\sigma$  are magnetic permeability and electric conductivity, respectively. Small  $\tau$  means low attenuation. When  $\tau$  is infinitely small, the lossy wave equation reduces to the loss-free wave equation. Take Fourier transform of (7.8), we obtain

$$(-jk_x)^2 P_i + P_i'' = \frac{1}{v^2} (-j\omega)^2 P_i + (-j\omega)\tau P_i. \quad (7.10) \quad \text{eq:inhomo}$$

From (7.10), we derive the extrapolation equation as

$$k_z = \left[ \frac{\omega^2}{v^2} + j\omega\tau - k_x^2 \right]^{\frac{1}{2}}. \quad (7.11) \quad \text{eq:inhomo}$$

By taking attenuation into the wave equation, better results are expected from the F-K migration.

## 7.4 Quantification of Resolution

Following the work of Berkhout<sup>Berkhout:1979</sup> [52] in defining resolution of far-field migrated result, we propose to use similar approach to examine the resolution of near-field migration. The spatial resolution of the image is determined by the width of the mainlobe, and the dynamic range is determined by the ratio of the mainlobe amplitude over the maximum sidelobe amplitude. Narrower mainlobes and higher dynamic ranges provide better resolved images. The lateral resolution of migration depends on the size of the GPR array and the near field nature of GPR application in our research.

# Bibliography

Peters:1994

- [1] L. Peters Jr., J. J. Daniels, and J. D. Young, “Ground penetrating radar as a subsurface environmental sensing tool”, *Proc. IEEE*, vol. 82, no. 12, pp. 1802–1822, Dec. 1994.

Witten:1994

- [2] A. J. Witten, J. E. Molyneux, and J. E. Nyquist, “Ground penetrating radar tomography: algorithms and case studies”, *IEEE Trans. Geosci. Remote Sensing*, vol. 32, no. 2, pp. 461–467, Mar. 1994.

Uppsall:2000

- [3] M. S. Uppsall, L. M. Pettersson, M. Georgson, and S. Sjokvist, “Temporal IR contrast variation of buried landmines”, in *Proc. SPIE AeroSense Detection and Remediation Technologies for Mines and Minelike Targets V*, Orlando, FL, Apr. 2000, vol. 4038, pp. 146–155.

Sendur:2000

- [4] I. K. Sendur and B. A. Baertlein, “Numerical simulation of thermal signatures of buried mines over a diurnal cycle”, in *Proc. SPIE AeroSense Detection and Remediation Technologies for Mines and Minelike Targets V*, Orlando, FL, Apr. 2000, vol. 4038, pp. 156–167.

Drewniak:2000

- [5] J. L. Drewniak and W. Cui, “Detection of electronic mines, timers, and fuses through electromagnetic interference signatures and stimulated emissions”, in *Proc. SPIE AeroSense Detection and Remediation Technologies for Mines and Minelike Targets V*, Orlando, FL, Apr. 2000, vol. 4038, pp. 66–77.

- Ozdemir:2000** [6] M. Ozdemir, E. L. Miller, and A. J. Witten, “Clutter modeling and estimation methods for low metal content mine characterization from broadband electromagnetic induction data”, in *Proc. SPIE AeroSense Detection and Remediation Technologies for Mines and Minelike Targets V*, Orlando, FL, Apr. 2000, vol. 4038, pp. 45–55.
- McKnight:2000** [7] S. W. McKnight, C. A. DiMarzio, and W. Li, “Laser-induced acoustic generation for buried object detection”, in *Proc. SPIE AeroSense Detection and Remediation Technologies for Mines and Minelike Targets V*, Orlando, FL, Apr. 2000, vol. 4038, pp. 734–739.
- DiMarzio:2000** [8] C. A. DiMarzio, W. Li, L. J. Berg, and J.M Sabatier, “Toward a laser-based, non-contact acoustic landmine imager”, in *Proc. SPIE AeroSense Detection and Remediation Technologies for Mines and Minelike Targets V*, Orlando, FL, Apr. 2000, vol. 4038, pp. 740–747.
- Hibbs:2000** [9] A. D. Hibbs et al, “Field tests results of a nuclear quadrupole resonance landmine detection system”, in *Proc. SPIE AeroSense Detection and Remediation Technologies for Mines and Minelike Targets V*, Orlando, FL, Apr. 2000, vol. 4038, pp. 564–571.
- Chan:1979** [10] L. C. Chan, D. L. Moffatt, and L. Peters, Jr., “A Characterization of sub-surface radar targets”, *Proc. IEEE*, vol. 67, no. 7, pp. 991–1001, July 1979.
- Daniels:1988** [11] J. J. Daniels, “Locating caves, tunnels, and mines: the leading edge of exploration”, *Soc. Expl. Geophys.*, Jan-Feb 1988.
- Daniels:1989** [12] J. J. Daniels, “Fundamentals of ground penetrating radar”, in *Proc. Symp. on the Application of Geophysics to Engineering and Environmental Problems*, Golden, CO, Mar. 1989.

- [13] J. J. Daniels and R. L. Roberts, “Ground penetrating radar for geotechnical applications”, *Geophysical Characterization of Sites, AMCE*, vol. ISSMFE TC #10 Publication on Geophysics, special volume XIII ICSMFE, 1994.
- [14] C. M. Rappaport, S. G. Azevedo, T. Rosenbury, and J. Gough, “Handheld forward-Looking focused array mine detection with plane wave excitation”, in *Proc. SPIE AeroSense Detection and Remediation Technologies for Mines and Minelike Targets V*, Orlando, FL, Apr. 2000, vol. 4038, pp. 1118–1126.
- [15] J. Gazdag and P. Sguazzero, “Migration of seismic data”, *Proc. IEEE*, vol. 72, no. 10, pp. 1302–1315, 1984.
- [16] E .A. Robinson, *Migration of Geophysical Data*, Int. Human Resources Development Corporation, Boston, MA, 1983.
- [17] E. L. Miller and A. S. Willsky, “Multiscale, statistical anomaly detection analysis and algorithms for linearized inverse scattering problems”, *Multidimensional Systems and Signal Processing*, vol. 8, pp. 151–184, 1995.
- [18] X. Xu, E. L. Miller, G. Sower, and T. Broach, “Detection of buried mines from GPR array measurement: a statistical approach”, in *Int. Geosci. and Remote Sensing Symp. (IGARSS)*, Honolulu, HA, July 2000.
- [19] P. G. Gader, H. Frigui, B. N.Nelson, G. Vaillete, and J. M. Keller, “New results in fuzzy set based detection of landmines with GPR”, in *Proc. SPIE AeroSense Detection and Remediation Technologies for Mines and Minelike Targets IV*, Orlando, FL, Apr. 1999, vol. 3710, pp. 1075–1084.



- [Gader:2000] [20] P. D. Gader, Y. Zhao, M. Mystkowski, M. A. Khabou, and Y. Zhang, “Hidden Markov models and morphological neural networks for GPR-based landmine detection”, in *Proc. SPIE AeroSense Detection and Remediation Technologies for Mines and Minelike Targets V*, Orlando, FL, Apr. 2000, vol. 4038, pp. 1096–1107.
- [Bradley:1999] [21] M. Bradley, “Mine detection with a multichannel stepped-frequency ground-penetrating radar”, in *Proc. SPIE AeroSense Detection and Remediation Technologies for Mines and Minelike Targets IV*, Orlando, FL, Apr. 1999, vol. 3710, pp. 953–960.
- [Dogaru:1998] [22] T. Dogaru and L. Carin, “Time-domain sensing of targets buried under a rough air-ground interface”, *IEEE Trans. Antennas Propagat.*, vol. 46, no. 3, pp. 360–372, Mar. 1998.
- [Xu:1999] [23] X. Xu, E. L. Miller, and C. M. Rappaport, “Statistically-based sequential detection of buried mines from array ground penetrating radar data”, in *Proc. SPIE AeroSense Detection and Remediation Technologies for Mines and Minelike Targets IV*, Orlando, FL, Apr. 1999, vol. 3710, pp. 1063–1075.
- [Xu:2000] [24] X. Xu and E. L. Miller, “A statistical approach to object detection from ground penetrating radar arrays”, in *Progress in Electromagnetics Research Symposium*, Boston, MA, July 2000.
- [Helstrom:1995] [25] C. W. Helstrom, *Elements of Signal Detection and Estimation*, Prentice-Hall, New York, NY, 1995.
- [Ghosh:1970] [26] B. K. Ghosh, *Sequential Tests of Statistical Hypotheses*, Addison-Wesley, Reading, MA, 1970.
- [Fan:1996] [27] J. Fan, “Test of significance based on wavelet thresholding and Neyman’s truncation”, *J. of American Statistical Association*, vol. 91, pp. 674–688, 1996.
- [Port:1994] [28] S. C. Port, *Theoretical Probability for Applications*, John Wiley & Sons, New York, NY, 1994.

- [Fan:1998] [29] J. Fan and S. Lin, “Test of significance when data are curves”, *J. of American Statistical Association*, vol. 93, pp. 1007–1021, 1998.
- [Jakubowicz:1983] [30] H. Jakubowicz and S. Levin, “A simple exact method of 3-D migration–theory”, *Geophys. Prospect.*, vol. 31, pp. 34–56, 1983.
- [Gibson:1983] [31] B. Gibson, K. Larner, and S. Levin, “Efficient 3-D migration in two steps”, *Geophys. Prospect.*, vol. 31, pp. 1–33, 1983.
- [Gazdag:1978] [32] J. Gazdag, “Wave equation migration with the phase-shift method”, *Geophys.*, vol. 43, no. 7, pp. 1342–1351, Dec. 1978.
- [Yu:1996] [33] H. Yu, X. Ying, and Y. Shi, “The use of FK techniques in GPR processing”, in *6’TH Int. Conf. on Ground Penetrating Radar(GPR’96)*, Sendai, Japan, Sept. 1996, pp. 595–600.
- [Holzrichter:2000] [34] M. W. Holzrichter and G. E. Sleefe, “Resolution enhancement of landmines in ground penetrating radar images”, in *Proc. SPIE AeroSense Detection and Remediation Technologies for Mines and Minelike Targets V*, Orlando, FL, Apr. 2000, vol. 4038, pp. 1160–1170.
- [Belge:1998] [35] M. Belge, E. L. Miller, and M. Kilmer, “Simultaneous multiple regularization parameter selection by means of the L-hypersurface with applications to linear inverse problems posed in the wavelet transform domain”, in *SPIE Int. Symp. on Optical Sci., Engineering, and Instrumentation: Bayesian Inference for Inverse Problems*, July 1998, vol. 3459, pp. 328–336.
- [Hansen:1992] [36] P. C. Hansen, “Analysis of discrete ill-posed problems by means of the L-curve”, *SIAM Review*, vol. 34, no. 4, pp. 561–580, Dec. 1992.

- [Bourgeois:1996] [37] J. M. Bourgeois and G. S. Smith, “A fully three-dimensional simulation of a ground-penetrating radar: FDTD theory compared with experiment”, *IEEE Trans. Geosci. Remote Sensing*, vol. 34, no. 1, pp. 36–44, Jan. 1996.
- [Rappaport:1996] [38] C. M. Rappaport and D. M. Reidy, “Focused array radar for real time imaging and detection”, in *Proc. SPIE, Radar Sensor Technology*, Orlando, FL, Apr. 1996, vol. 2747, pp. 202–213.
- [Balanis:1989] [39] C. Balanis, *Advanced Engineering Electromagnetics*, John Wiley & Sons, Inc., New York, NY, 1989.
- [EGG] [40] “UXO Signature Data”, <http://www.denix.osd.mil/denix/Public/News/UXO-COE/Sigdata/sigdata.html>, 1999.
- [Shi:1999] [41] P. Shi and E. L. Miller, “Baseband Wiener filter processing for mine detection from scanned laser induced acoustic data”, in *Proc. SPIE AeroSense Detection and Remediation Technologies for Mines and Minelike Targets IV*, Orlando, FL, Apr. 1999, vol. 3710.
- [El-Shenawee:2000] [42] M. El-Shenawee and C. M. Rappaport, “Quantifying the effects of different rough surface statistics for mine detection using the FDTD technique”, in *Proc. SPIE AeroSense Detection and Remediation Technologies for Mines and Minelike Targets V*, Orlando, FL, Apr. 2000, vol. 4038, pp. 966–975.
- [Siegmund:1985] [43] D. Siegmund, *Sequential Analysis: Tests and Confidence Intervals*, Springer-Verlag, New York, NY, 1985.
- [Basseville:1993] [44] M. Basseville and I. V. Nikiforov, *Detection of Abrupt Changes: Theory and Application*, Prentice-Hall, New York, NY, 1993.
- [Jain:1989] [45] A. K. Jain, *Fundamentals of Digital Image Processing*, Prentice-Hall, Englewood Cliffs, NJ, 1989.

- [Xu:2000c] [46] X. Xu and E. L. Miller, “A statistical approach to multichannel blind signal detection for ground penetrating radar arrays”, in *IEEE Sensor Array and Multichannel (SAM) Signal Processing Workshop*, Cambridge, MA, Mar. 2000.
- [Belge:2000] [47] M. Belge, M. Kilmer, and E. L. Miller, “Wavelet domain image restoration with adaptive edge-preserving regularization”, *IEEE Trans. Image Processing*, vol. 9, no. 4, pp. 598–608, Apr. 2000.
- [Wu:1998] [48] H. Wu and J. Barba, “Minimum entropy restoration of star field images”, *IEEE Trans. Systems, Man, and Cybernetics*, vol. 28, no. 2, pp. 227–231, Apr. 1998.
- [DeTeC:1997] [49] “DeTeC GPR data”, <http://diwww.epfl.ch/lami/detec/gprimages.html>, 1997.
- [Leuschen:2001] [50] C. L. Leuschen and R. G. Plumb, “A matched-filter-based reverse-time migration algorithm for ground-penetrating radar data”, *IEEE Geoscience*, vol. 39, no. 5, pp. 929–936, May 2001.
- [Chew:1990] [51] W. C. Chew, *Waves and Fields in Inhomogeneous Media*, Van Nostrand Reinhold, New York, NY, 1990.
- [Berkhout:1979] [52] A. J. Berkhout and D. W. Van Wulfften Palthe, “Migration in terms of spatial deconvolution”, *Geophys. Prospect.*, vol. 27, pp. 261–291, 1979.